POLITECNICO DI TORINO

Collegio di Ingegneria Chimica e dei Materiali

Master of Science Course
in Materials Engineering for Industry 4.0

Master of Science Thesis

Synthesis and Characterization of Bismuth-based Catalyst for Electrochemical Reduction of CO_2

Politecnico di Torino

Supervisors:
Giancarlo Cicero
Paolo P. Pescarmona
PhD supervisors:
Jiahui Zhu, Jennifer Hong

Candidate:
Margherita Aragona

July 2025

Abstract

Over the past two centuries, global annual CO_2 emissions have increased by approximately 40 billion tons, becoming the main cause of climate change. To address this pressing issue, many strategies have been developed to reduce atmospheric CO_2 concentration, collectively known as Carbon Capture, Utilization, and Storage (CCUS).[1] Among these, the electrochemical reduction of CO_2 (ECO2RR) stands out as a promising approach, converting CO_2 into reusable carbon-based products with oxygen as the only by-product. Furthermore, when powered by renewable energy sources, ECO2RR can also be use for energy storage. However, the development of catalysts with both high activity and selectivity remains a significant challenge.

This thesis investigates the synthesis and characterization of bismuth-based (Bi-based) catalysts for the electrochemical production of formate. The catalysts were characterized by different techniques such as XRD, SEM, TEM, and TGA to study their physicochemical properties and their ECO2RR performance was evaluated through chronoamperometry testing.
The initial phase of the study aimed to replicate the BiSub@AC-400 catalyst, following previously established methods.[2] Despite modifications to the synthesis parameters, the original material could not be reproduced, with a main difference being the bismuth crystalline phase. While the reference catalyst predominantly contained Bismutite, during this work metallic Bi and Bi_2O_3 were obtained. This might be the reason why the resulting BiSub@AC-400 exhibited superior performance, achieving a current density of -8.8 mA/cm^2 at -1.07 V vs. RHE, compared to the reported -6.2 mA/cm^2.
Subsequently, the research focus shifted to optimizing the synthesis process to improve the distribution of bismuth on the activated carbon (AC) and reduce the nanoparticle (NPs) size, a feature critical for enhancing catalytic activity due to the increased surface-to-volume ratio. To achieve this, bismuth subsalicylate (BiSub) was solubilized in two different environments: ethanol with 1.8M salicylic acid (SA) and in a mixture of ethanol and acetic acid (AcOH), producing BiNPs@AC-SA and BiNPs@AC-AcOH catalysts, respectively. At a catalyst loading of 0.298 mg/cm^2 and -1.07 V vs. RHE, the BiSub@AC-400, BiNPs@AC-SA and BiNPs@AC-AcOH achieved -8.7 mA/cm^2, -7.7 mA/cm^2 and -7.8 mA/cm^2, with faradaic efficiencies of 83 $\pm$ 5%, 75 $\pm$ 6% and 82 $\pm$ 3% respectively. The reduced performance of BiNPs@AC-SA and BiNPs@AC-AcOH may result from the presence of amorphous bismuth or diminished wettability of the materials.
For BiNPs@AC-AcOH, the effect of varying the BiSub:AC ratio was also investigated. Reducing bismuth content decreased current density (-4.1 mA/cm^2) and the faradaic efficiency (70 $\pm$ 3%) but improved formate production per bismuth weight, likely due to a reduction in NPs size.

This study highlights the effect of synthesis parameters on material properties and catalytic performance for ECO2RR, offering valuable insights for the design of more efficient catalysts. Further research on BiNPs@AC-SA and BiNPs@AC-AcOH performance over a wider range of applied potentials is encouraged to optimize their catalytic efficiency.

List of abbreviation

Abbreviation	**Meaning**
AcOH	Acetic acid
AC	Activated Carbon
Bi	Bismuth
BiSub	Bismuth subsalicylate
C	Carbon
CE	Counter Electrode
ECO2RR	Electrochemical CO_2 Reduction Reaction
EtOH	Ethanol
GC	Glassy Carbon
HER	Hydrogen Evolution Reaction
NPs	NanoParticles
NTs	NanoTubes
NWs	NanoWires
OER	Oxygen Evolution Reaction
RE	Reference Electrode
SA	Salicylic Acid
SEM	Scanning Electron Microscopy
TEM	Transmission Electron Microscopy
TGA	ThermoGravimetric Analysis
WE	Working Electrode

Contents

1 Introduction

The excessive combustion of fossil fuels and the resulting emission of CO_2 have caused serious energy and environmental problems, including climate change and negative effects on ecosystems and human health.[1] Carbon dioxide, together with other greenhouse gases (GHGs) such as methane (CH_4) and nitrous oxide (N_2O), forms a layer in the Earth's atmosphere that contributes to the greenhouse effect. While plants and ocean's surface absorb solar energy to sustain life, they re-emit part of this energy as infrared (IR) radiation. Ultraviolet (UV) rays from the Sun penetrate through the atmosphere relatively unimpeded, but the IR radiation, re-emitted from the Earth's surface, is partially trapped by the GHGs layer, leading to an increase in global temperature.[3]
Although climate change is driven by natural processes, human activities have significantly accelerated global warming. Under natural conditions, carbon is exchanged between the atmosphere, oceans, terrestrial biosphere, and, more slowly, sediments and sedimentary rocks. Before the anthropogenic rise in CO_2 emissions, this exchange maintained a relatively stable atmospheric concentration over millennia. However, since the Industrial Revolution, CO_2 emissions have increased substantially due to fossil fuel combustion, deforestation, and population growth, disrupting this balance.[4] In Figure 1 are shown the main components of the global carbon cycle.[5]

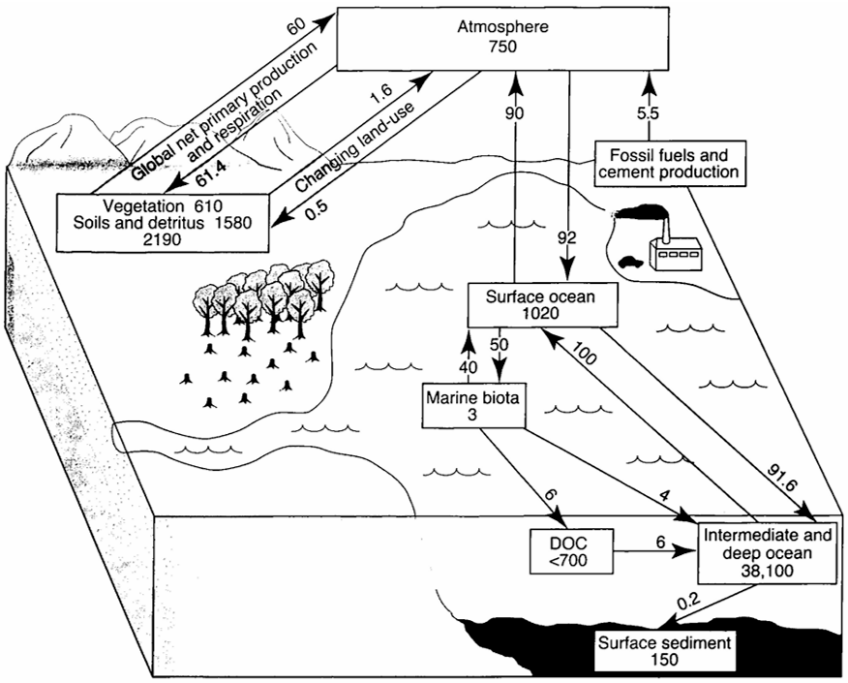

Figure 1: Scheme of the global carbon cycle showing the main components. This figure presents average values.[5]

1.1 Electrochemical reduction of CO_2

To address rising atmospheric CO_2 levels, many strategies, collectively known as Carbon Capture, Utilization, and Storage (CCUS), have been developed. Among them, the electrochemical reduction of CO_2 (ECO_2RR) presents a promising approach to mitigate the rising concentration of carbon dioxide in our atmosphere. This process converts CO_2

into value-added carbon-based products, so it could be combined with carbon-intensive industries for on-site CO_2 valorization to reduce carbon footprints.[6], [7]

1.1.1 Electrochemical cell

In general, during an electrochemical process, a redox reaction occurs thanks to the electron transfer from a species that is oxidized, called the reductant, to one that is reduced, called the oxidant.[8] Since the reactions take place separately at the two surface, the redox process is usually described in terms of two half-reactions. For aqueous solution electrochemistry, each half-reaction is characterized by a standard potential (E^0), defined relative to the Standard Hydrogen Electrode (SHE). By convention, the standard potential of the hydrogen half-cell reaction ($2H^+(aq) + 2e^- \rightarrow H_2(g)$) is assigned a value of 0.0 V.[8]
Considering two generic half-reactions:

$$\begin{aligned} Cathode: \quad & A + ne^- \rightarrow B \\ Anode: \quad & C + me^- \rightarrow D \end{aligned}$$

These can be combined into the overall cell reaction:

$$mA + nD \rightarrow mB + nC$$

Knowing the respective standard potentials, $E^0_{A/B}$ and $E^0_{C/D}$, the standard cell potential can be measure as:[8]

$$E^0_{cell} = E^0_{A/B} - E^0_{C/D}$$

This value provides information about the spontaneity of the reaction: in particular, if $E^0_{cell} > 0$, the redox reaction is spontaneous. From a thermodynamic perspective, the change in Gibbs free energy for the electrochemical cell is related to the cell potential by:[8]

$$\Delta G_{T,P} = -(nm)FE^0_{cell}$$

Where: n and m are the number of electrons transferred per mole of reaction [mol/mol], E^0_{cell} is the cell potential in Volts [V] and F is the Faraday constant [C], the charge of one mole of electrons (96484.6 C). As a result, $\Delta G_{T,P}$ in calculated in [J mol^{-1}]. Since spontaneous reactions are characterized by a decrease in Gibbs free energy ($\Delta G < 0$), this condition corresponds to a positive cell potential ($E^\circ_{\text{cell}} > 0$) in electrochemical systems. When the reaction is spontaneous, the electrochemical cell works as a galvanic cell, converting chemical energy into electrical energy. Conversely, if the reaction is non-spontaneous ($E^0_{cell} < 0$), the cell operates as an electrolytic cell, driving the non-spontaneous reactions through electrical energy given applying an external voltage.

A central reaction in electrochemical systems with aqueous electrolytes is water electrolysis, which produces hydrogen at the cathode and oxygen at the anode. The reduction half-reaction is called Hydrogen Evolution Reaction (HER), while the oxidation one is known as Oxygen Evolution Reaction (OER). In acidic media, these half-cell reactions are as follows:

$$\begin{aligned} 2H^+(aq) + 2e^- \rightarrow H_2(g) \qquad & E^0_{cathode} = 0V \\ 2H_2O(l) \rightarrow O_2(g) + 4H^+(aq) + 4e^- \qquad & E^0_{anode} = 1.23V \end{aligned}$$

The standard cell potential is therefore:

$$E^0_{cell} = E^0_{cathode} - E^0_{anode} = -1.23V$$

Since the cell standard potential is negative, the water splitting reaction is non-spontaneous

under standard conditions, and an external potential must be applied to initiate electrolysis. In practice, the required applied potential exceeds the theoretical value due to overpotentials (η). Overpotentials arise from several kinetic and transport processes involved in an electrode reaction, including:[9]

- Mass transfer of reactants from the bulk electrolyte to the electrode surface.
- Electron transfer at the electrode surface
- Additional chemical reactions preceding or following electron transfer.
- Surface processes such as adsorption, desorption, or crystallization.

The sum of all these contributions determines the overall overpotential of the electrochemical cell.

In this work, the ECO_2RR is carried out in electrochemical systems using aqueous electrolytes at room temperature. Since carbon dioxide is extremely thermodynamic stable, the device operates in the electrolytic configuration. In particular, the ECO_2RR requires high energy to break the strong C=O bonds in carbon dioxide (532 kJ mol^{-1}[10], 750 kJ mol^{-1}[11]). The first electron transfer step in CO_2 reduction transforms the surface-adsorbed CO_2 in the first intermediate. The reaction and its standard potential are given by:[12]

$$CO_2 \rightarrow CO_2^{-\cdot} \qquad E^0 = -1.85 V vs. SHE \tag{1}$$

Furthermore, this step is accompanied by a change in molecular geometry from linear CO_2 to bent $CO_2^{-\cdot}$, resulting in a very slow electron self-exchange rate and consequently a high overpotential.[13] To overcome this kinetic barrier, researchers have developed several catalysts capable of lowering the activation energy and facilitating the multiple proton-coupled electron transfer steps involved in the ECO_2RR.[11] These aspects will be discussed further in subsubsection 1.1.2.

In this work, CO_2 electroreduction is studied using an H-cell configuration, which is a typical laboratory-scale setup. The schematic diagram of the cell and the fundamental processes involved in CO_2 electrolysis are shown in Figure 2.

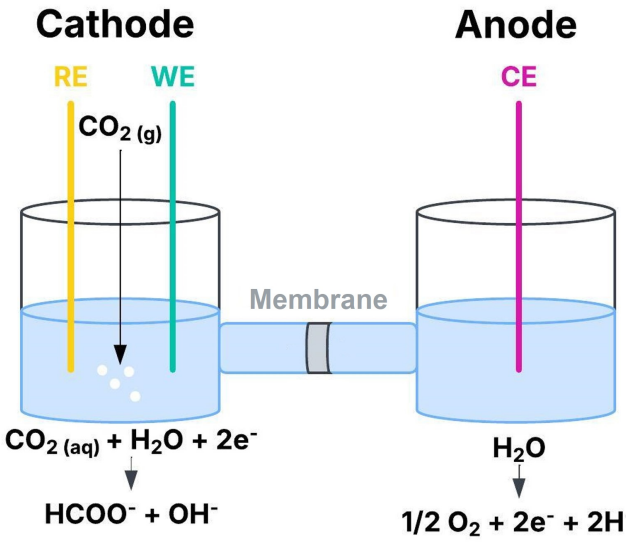

Figure 2: Schematic illustration of the processes taking place in CO_2 electrolysis.

The H-cell consists of two compartments filled by electrolyte solution, referred to as catholyte and anolyte, separated by an ion-exchange membrane to prevent cross-contamination of products. In the anodic compartment, the OER occurs at the counter electrode (CE). The cathodic compartment is equipped with the reference electrode (RE), working electrode (WE) and it is continuously bubbled with CO_2 to saturate the electrolyte. The RE allows accurate control over the applied potential, it functions reliably across a wide potential range and is stable over time.[14] The reduction reactions occur at the WE, which consists of, or is coated with, the electrocatalyst. These reactions are driven by the potential difference applied between the WE and the RE by the potentiostat. However, most reduction reactions, except producing ethanol and methane, are thermodynamically less favored than the HER, especially under high overpotential conditions.[13] Therefore, it is essential to design catalysts that can suppress hydrogen production and selectively promote CO_2 reduction.

1.1.2 Catalyst for the ECO_2RR

Copper-based catalysts have been extensively studied since Hori's discovery that copper can electrochemically reduce CO_2 to hydrocarbons with higher efficiency than other metals.[15] At 0°C, the primary product is CH_4 with a Faradaic efficiency of 65%. As the temperature increases, carbon-carbon coupling is promoted, resulting in a greater formation of C_2H_4.[16]

Over the years, several materials have been employed as electrocatalyst for ECO_2RR, they can be divided in three groups: metallic, non-metallic and molecular catalyst.[17] Monometallic catalyst can be further grouped in four classes according to their main reduction products: (i) Pd, Au, Zn, Ag, and Ga which primarily yield CO; (ii) Hg, Pb, Cd, In, Sn, Bi and Ti selective towards formic acid (HCOOH); (iii) Cu which produces hydrocarbons (such as CH_4 and C_2H_4); (iv) Ni, Pt, Fe, and Ti which form hydrogen.[18]

The key parameters to evaluate the performance of an electrocatalyst are:

- Activity: the ability of a catalyst to increase the reaction rate by lowering the energy barrier. This is often characterized by the exchange current density at the equilibrium potential.
- Faradaic efficiency (FE): it quantifies the fraction of electrons contributing to the formation of a specific product, so it is considered a measure of the selectivity.
- Overpotential: as already discussed, it is the voltage difference between the thermodynamic equilibrium potential and the experimentally applied potential. In an electrolytic cell, overpotential indicates the kinetic and transport barriers of the reaction.
  Table 1 shows the standard potentials (E^0) and the reactions of several common ECO_2RR products.[19]
- Cost: the economic feasibility of the catalyst, which depends on the raw material price and usage, is important for promoting the industrial implementation of ECO_2RR. However, the overall cost depend also on the electrocatalyst stability over time, as more durable as longer time of activity and as higher total production.
- Sustainability: the environmental impact of the materials and the synthesis methods.

Table 1: Standard reduction potentials for key ECO_2RR and OER half-reactions.[19]

Electrode	Reaction	E^0 [V]
Cathode	$CO_2 + 2H^+ + 2e^- \rightarrow CO + H_2O$	-0.106
	$CO_2 + 2H^+ + 2e^- \rightarrow HCOOH$	-0.250
	$CO_2 + 4H^+ + 4e^- \rightarrow HCOH + H_2O$	-0.070
	$CO_2 + 6H^+ + 6e^- \rightarrow CH_3OH + H_2O$	0.016
	$CO_2 + 8H^+ + 8e^- \rightarrow CH_4 + 2H_2O$	0.169
	$2CO_2 + 12H^+ + 12e^- \rightarrow C_2H_4 + 4H_2O$	0.064
	$2H^+ + 2e^- \rightarrow H_2$	0.000
Anode	$2H_2O - 4e^- \rightarrow O_2 + 4H^+$	1.230

Determining all possible ECO_2RR mechanistic pathways and study the intermediate stabilization on different materials is a strategy to improve catalytic system.[20] Over the years, researchers studied the reaction steps both experimentally and theoretically.[21], [22], [23] Today, almost all of the scientists agreed that the first electron transfer is the rate-determining step, which transforms the surface-adsorbed CO_2 in the first intermediate (Equation 1).[24] The next steps depend on which atom binds the electrode surface, Figure 3 shows the two possible pathways.[25]

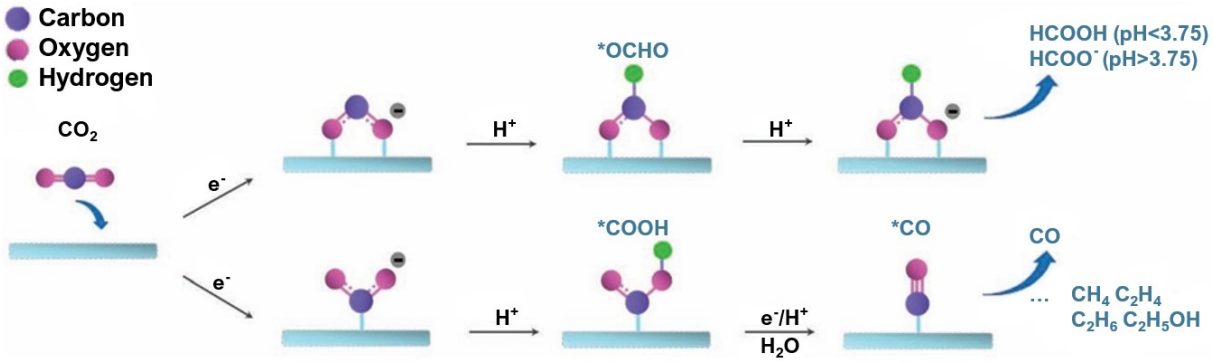

Figure 3: Possible reaction pathways for ECO_2RR to formate, CO, methane and other products.[25]

Adsorption of *OCHO and *COOH intermediates is usually endothermic and requires stabilization by catalyst surface. If a material efficiently stabilizes *OCHO intermediate, it tends to exhibit high selectivity toward formate production. In contrast, if *OCHO is not favored the reaction pathway proceeds through *COOH, leading to the formation of CO, methane, or other C_2^+ products.[25]

Since the CO_2 can be converted into various products, depending on the electrocatalyst used, one rational strategy is to choose a main product and then develop a material that is active and efficient for its formation. The choice of product should consider commercial viability, which depends on different factors: market demand, manufacturing costs and achievable reaction selectivity.[25] Among the possible products, formate stands out as particularly promising:

- Market demand: formate is an crucial chemical intermediate used in many industrial processes, including textiles, food processing, pharmaceuticals. Moreover, it can be used as chemical fuel for fuel cells and it has potential as a liquid for hydrogen storage and transport.[26]

- Manufacturing costs: conventional industrial production of formic acid is costly and energy intensive.[27] Direct electrochemical CO_2 reduction under mild conditions with high energy conversion efficiency offers a potentially more economical alternative. Additionally, recent techno-economic analysis suggest that formic acid is among the most commercially viable ECO_2RR products. Figure 4 shows a price comparison of some ECO_2RR products, based on moles of electrons consumed, without considering electricity and separation costs.[28]

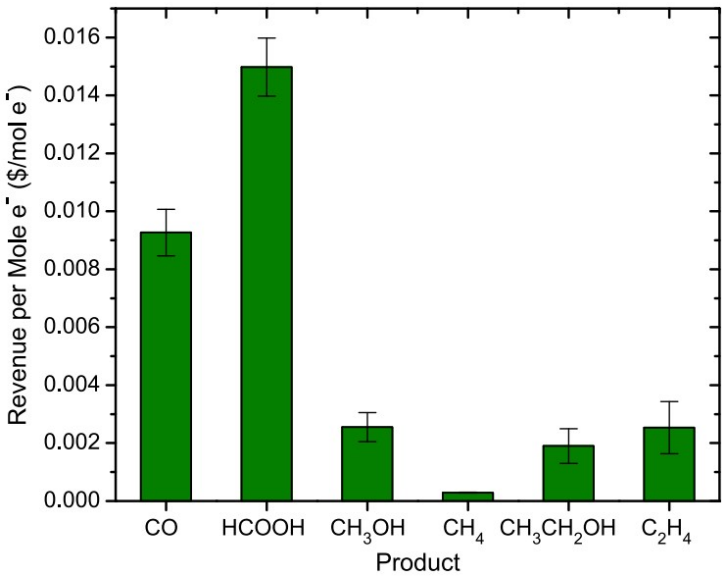

Figure 4: Value generated per mole of electrons consumed for different ECO_2RR products. The market fluctuation, transport, capital, and purification costs are not taken into consideration.[28]

However, product separation remains a significant economic challenge. For formic acid, separation costs account for approximately 70% of the total production cost.[29] Addressing this limitation requires the development and implementation of more efficient technologies.

- Reaction selectivity: FE significantly decreases for products with more than one carbon atom. This is because the carbon-carbon coupling requires the adsorption of multiple CO_2 molecules on surface and their simultaneous transformation, which presents a statistical challenge. In contrast, formate can be produced via simpler pathways involving only a single CO_2 adsorption.

As previously mentioned, p-block metals (in groups 13-16 of the periodic table) such as Sn, Pb, Hg, In and Bi thermodynamically favor the adsorption of *OCOH over *COOH, directing the reaction toward selective formate production. Moreover, these metals generally exhibit poor catalytic activity for the competing Hydrogen Evolution Reaction (HER), further enhancing their selectivity toward formate.[30] Theoretical calculations attribute the higher selectivity of Bi-based catalysts for formate to the greater stability of the O–Bi bond compared to the C–Bi bond.[30]

1.1.3 Bi-based catalyst

Among the p-block metals, bismuth stands out for its low toxicity, environmental sustainability and low cost, thanks to its relatively high natural abundance in the Earth's

crust. Despite these advantages, Bi also exhibits some intrinsic limitations, such as poor electrical conductivity and sluggish reaction kinetics, which can negatively affect its electrocatalytic performance.
To overcome these challenges, a variety of Bi-based electrocatalysts for ECO_2RR have been developed using various methods, including hydrothermal synthesis, chemical or electrochemical reduction and electrodeposition. These approaches have enabled the porduction of catalysts with diverse morphologies and structural features designed to mitigate these drawbacks. The most promising categories include:[31]

- Single atom catalysts (SACs): atomic dispersion maximizes atoms utilization efficiency. SACs can be used as models to further investigate the ECO_2RR mechanisms. However, their application is accompanied by difficulties, including atomic characterization and precise identification of active sites. Furthermore, increasing the bismuth loading and scale-up the synthesis procedure are also critical.

- Nanoparticles (NPs): nano-sized materials exhibit improved catalytic performance compared to the bulk counterpart thank to the larger surface-to-volume ratio and, consequently, reactivity. Further improvements in activity can be achieved by nano-engineering strategies to control morphology and maximize surface area. However, the development of a synthesis procedure that can control the NPs size is critical mainly due to: high bismuth precursors tendency to hydrolyzed to hydroxides in water, forming bismuth oxides, and very low bismuth melting point (271.3 °C), which can lead to the agglomeration of Bi-based nanocrystals under over-heating. The main strategies to overcome these issues include using surface ligands or carbon-based supports.
  The surface ligands adsorb onto the surface of the nanocrystals, preventing aggregation through steric hindrance effect arising from the solvophilic tails. Furthermore, the use of surfactants can improve the control of the NPs size and shape and the exposed facets of the crystals. [32]
  Carbon-based support provide excellent electrical conductivity, high specific surface area and strong chemical stability. By using these materials as support for the Bi-based NPs, both the conductivity and activity of electrocatalysts can be improved.

- 1D nanostructures: these mainly include nanowires (NWs) and nanotubes (NTs). Their synthesis procedure commonly results in ultra-fine crystalline particles with a high density of grain boundaries (GBs) which can enhance selectivity for ECO_2RR. These features make 1D nanostructures promising for electrocatalytic applications in both energy conversion and storage.

- 2D nanostructures: this category includes nanosheets (NSs), nanoflakes, bismuthene and thin films. In recent years, these materials has been largely investigated due to their characteristic large specific surface, high conductivity and rich abundant active sites on the surface and edges.

A literature overview on Bi-based catalyst is given in Table 2.

Table 2: Literature overview on Bi-based electrocatalyst for the ECO_2RR.

Material	Applied potential [V_{RHE}]	$FE_{formate}$ [%]	j [mA/cm^2]	Ref.
Bi NSs	-0.8	94	-4.6	[33]
Bi NSs	-0.83	95	-15.3	[34]
Bi NPs	-0.83	94.7	-4.9	[35]
Bi NTs	-0.85	99	-42	[36]
Bi_2O_3 NPs	-0.9	91	8.0	[37]
Curved Bi NSs	-0.9	92	15.0	[38]
Bi_2O_3-Bi NPs	-0.97	95	5.1	[39]
$(BiO)_2CO_3$-Bi NPs	-1.07	99	6.2	[2]
Bi NTs	-1.1	97 (at -1.0 $V_{RHE)}$)	-39.4	[40]
Bi NSs	-1.1	<80 (at -1.0 $V_{RHE)}$)	-45.6	[40]
Mesoporous Bi NSs	-1.1	100	18.0	[33]

1.2 Thesis outline

The excessive consumption of fossil fuels has led to a rapid increase in atmospheric CO_2 levels, contributing to global warming and climate change. Electrochemical reduction of CO_2 is a promising strategy to mitigate the carbon dioxide emissions and produce value-added carbon-based product. Among the various ECO_2RR products, formate is particularly attractive because of its market demand and its high value generated. Bismuth is recognized as one of the most promising elements for catalyzing ECO_2RR towards formate production. Consequently, the main focus of this research project is the synthesis and the characterization of Bi-based materials. The effect of different synthesis parameters on the physicochemical properties and, consequently, electrochemical performance of the catalysts was investigated.

The first material, BiSub@AC-400, is synthesized following the procedure reported by Miola et al.[2] This electrocatalyst demonstrated nearly complete selectivity toward formate (FE>99%) at an overpotential of 0.88 V, along with high stability over 48h of electrolysis. Additionally, the synthesis method is rapid, cheap and straightforward. The activated carbon (AC) was added to improve the electrical conductivity, limit aggregation maintaining small NPs size, thus increasing the number of active sites per gram of catalyst.
Subsequently, the research focused on synthesizing new materials by modifying the original procedure, specifically by solubilizing the bismuth precursor to improve its interaction with the AC support. This modification aims to enhance the carbon support's effectiveness in limiting aggregation and to promote a more uniform dispersion of Bi on the AC.

The structure of the thesis is as follows:

- Experimental section & methods: detailed information about the materials and synthesis procedures for BiSub@AC-400, BiNPs@AC-SA and BiNPs@AC-AcOH. A brief overview of the characterization techniques employed and the conditions under which they were performed. Explanation of the methods used to analyze the results.
- Results and discussion: this chapter in further divided in the discussion of the physico-chemical and electrochemical characterization.
  In the first section includes the results of XRD, SEM, TEM and TGA of all the ma-

terials. A comparison between the synthesized BiSub@AC-400 and the literature data[2] is provided, addressing reproducibility challenges. The influence of varying synthesis parameters is also investigated.
The second section compares the electrocatalytic performance of the materials, discussing chronoamperometry tests and Faradaic efficiencies determined by HPLC. The relationship between physicochemical properties and electrochemical behavior is analyzed.

- Conclusion and future developments: a summary of key findings is presented, along with recommendations for potential future research directions.

2 Experimental section & Methods

2.1 Synthesis

2.1.1 Materials

Bismuth(III) subsalicylate (99.9%), salicylic acid ($\geq$ 99%), ethanol (96% and 99%) and acetic acid (99.7%) were purchased from Sigma-Aldrich. Norit SX1G activated carbon was purchased from Cabot.

2.1.2 BiSub@AC-400 electrocatalyst

Synthesis procedure

The synthesis is straightforward and fast, it consists of three steps: mixing of the AC with the Bi precursor in solution, drying and pyrolysis. In Figure 5 a representation of the synthesis scheme is shown.[2]

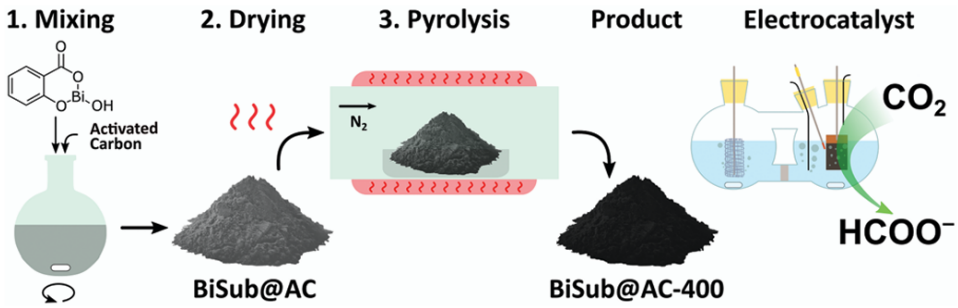

Figure 5: Schematic of the synthesis steps of the BiSub@AC-400 electrocatalyst.

In details, in a round-bottom flask 0.5852 g of BiSub were mixed with 25 mL of ethanol (96%) under stirring for one minute, then 0.5090 g of AC were added to the dispersion. According to Miola et al.[2], the aim of this first step is to allow the interaction between the activated carbon support and the bismuth subsalicylate (wet impregnation). Due to the BiSub structure, characterized by the bidentate coordination of the subsalicylate to the Bi atom and the aromatic backbone, this organic compound should show a strong physisorption on the AC. Figure 6 shows the BiSub structure.

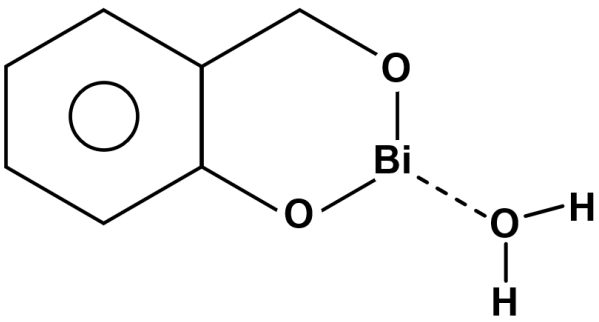

Figure 6: Bismuth subsalicylate structure

After stirring overnight (16 h), the slurry was dried with the rotovap (175 mbar, 40 °C) and then overnight with a oven at 90 °C.

The dried powder was put in a quartz boat (Figure 7) and pyrolyzed in a tubular oven under N_2 flow (100 mL min^{-1}) at 400 °C for 1 h (rate of heating: 25 °C min^{-1}). Before starting the heating, the system was purged with nitrogen at the same flow rate for 10 minutes to ensure complete removal of air from the tube.

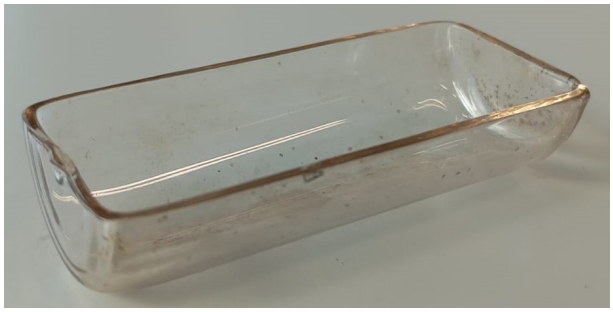

Figure 7: Picture of the quartz boat use during the pyrolysis in the tubular oven

The goal of the pyrolysis is to reduce the organic bismuth precursor to generate metallic bismuth $Bi^{(0)}$ nanoparticles.

2.1.3 BiNPs@AC-SA electrocatalyst

Synthesis procedure

In a round-bottom flask 6.2157 g of SA were mixed with 25 mL of ethanol (99%) under stirring (750 rpm) for 10 minute. Then 0.5852 g of BiSub were added to the solution and stirred for an additional 10 minutes, followed by the addition of 0.5090 g of AC.
The remaining synthesis procedure was carried out following the same steps reported in subsubsection 2.1.2 except for an additional grinding step introduced between the drying in the oven and the pyrolysis. This grinding was performed manually using a mortar and a pestle made of white opal.
This additional step was necessary because, due to the high amount of SA used, the dried material did not form a fine powder.

2.1.4 BiNPs@AC-AcOH electrocatalyst

Synthesis procedure

In a round-bottom flask 12 mL of AcOH were mixed with 13 mL of ethanol (99%), then the BiSub was added to the mixture under stirring (750 rpm). After 10 minutes, 0.5090 g of AC were put into the flask.
At the beginning of the rotovap step, 175 mbar and 40 °C were set. While maintaining the temperature constant, the pressure was slowly reduced to 90 mbar to minimize the bubbles formation. When most of the solvent evaporated, the pressure was slowly reduced to 45 mbar to ensure complete removal of AcOH.
The remaining synthesis procedure was carried out following the same steps reported in subsubsection 2.1.2.

2.2 Physico-chemical characterization

2.2.1 X-Ray Diffraction (XRD)

XRD is an analytical technique used to analyze the structure and the composition of the crystalline phases in the sample, it is also possible to recognize the presence of amorphous phases. The diffractogram of a crystalline material shows different peaks, while that of an amorphous material shows only humps. The position of the peak gives information about the crystal structure and orientation, that's because the X-ray diffraction follow the Bragg's law:

$$n\lambda = 2d \cdot sin\theta \tag{2}$$

Where: n is the order of diffraction (integer, typically 1 or 2), λ is the X-ray wavelength, d is the interplanar spacing of the crystal, and θ is the angle of diffraction. The Figure 8 shows the physical phenomenon.

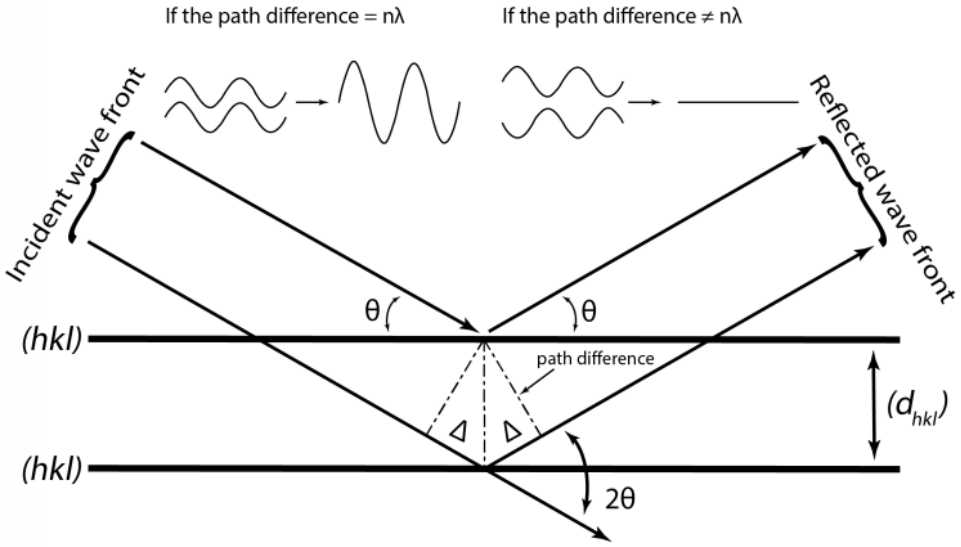

Figure 8: Bragg diffraction phenomenon.

When the Bragg's law is satisfied constructive interference occurs between X-rays scattered from parallel crystal planes, resulting in a detectable peak in the diffractogram. Since each crystal structure is associated with specific families of crystallographic planes (denoted by Miller indices (hkl)), each characterized by a unique interplanar spacing, the positions of the diffraction peaks represent a distinctive fingerprint of the crystalline material.

X-Ray Diffraction (XRD) patterns were recorded on a Bruker D8 Endeavor diffractometer using Cu K-α radiation (λ = 1.541874 Å) at 25 mA and 40 kV. The 2θ scan range was from 5° to 80° (2θ increment = 0.02°) with a step rate of 3757 steps s^{-1}.
The XRD patterns were analyzed using the software DIFFRAC.EVA (developed by Bruker), and the resulting data were plotted with the software Origin. In all graphs, the diffraction patterns were normalized to the intensity of the most intense peak to enable direct comparison among samples.
Peaks deconvolution was performed using the software Fityk. After baseline correction, the diffraction peaks were fitted using the function type 'PseudoVoigt'. Appendix B

presents the peaks fitting and the convolution curves data. The integrated areas of the fitted bismuth peaks were then used to calculate the rhombohedral-to-hexagonal phase ratio by comparing the corresponding peak contributions. In particular, the following equation was applied:

$$rhombohedral - to - hexagonalphaseratio = \frac{Area_{R-Bi}}{Area_{H-Bi}}$$

Where: $Area_{R-Bi}$ and $Area_{H-Bi}$ are the integrated areas of the rhombohedral and hexagonal bismuth peaks, respectively.

Scherrer equation: estamation crystallite size

The crystallite size can be estimated from XRD patterns using the Scherrer equation, defined as follows:

$$L = \frac{K \cdot \lambda}{\beta \cdot cos\theta} \tag{3}$$

Where: L is the mean size of the ordered crystalline domains, K is a dimensionless shape factor (in the following calculations was used the typical value for spherical particles, 0.94), λ is the X-ray wavelength (0.1541874 nm for the Cu K-α radiation), β is the full width at half the maximum intensity in radians and θ is the Bragg angle in radians.
The values β and θ were obtained by the fitting made by the software Fityk, using the procedure previously described.

It is important to underline that the Scherrer equation return an approximate value, as it assumes that the width of the peak depends only on the crystalline domains size even if it is also influenced by the microdeformations and large defects of the lattice.

2.2.2 Scanning Electron Microscopy (SEM)

SEM is a technique used to obtain high-resolution surface imaging by detecting the signals generated from the interaction between a focused electron beam and the sample. There are two distinct signals used for surface imaging: Backscattered Electrons (BSEs) and Secondary Electrons (SEs).
BSEs come from relatively deeper regions of the sample and result from elastic collisions between the incident electrons and atomic nuclei. The BSEs signal gives information about the composition of the sample because its intensity increases with the atomic number of the constituent elements. This is because the higher the atomic number of the element, the greater its probability of interaction with the incident electrons.
In contrast, SEs are generated by the inelastic interaction between the incident electron beam and the electrons in the sample. Due to their relatively low energy, they can only escape from the near-surface region. As a result, SEs signal is highly sensitive to surface morphology and topography, enabling visualization of fine surface features.

SEM and SEM-EDX analysis were performed on an FEI Nova NanoSEM 650 operated at 18 kV with a spot size of 3.5 nm.
The software ImageJ was used to evaluate the range of NPs size.

2.2.3 Transmission Electron Microscopy (TEM)

TEM is a technique used to obtain high-resolution images of the material and, if the sample is thin enough, its internal structure (crystalline plane, orientation and defects) by detecting the electrons that pass through the specimen.

The transmission through the materials is enabled by the high energy of the incident electron beam, by the de Broglie equation (Equation 4) it is clear that higher energy means shorter wavelength and so higher penetration depth.

$$h = p \cdot \lambda \tag{4}$$

Where: h is the Planck's constant ($6.626 \cdot 10^{-34}$ J· s), p is the electron momentum and λ is the electron wavelength.

TEM and STEM-EDX were performed on a FEI Tecnai T20 at 200 keV equipped with a High-Angle Annular Dark-Field detector (HAADF) and an X-max80T EDX detector (Oxford instruments).
For the sample preparation a small amount of electrocatalyst was added to ethanol 99% to obtain a dispersion with very low concentration, then it was dropcasted on the Cu TEM grid.

2.2.4 Energy-Dispersive X-ray spectroscopy (EDX)

EDX is a technique that can be coupled with both SEM and TEM to provide qualitative and quantitative elemental analysis. The X-rays production is due to the interaction between the electron beam and the sample, specifically through inelastic collisions between the incident electrons and the electrons within the atoms of the material.
The energy transfer allows the ionization of the atoms, wherein an electron, called photoelectron, is ejected from an inner shell of the atom, creating an electron vacancy. This ionized state is energetically unstable, so the atom regains stability through a relaxation process, during which an electron from an outer shell fills the vacancy. The difference in binding energies between the two shells is released as a characteristic X-ray photon. The energy of the emitted X-ray depends on the electronic transition involved and is therefore unique to each element, enabling both elemental identification and quantification. Figure 9 illustrates the process when an interaction with an electron in the K shell is indicated.

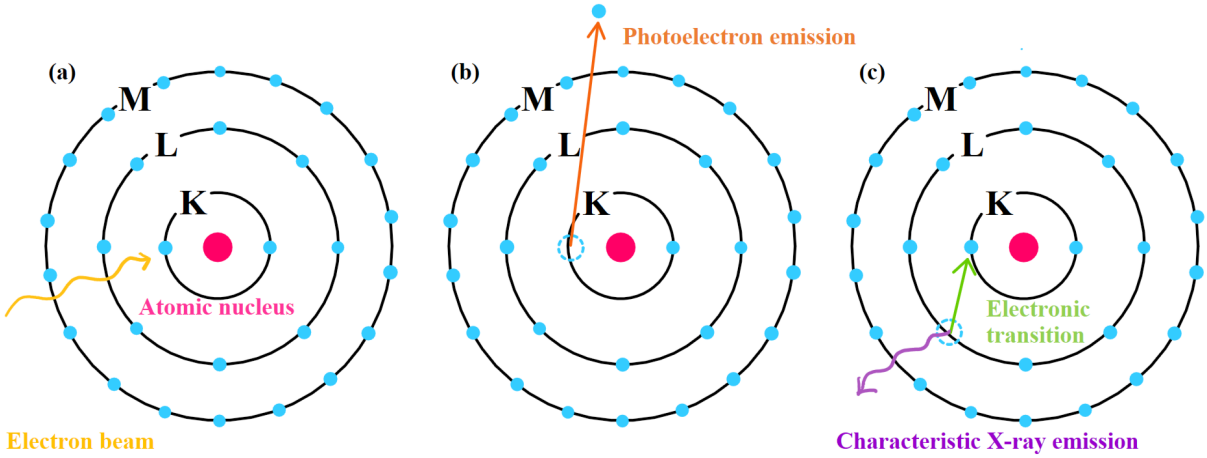

Figure 9: Production of characteristic X rays. (a) Excitation of a K-orbital electron. (b) Emission of a photoelectron producing a vacancy. (c) Relaxation process: electron transition and consequent the emission of a characteristic K photon.

2.2.5 Thermogravimetric Analysis (TGA)

TGA is a thermal analysis that measures the change in mass of the sample as a function of temperature or time, it is used to understand the thermal stability, composition, and decomposition kinetics of the material.

Thermogravimetric analysis was performed on a thermogravimetric analyser TGA4000 from Perkin Elmer under air and with a temperature ramp of 10 °C min^{-1} from 25 °C to 900 °C.
The Derivative Thermogravimetric (DTG) curve was obtained from the TGA data using Origin software. Due to the presence of significant noise, likely resulting from the high heating rate applied during the measurement, the DTG signal was smoothed using the 'Loess' (Locally Estimated Scatterplot Smoothing) method, with a span parameter set to 0.1 to preserve key features while reducing high-frequency fluctuations. Appendix F shows the DTG curves of the TGA performed on all the materials.

Estimation of Bi %wt

First of all the AC was tested to measure its weight loss % at 900 °C. Then, assuming that in the electrocatalysts the removal of the carbon phase is the same and that all the bismuth is in the oxidized form (Bi_2O_3), the Bi wt% can be calculated with these equation:

$$\begin{aligned} Bi_2O_3wt\% &= \%weightloss_{AC} - \%weightloss_{electrocatalyst} \\ Biwt\% &= Bi_2O_3wt\% \cdot \frac{MW_{Bi}}{MW_{Bi_2O_3}} \end{aligned} \tag{5}$$

The theoretical value of Bi %wt expected, assuming a complete decomposition of BiSub during the pyrolysis step and that all bismuth remains in the metallic form, can be measured using the following equation:

$$Bi\%wt = \frac{m_{BiSub} \cdot \frac{AW_{Bi}}{MW_{BiSub}}}{m_{BiSub} \cdot \frac{MW_{Bi}}{MW_{BiSub}} + m_{AC}} \tag{6}$$

Where: m_{BiSub} and m_{AC} are the mass ([g]), of BiSub and AC respectively, used for the synthesis, AW_{Bi} and MW_{BiSub} are atomic and molecular weight ([g mol^{-1}]) of Bi and bismuth subsalicylate respectively. The second assumption is necessary because it is difficult to estimate the final oxygen content, it depend on the time of air exposure and on the NPs reactivity, that is influenced by the NPs size and crystallinity.

2.3 Electrochemical characterization

2.3.1 Materials

Sodium bicarbonate ($NaHCO_3$), Ethanol (96%), Nafion 117 (5 wt%) and DMSO (≥ 99.9%) were purchased from Sigma Aldrich. DI water.
SIGRADUR G glassy carbon (GC) plates was purchased from HTW, used as working electrode. Polishing paper (3 and 1 µm), Teflon tape and liquid electrical tape were used for its preparation.
A Pt mesh, used as counter electrode, and an Ag/AgCl (3.5 M KCl) reference electrode.
A Nafion membrane, that allows the diffusion of protons between the two half cell.

A plastic micropipette tip to flow the CO_2 in the cell during the electrochemical test. An H-cell set up was used to perform all the experiments, in Figure 10, two picture of the real setup are shown.

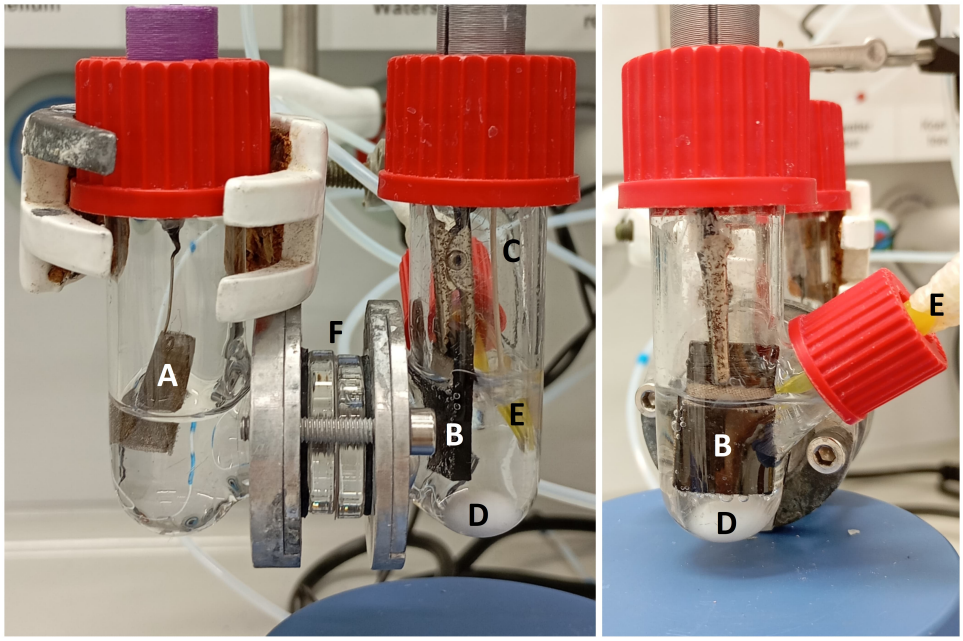

Figure 10: Front and side view of the H-cell used for the chronoamperometry. List of the elements: A. Pt-mesh counter electrode, B. Working electrode, C. Ag/AgCl reference electrode, D. Stirring egg, E. Gas inlet and F. Nafion membrane.

2.3.2 Electrode preparation

Procedure

Before starting it can be useful to make a groove on the top of the GC electrode, it can improve the holding of the crocodile clip.

The GC plate was polished with the 3 and 1 µm polishing paper, then it was coated with adhesive Teflon tape to cover everything except for the top of the electrode and the active surface area (1.69 cm^2). In Figure 11 the front, side and back views of the GC electrode are showed.

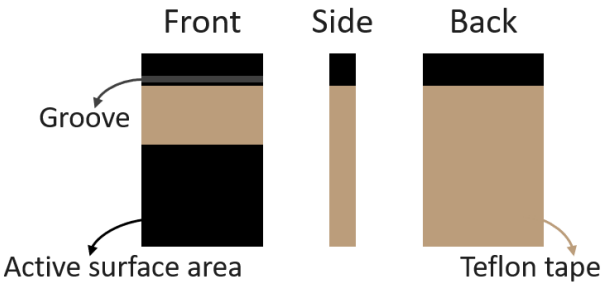

Figure 11: Scheme of the front, side and back views of the GC electrode coated with the Teflon tape.

The liquid electrical tape was used to cover the edges of the electrode to prevent excessive

exposure of the GC surface.
The GC electrode is now ready for drop casting, the method used to deposit the electrocatalyst on the active surface area.
To prepare the ink, 12 mg of the electrocatalyst were mixed with 1080 µL of 96% ethanol and 120 µL of Nafion 117 and then it was sonicated for 1 h in an ultrasound bath. After sonication, the suspension was drop-casted on the GC plates and allowed to dry in a fume hood for 2 h. The theoretical final catalyst loading was 0.296 mg cm^{-2} for all the experiments (50 μL of ink), with the exception of one test conducted at a higher loading of 0.385 mg cm^{-2} (63.62 μL of ink) to enable direct comparison with the reference study by Miola et al.[2].

2.3.3 Electrochemical characterization

Chronoamperometry (CA)

The chronoamperometry is an electrochemical test used to study the behavior of an electrochemical cell by measuring the current response over time at a constant applied potential.
In this project, the constant-potential CA was used to evaluate and compare the activity of the synthesized electrocatalysts. The comparison is possible by applying the same potential, the measured current and the activity of the electrocatalyst are proportional.

The analysis were performed with a Gamry Interface 1000 potentiostat.

The electrochemical cell was prepared by filling both the half cell with 7 mL (approximately 7.2 g) of an aqueous electrolyte 0.5 M $NaHCO_3$. Before starting the test, the stirring was turn on and a constant CO_2 bubbling of 50 sccm was maintained for 10 minutes to saturate the electrolyte. Upon CO_2 saturation, the electrolyte pH changed from pH = 8.4 to pH = 7.3; the pH was measured with a pH meter (Mettler Toledo).

The chronoamperometry was performed at -1.7 V vs. Ag/AgCl (RE) for 30 minutes, keeping the stirring and the bubbling of CO_2 constant.
To compare different materials it is useful to convert the applied potential to vs. RHE (Reversible Hydrogen Electrode). The conversion can be done using the following equation:

$$\begin{aligned} E(V_{Ag/AgCl}) =& E(V_{RHE}) - E^0_{Ag/AgCl}(V_{NHE}) - 0.059 \cdot pH \\ & E^0_{Ag/AgCl}(V_{NHE}) = 0.198V \end{aligned} \tag{7}$$

The obtained value, considering the experimental conditions, is -1.07 V vs. RHE.

After the analysis the anolyte and the catholyte were collected to analyze the CO_2 conversion. Anolyte was collected to investigate if any crossover of ECO_2RR liquid product occurred. Analysis and quantification of the CO_2 conversion products was performed through the High Performance Liquid Chromatography.

For the data analysis, since the Gamry output is the current (I [A]) Excel was used to calculate the current density (j [A/cm^2]). Then Origin was used to plot j vs. t to show how the activity changes over time. Since each material was tested three times to evaluate the reproducibility of the electrochemical test, Origin was used to measure the mean curves and the standard deviations. The average value of current density was measured using the data of the mean curves in the last 10 minutes of the chronoamperometry test to

exclude the initial transitory. The electrocatalytic activity normalized per bismuth mass was measured using this equation:

$$Activityperweight = \frac{Partialj_{formate}}{Massloading_{Bi}} = \frac{Averagej \cdot FE_{formate}}{Catalystloading \cdot Surfacearea \cdot \%wt_{Bi}} \quad (8)$$

Where: $\%wt_{Bi}$ is the weight concentration of bismuth measured by the TGA analysis, so the unit of the activity per weight is mA cm^{-2} mg^{-1}.

Potentiostatic Electrochemical Impedance Spectroscopy (EIS)

Potentiostatic EIS was used to measure the uncompensated resistance (R_u) before each test. The R_u represents the ohmic resistance in the electrochemical system and includes the resistance of the electrolyte between the reference and the working electrode. It may also include minor contributions from connection cables and the intrinsic resistance of the working electrode itself.[41]
The R_u can influence the current measured during a CA measurement due to Ohm's law:

$$V = IR \quad (9)$$

Thus, measuring R_u via potentiostatic EIS helps improve the reproducibility of CA measurements with a given electrocatalyst and enhance the reliability of comparisons between the activity of different materials. As a good practice, R_u should be maintained within a narrow range of $\pm 0.5\Omega$. If the measured resistance goes beyond this threshold, it may indicate issues such as incorrect relative position of the WE and the RE in the cell or poor electrical connection due to misplacement of the crocodile clamp or to presence of rust on the connectors.
The EIS condition were: a DC voltage of $0V$, an AC signal amplitude $10mV(rms)$, a frequency range from $100kHz$ to $10kHz$ and a resolution of $10Points/decade$.

2.3.4 High-Performance Liquid Chromatography (HPLC)

The HPLC is one of several chromatographic methods for the separation and analysis of chemical mixtures, all techniques have in common the principle by which compounds are divided. A moving phase, either a liquid or a gas, carries the sample through the stationary phase, also called column. All compounds in the sample can interact, physically or chemically, with the stationary phase; due to their different affinities they pass through the column at different speeds so they have specific retention time and became separated. At the end of the column there is a detector, there are different methods of detection and the most common are ultraviolet absorption or mass spectrometry. The resulting signal plotted against time is the chromatogram, which can give information about the concentration of the different species in the sample. By the retention time, it is possible to identify the molecules.[42]

The HPLC analysis was carried with an Agilent Technologies 1200 series equipped with Bio-Rad Aminex HPX-87H 300 × 7.8 mm column at T = 60 °C with 0.5 mM aqueous H_2SO_4 eluent (flow rate: 0.55 mL min^{-1}) and a refractive index detector.

Sample preparation

First of all, 1 g (1000 μL) of the electrolyte was filtered using a PTFE filter (0.2 μm)

and placed in a GC-vial. Then, 0.5 g (500 μL) of the internal standard aqueous solution (0.5 M $NaHCO_3$, 0.03 M DMSO) were added to the electrolyte in the GC-vial.

Calibration curve method: evalutation $FE_{formate}$

The calibration curve method is a widely used approach in HPLC to quantify the concentration of a specific analyte in a sample.
To apply this method, the first step is the preparation of at least five standard solutions containing known concentrations of the analyte of interest. After the HPLC analysis, the calibration curve is realize by plotting the peak areas, that can be measured by the chromatographs, against the corresponding analyte concentrations.
To improve accuracy and reproducibility of this method, by compensating the variations in injection volume and chromatographic conditions, a known concentration of an internal standard (IS) can be added to both the standard solution and the unknown samples. In this case, the calibration curve relates the ratio of analyte concentration to internal standard concentration with the ratio of their respective peak areas. The data are tipically fitted using a linear regression, as shown in the following equation:

$$\frac{AREA_{analyte}}{AREA_{IS}} = m \cdot \frac{[analyte]}{[IS]} + b \tag{10}$$

Where: $AREA_{analyte}$ and $AREA_{IS}$ are the peak area of the molecule of interest and internal standard, respectively, $[analyte]$ and $[IS]$ are the respective concentration, m is the line slope and it accounts for the sensitivity factor of the different compounds toward the detection method (RID or UV) and b are the line intercept received by the linear regression analysis.
Once the calibration curve has been established, the concentration of the analyte in an unknown sample can be determined by measuring the ratio of peak areas between the analyte and the internal standard, and using the known concentration of the IS to solve the calibration equation. The data and the calibration curve used are shown in Appendix G.

In this work, the analyte of interest was the formate and the internal standard was the DMSO. The HPLC gave the concentration of formate in the sample, by this value it was possible to calculate the concentration in the catholyte and the total formate moles produced during the chronoamperometry test. The charge necessary to produced a known moles of formate can be measured using this equation:

$$Q_{HCOO^-} = 2 \cdot F \cdot n_{HCOO^-} \tag{11}$$

Where: F is the Faraday constant (96485.3 $C \cdot mol^{-1}$), n_{HCOO^-} are the produced moles of formate and 2 is the number of electrons involved in the reduction reaction.
The faradaic efficiency of the electrocatalyst toward formate can now be determined using the following equation:

$$FE_{HCOO^-} = \frac{Q_{HCOO^-}}{Q} \cdot 100 \tag{12}$$

Where: Q is the total charge measured during the chronoamperometry test, that was measured integrating the curve that represent the current over time.

Appendix G presents the data for the Faradaic efficiency calculation.

3 Results and discussion

3.1 Physico-chemical characterization

3.1.1 Reproducibility of BiSub@AC-400

The material synthetized by Miola et al. was tested by XRD, the analysis showed that it consisted of three main crystalline phases: bismutite ($(BiO)_2CO_3$), bismuth and bismuth oxide (Bi_2O_3). Using the TEM analysis, dispersed Bi NPs were observed and an average NPs size of 5.5±2 nm was measured. Furthermore, the weight concentration of bismuth, measured using the TGA in air and ICP-OES elemental analysis, was 41.5% and 47% respectively. Figure 12 shows the XRD, TEM and TGA analysis made by Miola et al.[2]

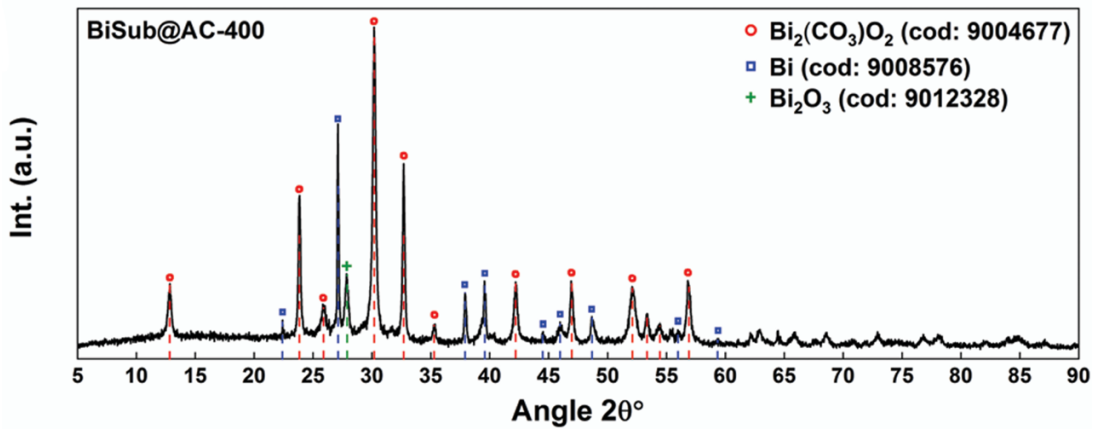

(a) XRD characterization of BiSub@AC-400.

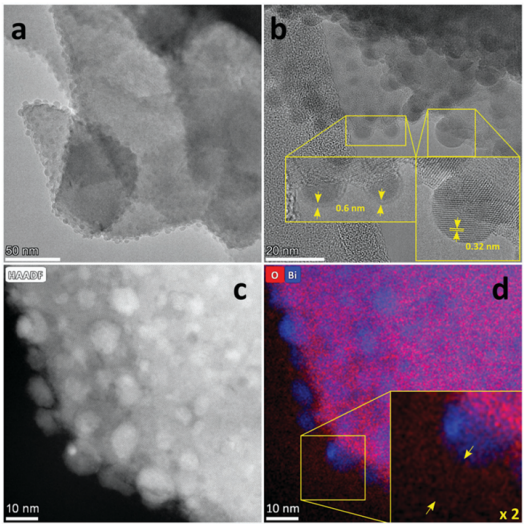

(b) (a) HR-TEM pictures of BiSub@AC-400: with (b) focus on the crystal lattice and the surface of the nanoparticles; (c) HAADF-STEM and (d) EDX-STM pictures.

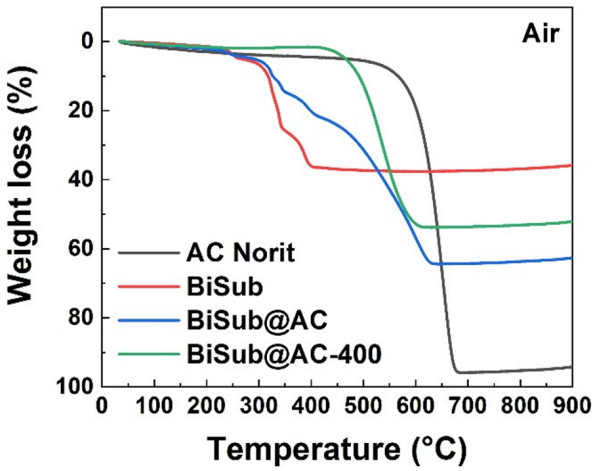

(c) TGA analysis in air of AC, BiSub, BiSub@AC and BiSub@AC-400.

Figure 12: XRD and TEM characterization and TGA analysis made by Miola et al.[2]

Following the synthesis procedure reported on the paper, issues with reproducibility were encountered; to solve them one parameter of the synthesis at a time was changed. However, all the obtained materials were similar between each other but still different from the results of Miola et al.[2] Further discussion about the dissimilarities follows in this chapter.

Table 3 presents all the materials BiSub@AC-400 synthesized with an identification code and shows the parameters changed.

Table 3: Samples of BiSub@AC-400 list with identification code.

Code	BiSub powder	Stirring rate	Pyrolysis
MA001	OLD	LOW	NO CAP
MA002			CAP
MA003	NEW		NO CAP
MA004		750 rpm	

MA001, MA003 and MA004 were synthetized following the procedure reported by Miola et al.; in fact, the stirring rate was not specified. For MA002 only one parameter was changed, the reason will be explained later in the discussion.

Figure 13 shows the XRD patterns of the all materials. Three crystalline phases are identified: metallic bismuth (COD: 9008576), metallic bismuth (COD: 5000215) and bismuth oxide (Bi_2O_3, COD: 9012327). The two bismuth phases belong to the same space group ($R\bar{3}m$) but differ in their unit cell geometry, rhombohedral and hexagonal, respectively. Although both structures exhibit the same symmetry, their unit cells differ in size and shape.[43] Compared to the XRD analysis reported (Figure 12), all the obtained materials do not consist of bismutite and, moreover, hexagonal bismuth is detected.

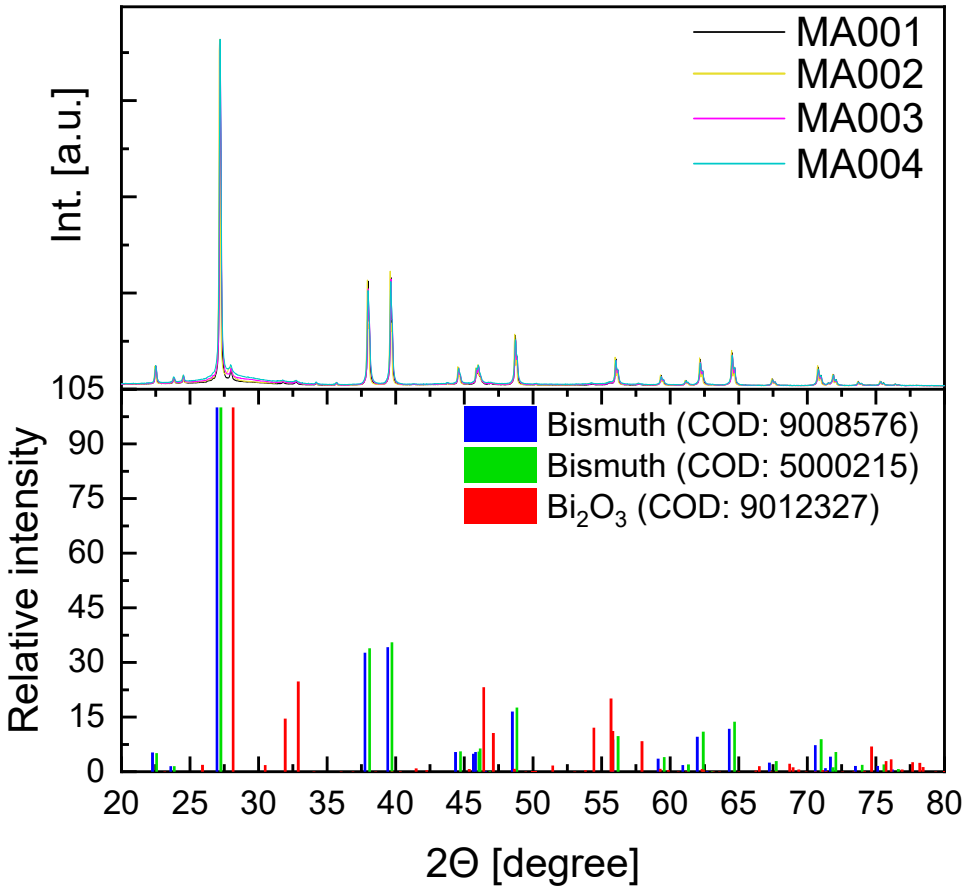

Figure 13: XRD patterns of MA001, MA002, MA003 and MA004. All the XRD patterns were normalized on the height of the highest peak of each material.

Bismutite ($(BiO)_2CO_3$) is likely formed as a decomposition product of BiSub ($C_7H_5BiO_4$) during thermal treatment. So, its presence in BiSub@AC-400 is expected to be associated with the pyrolysis step.
Previous studies have reported the formation of $(BiO)_2CO_3$ from a CO_2-absorbing Bi_2O_3 precursor in solution.[44], [45] Even if no direct synthesis of bismutite under CO_2-rich and dry conditions has been documented, it is plausible that a higher local CO_2 partial pressure could inhibit the thermal decomposition of $(BiO)_2CO_3$ into Bi_2O_3 during pyrolysis.
Based on this hypothesis, the material MA002 was synthesized by covering the quartz boat with a cap during the pyrolysis in the tubular oven (Figure 14). This modification aimed to reduce the efficiency of the N_2 flow in removing gaseous decomposition products, thereby potentially maintaining a higher CO_2 concentration around the sample and stabilizing bismutite from further thermal degradation.

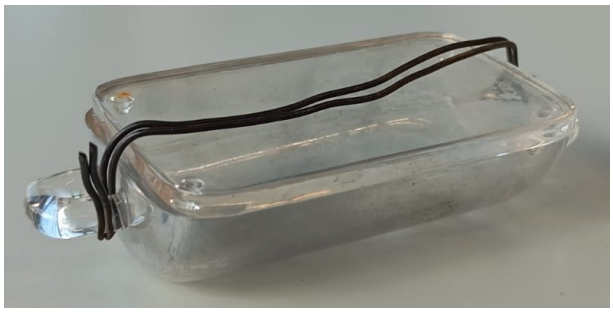

Figure 14: Picture of the quartz boat with the cap used during the pyrolysis in the tubular oven.

However, comparing the XRD graphs of MA001 and MA002, the detected crystalline phases are the same and the relative intensity of the peaks is similar.

Given that both MA001 and MA002 differed from the material described in the reference article (Figure 12), additional tests have been done directly on the bismuth subsalicylate powder to verify that it had not degraded. In fact, Bi(III) is known to be strong Lewis acid and can undergoes hydrolysis.[46] Since BiSub is widely used as an antimicrobial and anti-inflammatory agent, its hydrolysis has mainly been studied under gastric conditions, where it decomposes to form salicylic acid and bismuth oxychloride.[47] However, in a high-moisture environment over an extended period (notably, the batch of BiSub was opened in 2020), BiSub could also hydrolyze to yield bismuth hydroxide and salicylic acid, as shown in the following reaction:

$$Bi(C_7H_5O_4)_3) + H_2O \rightarrow Bi(OH)_3 + 3C_7H_6O_3$$

Both XRD and H-NMR analysis were performed to investigate potential degradation of the BiSub powder, comparing the old batch with a new one. The results of these analysis are presented in Appendix A; however, it remains inconclusive whether the old powder had actually degraded. Consequently, the material MA003 was synthesized using the new batch of BiSub. However, its XRD pattern still appears similar to those of MA001 and MA002 (Figure 13).

The Scherrer equation was used to estimate the crystallite size of the samples, for each material the most intense diffraction peak of every crystalline phase was used in the calculation (around 27°-28° 2θ). The estimated crystallite sizes for all samples are presented

in Figure 15. Appendix B shows the fitting of XRD peaks, made with the Pseudo-Voigt curves, for each material.

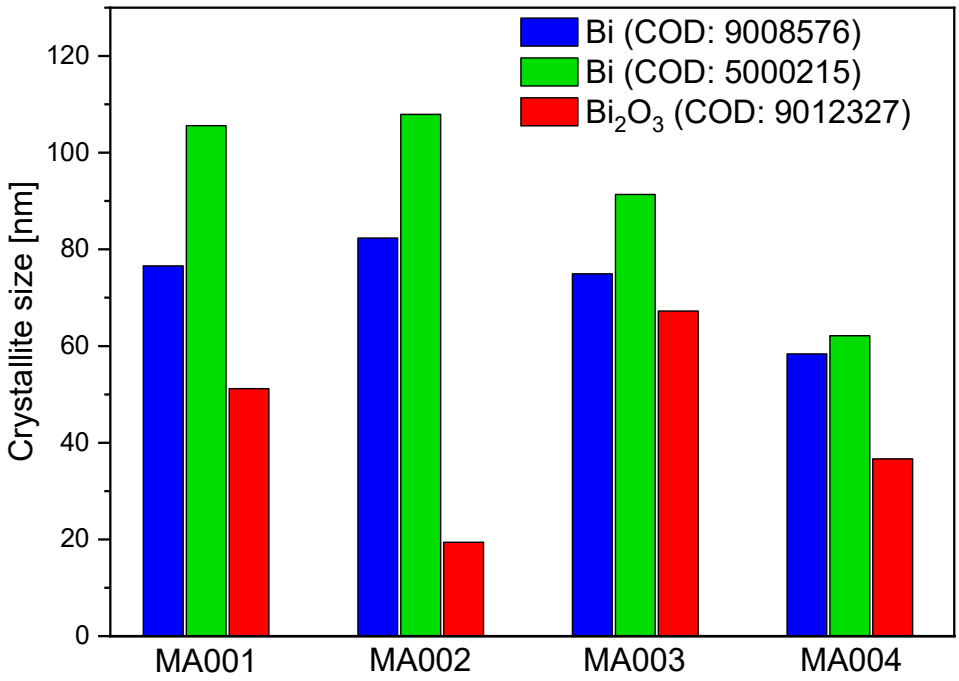

Figure 15: Estimation of crystallite size of the crystalline phases present in the BiSub@AC-400 materials.

According to the reference study, the average diameter of the nanoparticles (NPs) is reported to be 5.5 ± 2 nm. Therefore, the crystallite size is expected to be below this value.[2] However, MA001, MA002 and MA003 have a crystallite size estimation of both bismuth and bismuth oxide between 20 and 100 nm, suggesting the formation of larger nanoparticles.

Several studies on different materials, including inorganic and hybrid organic-inorganic solids[48], [49], [50], metals[51], [52], [53] or oxides[54], [55], [56], have shown that the mechanical agitation influences both the size and the shape of materials. In an attempt to reduce the NPs size, material MA004 was synthesized using a higher stirring rate of 750 rpm. The XRD pattern of MA004 (Figure 13) confirms the presence of the same crystalline phases observed previously. Although the estimated crystallite sizes are slightly reduced (Figure 15), they remain substantially larger than the nanoparticle sizes reported in the reference study.[2]

Since the Scherrer equation provides only an estimation of crystallite size, the NPs size was verified via SEM analysis. Figure 16 shows SEM images of MA001, MA003 and MA004 with different magnification.

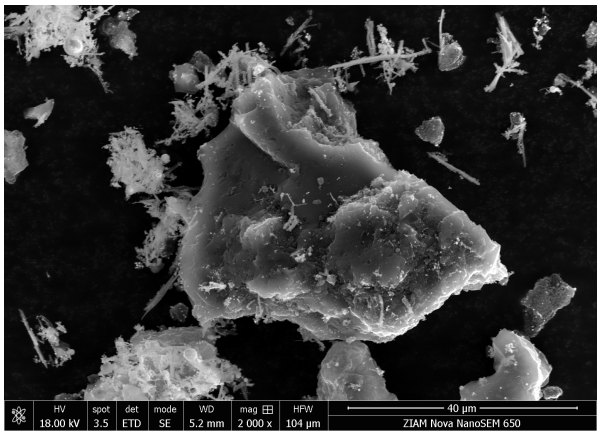

(a) SEM image of MA001 at 2000 x magnification.

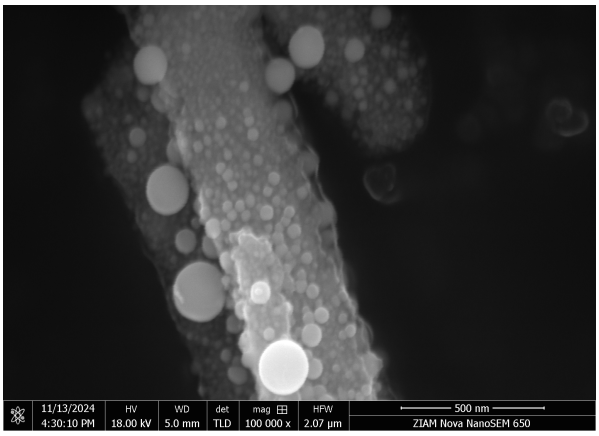

(b) SEM image of MA001 at 100000 x magnification.

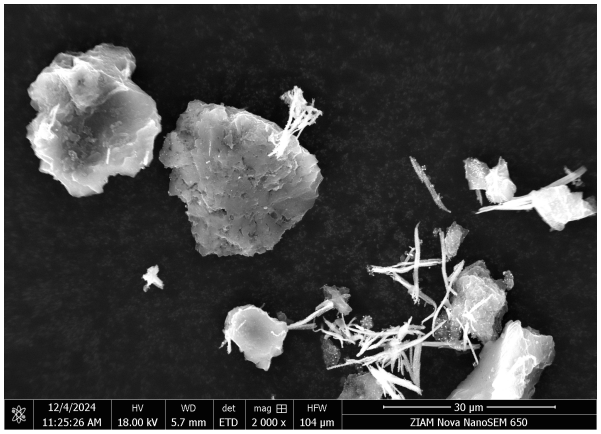

(c) SEM image of MA003 at 2000 x magnification.

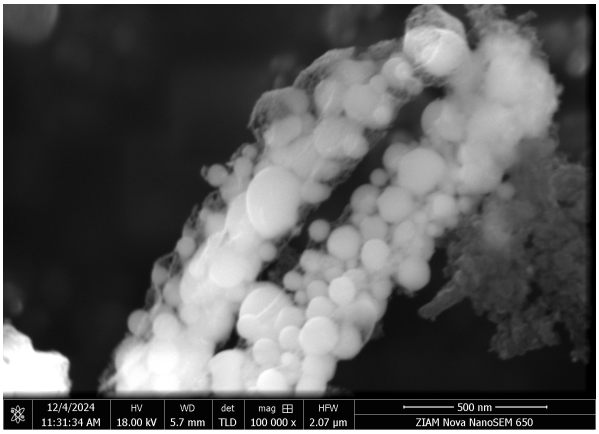

(d) SEM image of MA003 at 100000 x magnification.

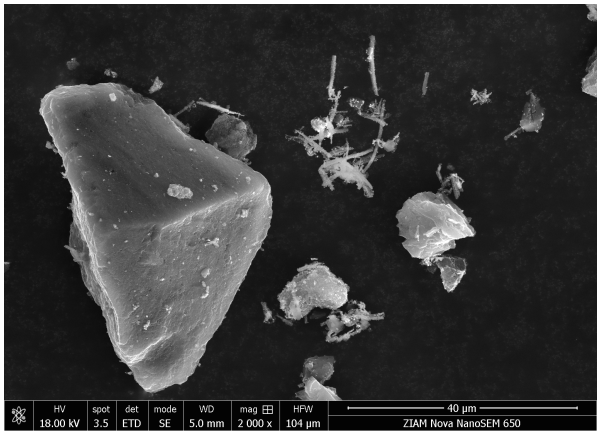

(e) SEM image of MA004 at 2000 x magnification.

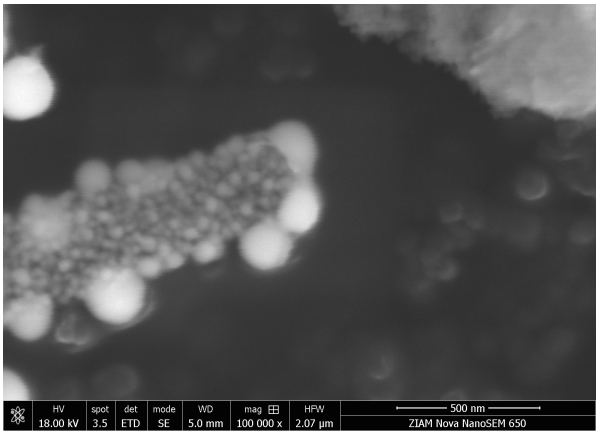

(f) SEM image of MA004 at 100000 x magnification.

Figure 16: SEM images at different magnification of MA001, MA003 and MA004.

A broad size distribution of nanoparticles was observed in all the materials analyzed. The measured diameter ranges, obtained by ImageJ software, are as follows: in MA001 is from about 200 nm to less than 25 nm, in MA003 from more than 200 nm to about 30 nm and in MA004 from about 200 nm to 20 nm. The NPs size of MA004 is similar to MA001 and MA003, this result suggests that the stirring rate influences more the crystallite than the particle size.

These observations are consistent with the results obtained from the Scherrer equation, confirming that the average bismuth nanoparticle sizes in the synthesized materials remain larger than those reported in the reference study.[2]
Low-magnification SEM images reveal that all the materials share a similar morphology, characterized by two distinct regions: one attributable to the AC, as confirmed by comparison with SEM images of the bare AC shown in Appendix C, and another comprising rod-like structures. Higher-magnification images of these rods (Figure 16b, 16d, 16f) show that they consist of agglomerated NPs connected together into elongated formations, giving rise to their characteristic morphology.
To investigate the composition of the rod-like structures, SEM-EDX analysis were performed on samples MA001 and MA003. Figure 17 presents the regions selected for analysis and their corresponding elemental distributions.

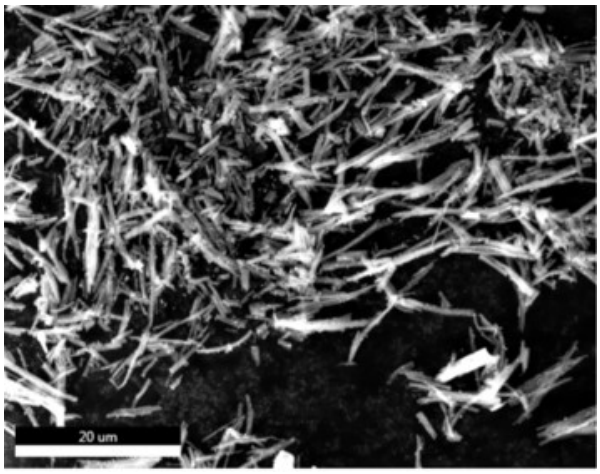

(a) SEM image of the area of analysis of MA001.

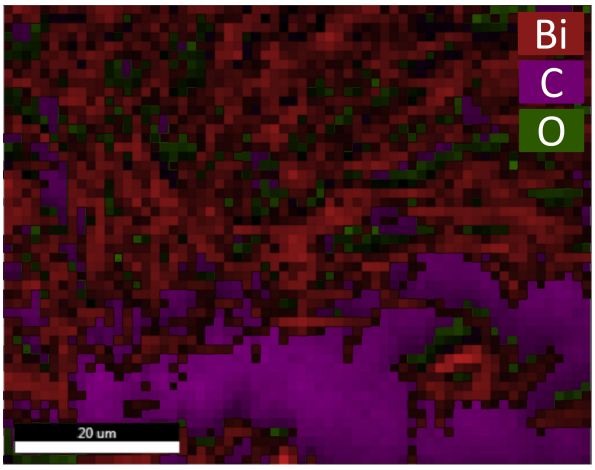

(b) Elemental distribution map of MA001.

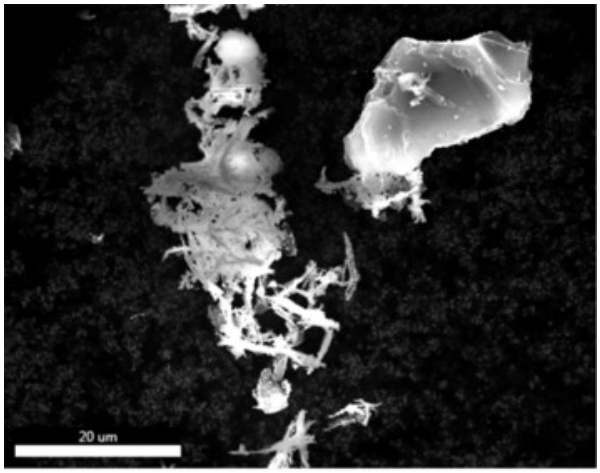

(c) SEM image of the area of analysis of MA003.

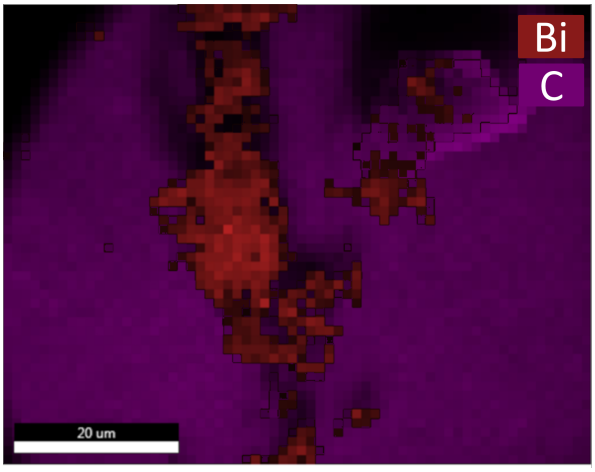

(d) Elemental distribution map of MA003.

Figure 17: SEM-EDX of the MA001 and MA003.

The element compositions obtained from the SEM-EDX analysis are as follow: for MA001, 58.6 wt% carbon, 29.0 wt% bismuth, and 12.4 wt% oxygen; for MA003, 90.4 wt% carbon and 9.6 wt% bismuth. It is important to note that a significant portion of the detected carbon originates from the adhesive tape used to secure the material to the sample holder. However, in both Figure 17b and Figure 17d, the rod-like structures exhibit a relatively

high bismuth content. These SEM and SEM-EDX findings indicate a correlation between morphological features and elemental heterogeneity.
STEM-EDX analysis were performed on MA004, to avoid the carbon signal from the sample holder a holey copper grid was used. Figure 18 shows the results.

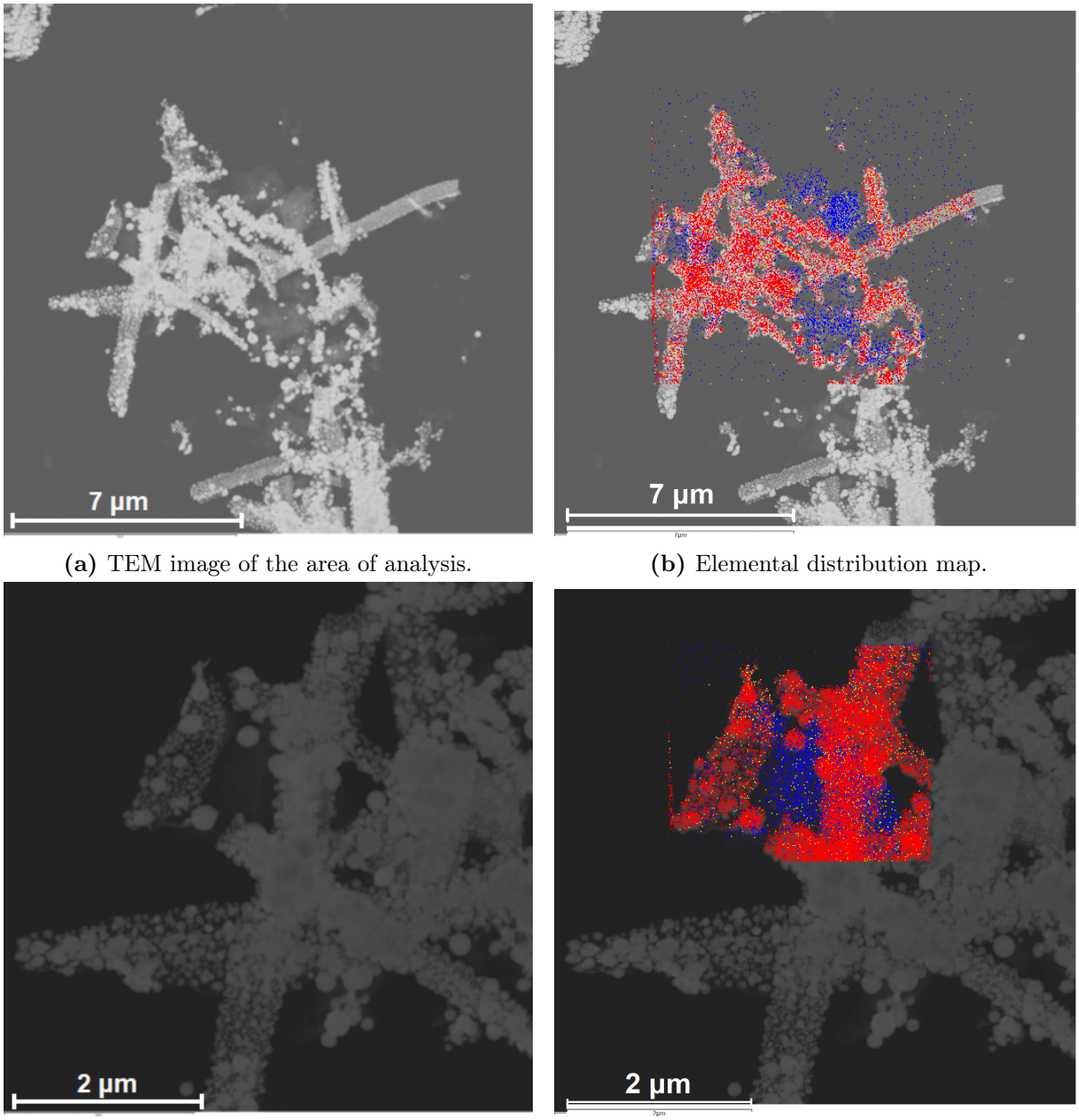

(a) TEM image of the area of analysis.

(b) Elemental distribution map.

(c) TEM image of the area of analysis.

(d) Elemental distribution map.

Figure 18: STEM-EDX analysis of the MA004.

The element composition obtained from the STEM-EDX analysis are: 14.55 %wt of carbon, 83.76 %wt of bismuth and 2.69 %wt of oxygen in Figure 18b and 11.4 %wt of carbon, 86.5 %wt of bismuth and 2.1 %wt of oxygen in Figure 18d. As shown in Figure 18 the elemental distribution within the material is non-uniform. The AC regions are predominantly composed of carbon, whereas the rod-like structures consist mainly of bismuth. It looks like there is no good interaction between the BiSub and the AC, even if we expected, based on the literature, small Bi NPs on the AC.[2]

The low bismuth content observed on the AC surface was hypothesized to result from the low solubility of BiSub in ethanol (96%). Based on this assumption, the new materials BiNPs@AC-SA and BiNPs@AC-AcOH were synthesized by modifying the solution to improve BiSub solubility. The synthesis procedures are described in detail in section 2, while the discussion of their physico-chemical properties is presented in subsubsection 3.1.2.

In conclusion, the BiSub@AC-400 was not reprodubible, mainly due to the absence of bismutite ($(BiO)_2CO_3$). The origin of bismutite in previously synthesized samples remains uncertain, and two main formation pathways can be hypothesized: (i) it may be a decomposition product of the bismuth subsalicylate, or (ii) it may form through a reaction between metallic bismuth or Bi_2O_3 and the activated carbon during pyrolysis.
The first hypothesis is supported by TGA analysis performed under both N_2 and air flow by Miola et al.[2], where BiSub shows multiple degradation steps. Notably, the final step start around weight loss of approximately 27-28%, which is similar the theoretical weight loss expected for the transformation of two BiSub molecules into one bismutite unit. This can be estimated by the following expression:

$$Weightloss\% = \frac{2 \cdot MW_{BiSub} - MW_{Bismutite}}{2 \cdot MW_{BiSub}} \cdot 100 = 29.3\%$$

Where: MW_{BiSub} and $MW_{Bismutite}$ are the molecular weight of BiSub (362.09 g mol^{-1}) and bismutite (511.99 g mol^{-1}) respectively. The factor '2' accounts for the two Bi atoms present in one formula unit of bismutite ($(BiO)_2CO_3$), assuming two BiSub molecules are needed for its formation. The TGA analysis under N_2 is shown in Figure 19.

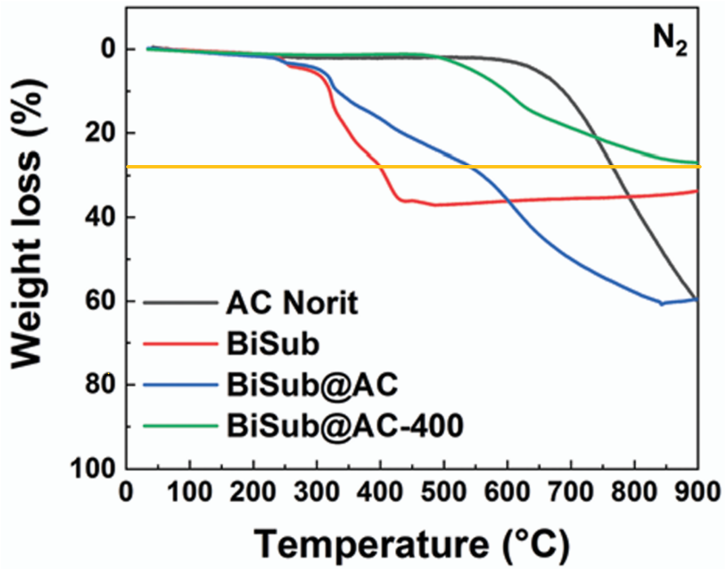

Figure 19: TGA analysis under N_2 flow of AC, BiSub, BiSub@AC and BiSub@AC-400.[2] The yellow line approximately indicates the onset of the final degradation step, which may correspond to the formation of bismutite.

The second hypothesis is supported by bismuth content measurements reported by Miola et al., based on both TGA in air and ICP-OES elemental analysis, which yielded Bi concentrations of 41.5 wt% and 47 wt%, respectively.[2] For comparison, the theoretical Bi loading, calculated using Equation 6 and assuming complete decomposition of BiSub,

is approximately 40 wt% Bi and 60 wt% C. The fact that the experimentally measured Bi content exceeds the theoretical value suggests that BiSub was indeed fully decomposed during pyrolysis. However, the formation of $(BiO)_2CO_3$ from either metallic Bi or Bi_2O_3 has been reported in solution-based processes, including solvothermal synthesis from Bi_2O_3[57] and electrochemical methods using both Bi[58] and Bi_2O_3[44] as precursors. Consequently, further investigation is needed to elucidate the mechanism of bismutite formation under pyrolytic conditions and to identify the key parameters, such as temperature, atmosphere and flow rate, that influence its nucleation and growth.

3.1.2 Solubilization BiSub: BiNPs@AC-SA & BiNPs@AC-AcOH

The structure of BiSub is still under debate, it was studied over the years because it can affect stability and solubility of the compound.[59] The BiSub is a crystalline compound made from bismuth cations (Bi^{3+}), oxygen (O^{2-}) and salicylate ($Hsal^-$) anions. Based on the study made by E. Svensson Grape et al., the Bi^{3+} can partially deprotonate the carboxylate groups.[59] For this reason, the BiSub is soluble in acidic solution because the H^+ in the solution can protonate the salicylates releasing the bismuth cations.
It was decided to dissolve the BiSub in ethanol (99%) with salicylic acid, for the material BiNPs@AC-SA. SA is soluble in EtOH (mole fraction solubility: 0.143 at 25°C)[60] and, since it is a weak acid, it can dissociate forming the salicylate and a proton.[61] For BiNPs@AC-AcOH, a mixture of ethanol (99%) and acetic acid was employed. In Appendix E are reported more details and photos about the solubility test.

In Table 4 are shown all the materials BiNPs@AC-SA and BiNPs@AC-AcOH synthesized, the parameters changed and an identification code that will be used from now on is also reported.

Table 4: Samples list of BiNPs@AC-SA and BiNPs@AC-AcOH with identification code.

Name	Code	BiSub [g]	Solvent
BiNPs@AC-SA	MA010	0.5852	99%EtOH 1.8M SA
BiNPs@AC-AcOH	MA011	0.5853	13 mL 99%EtOH + 12 mL Acetic acid
	MA012	0.0585	

Due to the changes in the synthesis procedure, the BiSub@AC-400, the BiNPs@AC-SA and the BiNPs@AC-AcOH looks different during the steps. In Figure 20, 21 and 23 are shown images of how these materials appear during the synthesis process.
For the BiSub@AC-400 (Figure 20), the solution during the stirring and the powder after the drying step appear grey as they respectively consists of a dispersion and a mixture of BiSub (white) and AC (black). During pyrolysis, BiSub decomposes to form metallic bismuth (black) and bismuth oxide (yellow), resulting in a powder that is predominantly black.

For the BiNPs@AC-SA material (Figure 21), the solution appears black. Since the BiSub solution alone is nearly transparent (Appendix E), the addition of AC is responsible for the observed dark coloration. After drying, the sample appears heterogeneous, with distinct regions: a black portion attributed to AC, white needle-like crystals identified as SA, and pink hemispherical crystal structures. The pink phase is hypothesized to correspond to bismuth subsalicylate. While commercially available BiSub (Sigma-Aldrich) is typically white, its color can vary due to differences in layer stacking or the presence of

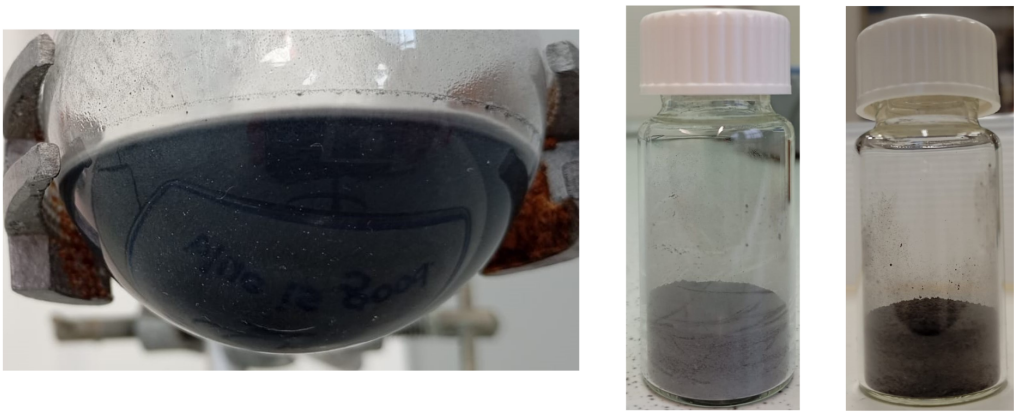

(a) (b) (c)

Figure 20: (a) Solution after the stirring overnight; (b) Powder after the drying in the oven; (c) Powder after the pyrolysis

(a) (b) (c) (d)

Figure 21: (a) Solution after the stirring overnight; (b) Material after the drying in the oven; (c) Powder after the grinding whit the opal mortar; (d) Pyrolized powder.

crystallographic defects, both of which are influenced by the crystallization conditions. Alternatively, the pink crystals may represent a different bismuth–salicylate complex, such as bismuth disalicylate, potentially formed due to the high concentration of salicylate in the solution.[62] Considering only the $Hsal^-$ that comes from the SA solubilization, the salicylate concentration in the solution reaches 1.8M. To confirm the identity of the pink compound, XRD analysis should be performed on the material prior to pyrolysis.
The presence of these pink regions suggest that not all of the BiSub was absorbed onto the AC surface. This may result from incomplete solubilization of BiSub (Appendix E) or the high salicylate concentration favoring the formation of complexes with Bi^{3+} ions, thereby impeding adsorption.
The high amount of SA added to the solution results in a light-grey powder after grinding, which turns black following pyrolysis. This color change is attributed to the volatilization of SA (boiling point, 211 °C at 20 mmHg) and the thermal degradation of BiSub. The final material is composed by crystals of metallic bismuth (rhombohedral and hexagonal) and an amorphous phase that remains difficult to identify (Figure 24); more details are discussed later in this chapter.
Evidence for SA volatilization is provided by the observation of needle-like crystals deposited at the inlet and outlet ends of the quartz tube during the pyrolysis(Figure 22). This phenomenon likely occurs because these regions are cooler than the central zone of the tube during heating. As a result, SA volatilizes from the quartz boat and subsequently condenses in the cooler sections of the tube. The pinkish coloration of these

needle-like crystals might suggests the presence of bismuth impurities, potentially corresponding to Bi-salicylate compounds. This observation aligns with the lower Bi%wt in MA010 measured by TGA analysis (Figure 31).

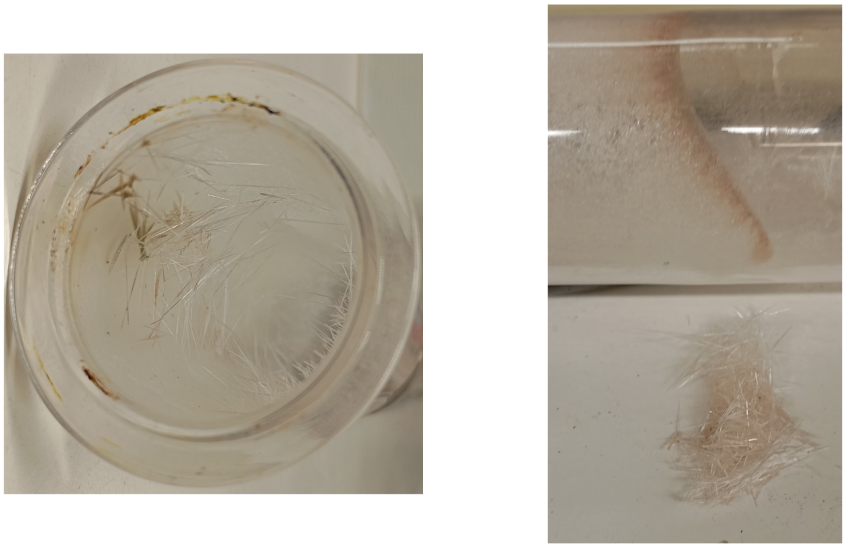

Figure 22: Needle-like crystals formed in the tube during the pyrolysis of MA010.

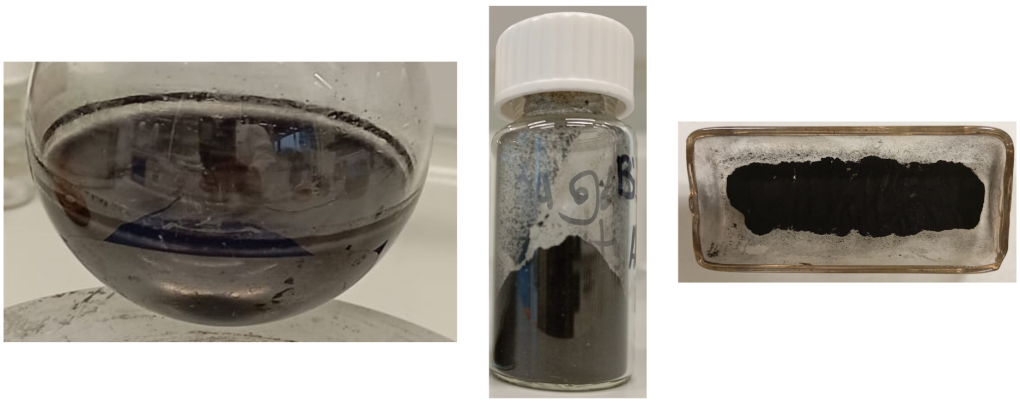

(a) (b) (c)

Figure 23: (a) Solution after the stirring overnight; (b) Material after the drying in the oven; (c) Pyrolized powder.

For the BiNPs@AC-AcOH material (Figure 23), both the solution and the dried powder appear predominantly black. This is likely due to the acidic environment created by the addition of acetic acid, which allows the solubilization of BiSub (Appendix E) and then evaporates during the drying process.
After the pyrolysis, the powder is still black because the BiSub is converted into metallic bismuth and Bi_2O_3 through thermal degradation and reduction under the pyrolytic conditions (Figure 24).

In Figure 24 are reported the XRD patterns of the materials MA010 and MA011, alongside that of MA004 to allow the comparison with BiSub@AC-400 materials.
The XRD pattern of material MA011 reveals the same crystalline phases previously identified in BiSub@AC-400 samples. In contrast, no crystalline Bi_2O_3 was detected in MA010

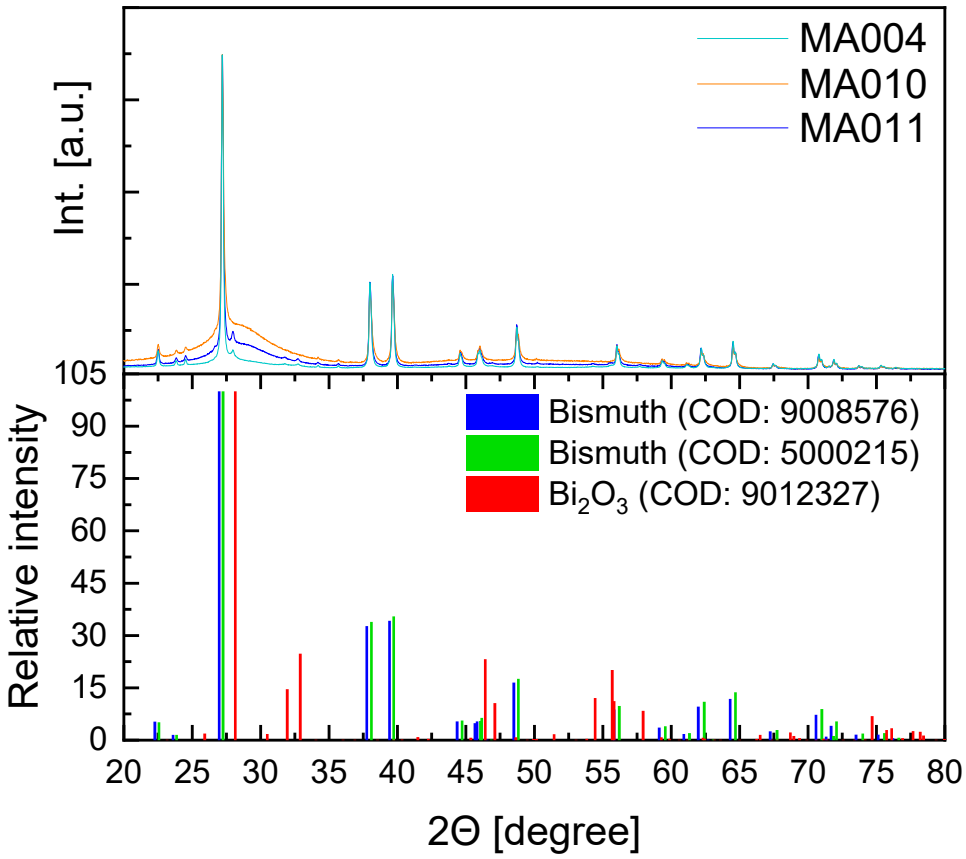

Figure 24: XRD patterns of the materials MA005, MA010 and MA011.

sample. Both diffractograms exhibit a broad hump in the 2θ range of 25–32°, indicative of an amorphous phase. However, the hump appears relatively more intense in MA010, suggesting a higher amorphous-to-crystalline bismuth ratio in this material. Two potential origins for this amorphous signal are proposed: (i) amorphous carbon, possibly arising from residue of BiSub and SA during pyrolysis, and (ii) amorphous Bi/Bi_2O_3.[63]
The appearance of a new amorphous carbon phase in MA010 and MA011, compared to BiSub@AC-400, may be attributed to improved interactions between the BiSub and the AC. Such interactions could thermally stabilize BiSub during pyrolysis, leading to a higher carbon residue. This interaction likely occurs between the delocalized electrons in the aromatic ring of BiSub and the π-electron system on the AC surface. Enhanced interaction in BiNPs@AC-SA is supported by its higher dispersion of Bi on the AC surface, both before and after pyrolysis (Figure 30), in comparison to BiSub@AC-400 (Figure 18). Since this improved interaction is likely due to the solubilization of BiSub in solution, a similar effect is expected for BiNPs@AC-AcOH. Moreover, MA010 exhibits a more pronounced amorphous hump than MA011, which may be attributed to residual SA remaining after pyrolysis. Given that SA also contains an aromatic ring, it could interact with the AC surface via $\pi-\pi$ interactions, thereby enhancing the thermal stability of the carbon phase and contributing to the observed amorphous signal. However, TGA analysis of MA011 indicates a Bi weight concentration comparable to BiSub@AC-400, suggesting that the overall carbon residue is not significantly higher. This aspect is discussed in more detail later in this chapter.
The formation of amorphous bismuth/bismuth oxide NPs may be attributed to their in-

teraction with the AC surface. This interaction can lead to anchoring the bismuth species onto the disordered substrate, thereby inhibiting crystal growth and promoting the stabilization of an amorphous structure.[64] TEM images of MA010 (Figure 25) support this interpretation: darker spots (some highlighted with a light green outline) are visible on the AC surface and may correspond to amorphous NPs (5–10 nm in size), as the absence of discernible reticular fringes might indicate. In contrast, larger NPs (>30 nm) are mainly black under the imaging conditions, making it difficult to confirm the presence or absence of lattice fringes; their crystallinity therefore cannot be definitively assessed.

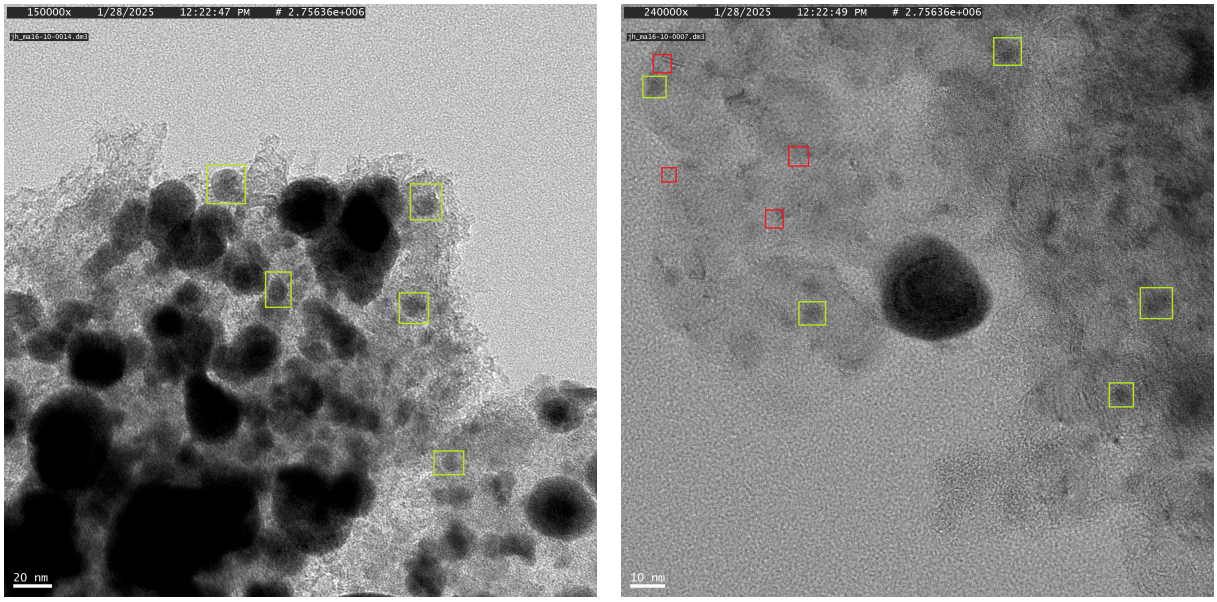

(a) TEM image of MA010 at 150000 x magnification.

(b) TEM image of MA010 at 240000 x magnification.

Figure 25: TEM images of MA010.

In the clearer regions of Figure 25b, small domains exhibiting lattice fringes with an interplanar spacing of approximately 0.33 nm are observable (some highlighted with a red outline). These features suggest the presence of localized crystalline regions, which may correspond to small crystalline domains within the AC matrix. However, they could also originate from partially crystallized Bi NPs, as no STEM-EDX analysis was performed at such high magnification to definitively confirm their composition.

The Scherrer equation was applied also for the patterns of MA010 and MA011, the crystallite size estimation is reported in Figure 26.

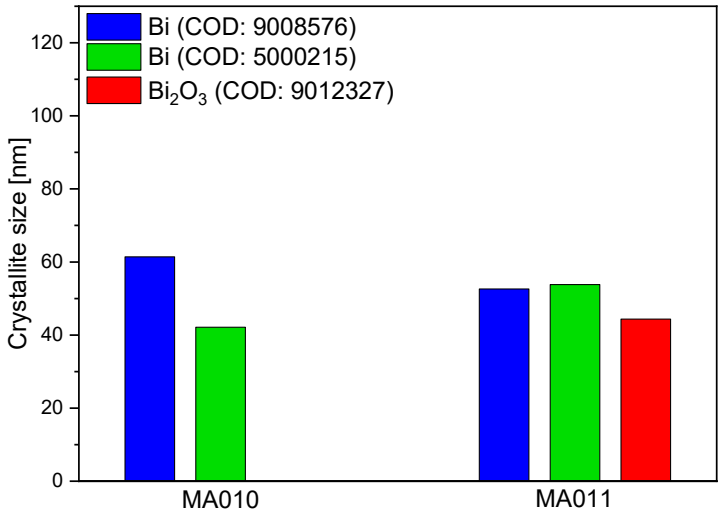

Figure 26: Estimation of crystallite size of the crystalline phases present in the materials MA010 and MA011.

The crystallite size estimation of MA010 and MA011 is around 50 nm and 50-100 nm range respectively. Since the Scherrer equation gives only an estimation of the crystallite size the SEM analysis (Figure 27) was performed on the materials to measure the NPs size.

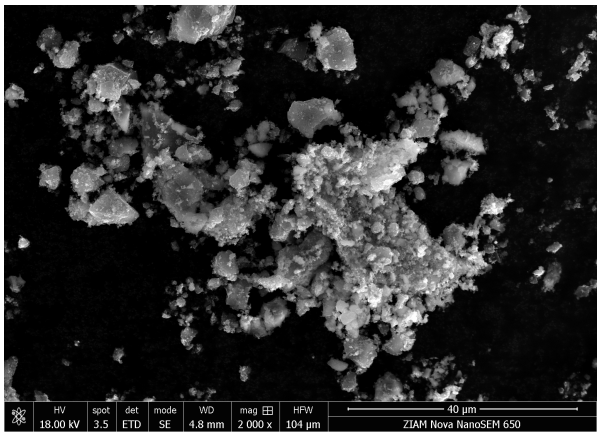

(a) Image of MA010 at 2000 x magnification.

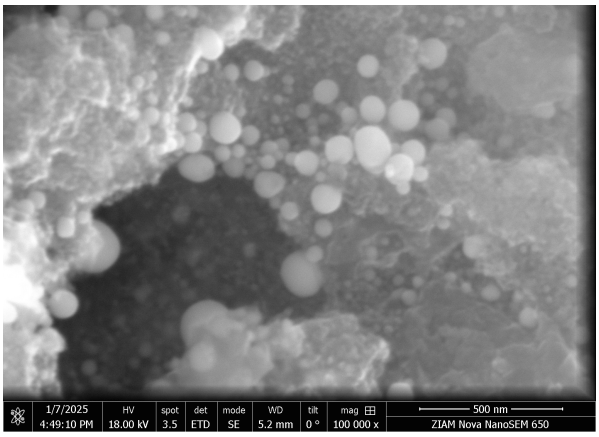

(b) Image of MA010 at 100000 x magnification.

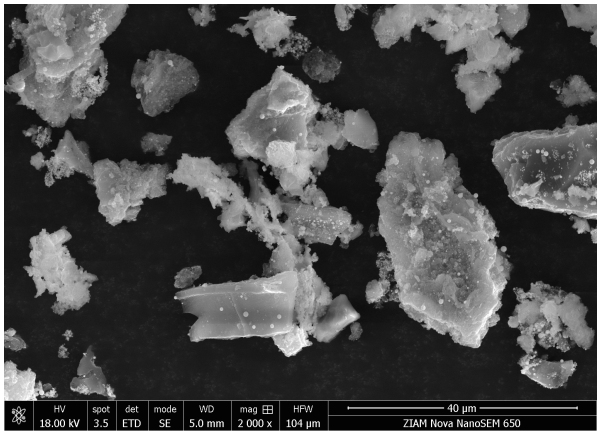

(c) Image of MA003 at 2000 x magnification.

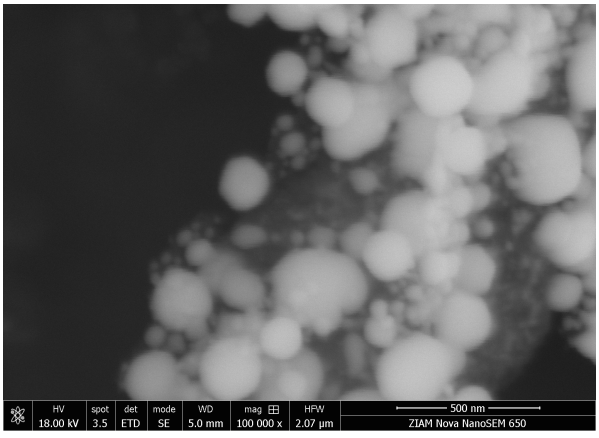

(d) Image of MA003 at 100000 x magnification.

Figure 27: SEM images at different magnification of MA010 and MA011.

Using the software ImageJ, the particles size range for MA010 was measured to be 20–250 nm, while for MA011 it ranged from 20–1000 nm. The significantly larger particles observed in MA011 compared to all other materials, including MA012 (Figure 33), are most likely attributable to a higher amount of undissolved BiSub in the solution, rather than to any detrimental effect of the AcOH. A detailed comparison between materials MA011 and MA012 is presented in subsubsection 3.1.4.

Low magnification SEM images (Figure 27a, 27c) reveal that the morphology of MA010 and MA011 is more homogeneous compared to BiSub@AC-400. The rod-like structures characteristic of BiSub@AC-400 are no longer visible. The AC support remains identifiable, and a greater number of small particles appear distributed across its surface.
The disappearance of these rod-like regions may be attributed to the improved solubility of BiSub achieved through the modified synthesis conditions. This hypothesis is supported by the observation that pure BiSub exhibits a similar rod-like crystal morphology, as shown in Figure 28.[59]

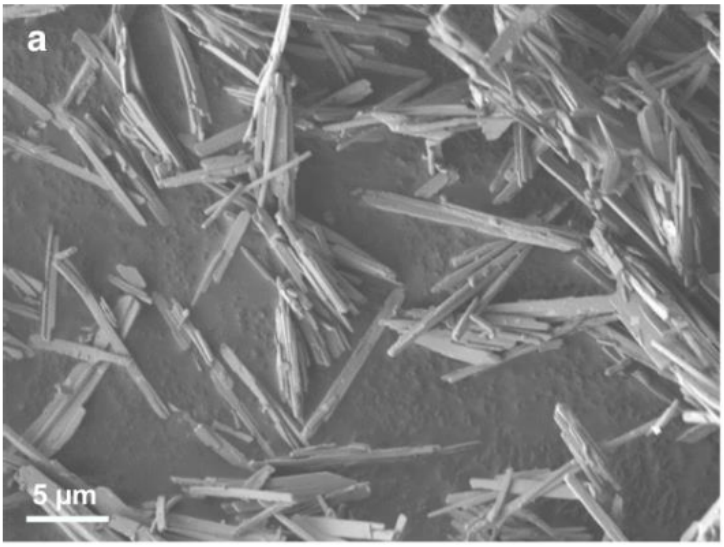

Figure 28: SEM images of BiSub purchased from Sigma-Aldrich.[59]

In the synthesis of BiSub@AC-400, the low solubility of BiSub may lead to the retention of its original crystal morphology throughout the stirring and drying steps. Although BiSub undergoes thermal degradation and reduction to metallic bismuth during pyrolysis, it may partially retain its initial structure due to incomplete decomposition. This interpretation is further supported by the elemental composition analysis of BiSub@AC-400 obtained through TGA (Figure 31 and Table 5), which reveals a carbon concentration slightly higher (64-65%) than the theoretical value (60%) calculated using Equation 6. This equation assumes complete decomposition of BiSub and the exclusive presence of metallic bismuth.
Figure 29 shows TEM images of MA004, highlighting both the rod-like structures and the NPs on the AC surface.

Furthermore, the material MA010 was analyzed by STEM-EDX both before and after the pyrolysis, the elemental distribution is reported in Figure 30. Figure 30d reveals that BiNPs@AC-SA is more homogeneous than BiSub@AC-400 also looking at the bismuth dispersion on the AC surface. The elemental distribution obtained by the STEM-EDX analysis before pyrolysis (Figure 30b) shows 22.3 %wt carbon, 70.4 %wt bismuth and 7.3

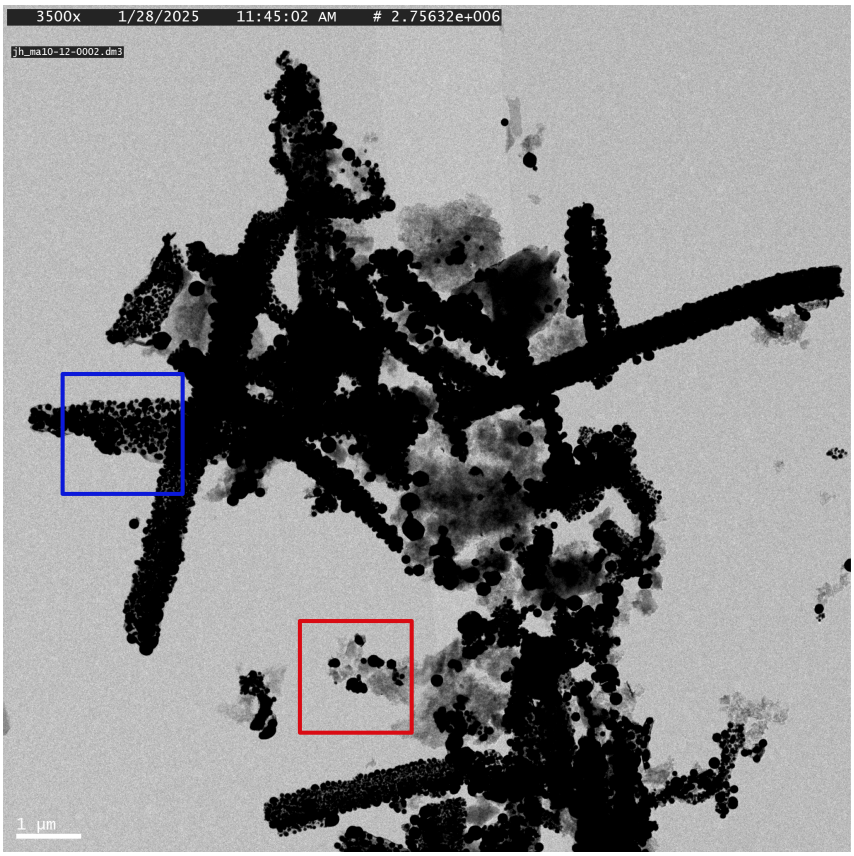

(a) Image of MA004 at 3500 x magnification.

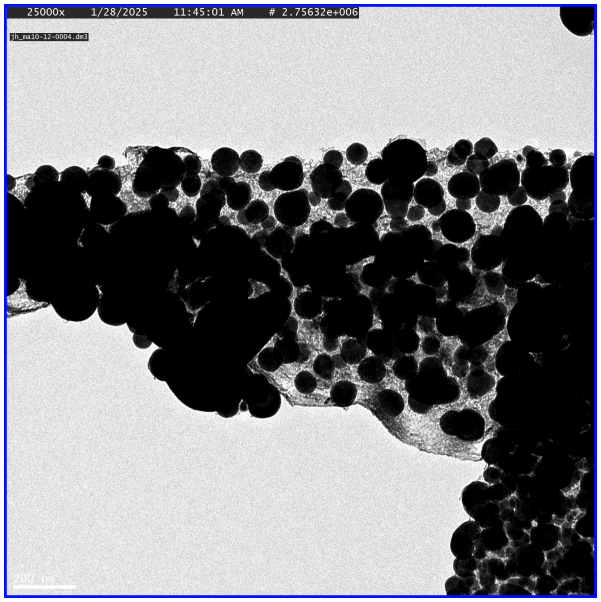

(b) Rod-like structure at 25000 x magnification.

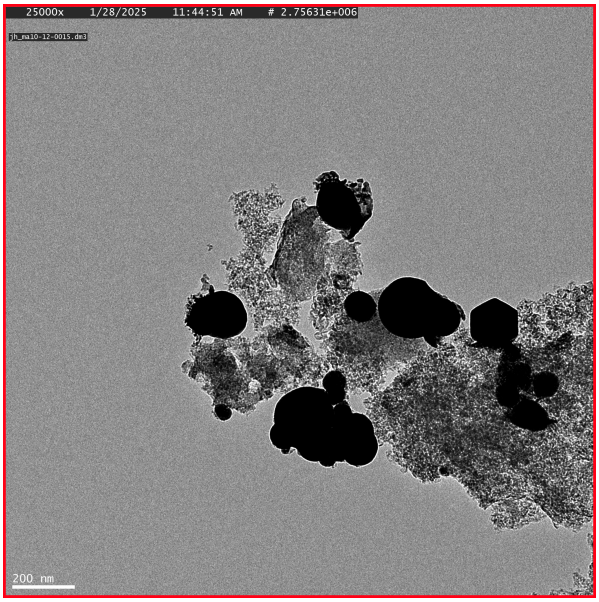

(c) AC with Bi NPs over the surface at 25000 x magnification.

Figure 29: TEM images of the MA004 material.

%wt oxygen. These values differ significantly from the expected composition of a physical mixture of 0.5852 g of BiSub and 0.509 g of AC, which, excluding hydrogen, should approximate be 59.5 wt% carbon, 31 wt% bismuth, and 9.5 wt% oxygen.
After pyrolysis, the elemental distribution determined by STEM-EDX (Figure 30d) is

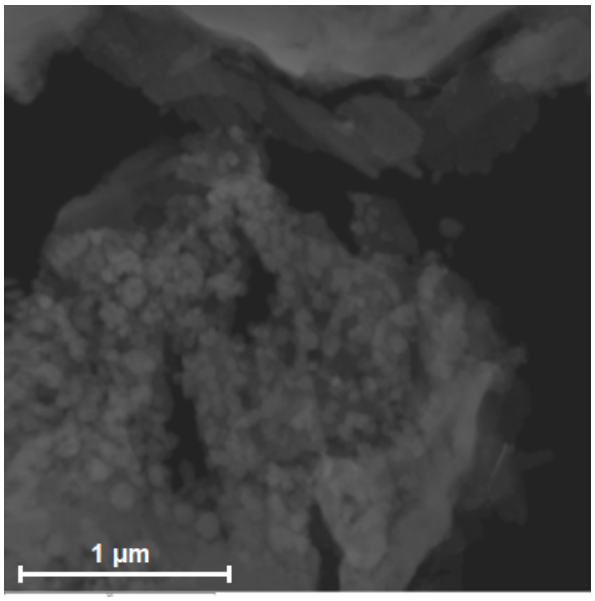

(a) TEM image of the area of analysis of BiNPs@AC-SA before the pyrolysis.

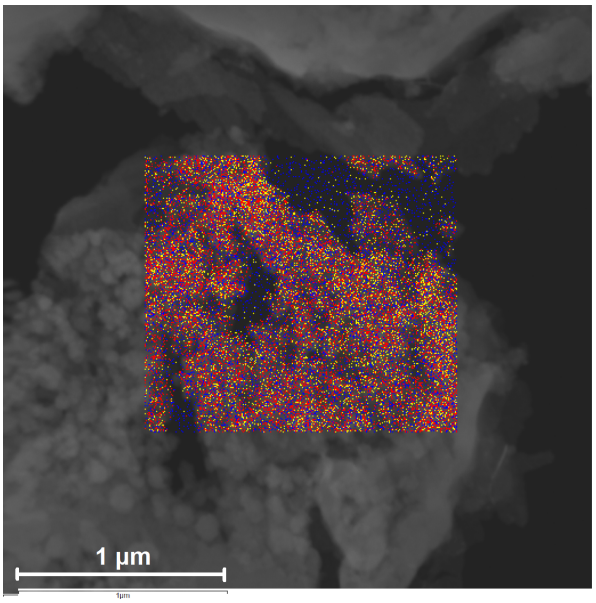

(b) Image of the element distribution of BiNPs@AC-SA before the pyrolysis.

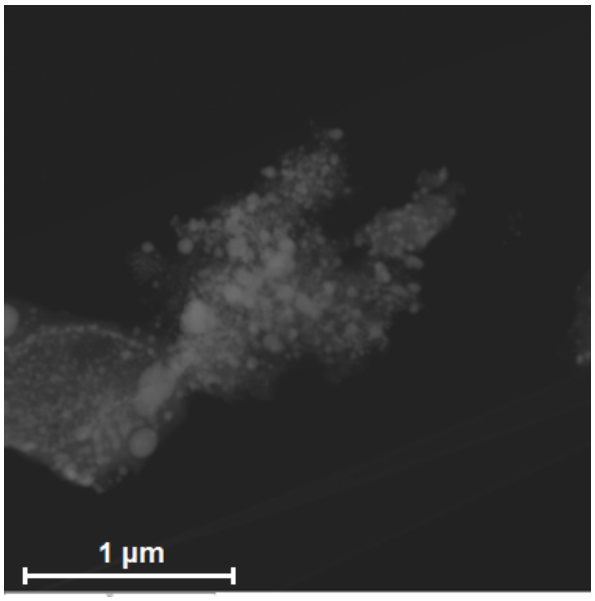

(c) TEM image of the area of analysis of BiNPs@AC-SA after the pyrolysis.

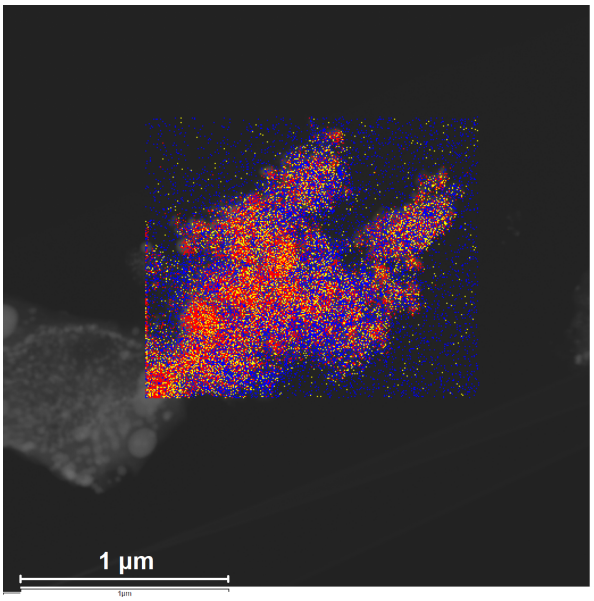

(d) Image of the element distribution of BiNPs@AC-SA after the pyrolysis.

Figure 30: STEM-EDX images of BiNPs@AC-SA.

41.3 wt% carbon, 53.1 wt% bismuth, and 5.6 wt% oxygen. According to the theoretical calculation in Equation 6, assuming complete decomposition of BiSub and the exclusive presence of metallic bismuth, the expected composition of MA010 should be approximately 60 wt% carbon and 40 wt% bismuth.
These differences in both pre- and post-pyrolysis measurements (Figure 30b, 30d) are probably due to limitations of the EDX technique. Heavier elements such as bismuth tend to emit more intense and higher-energy characteristic X-rays, potentially leading to an overestimation of their concentration. Additionally, because the EDX analysis is performed on a micrometric area, the results may not be representative of the macroscopic composition of the sample. However, these results may suggest a non-homogeneous dis-

tribution of the BiSub and Bi on the AC surface.

3.1.3 Thermogravimetric analysis

To obtain a macroscopic bismuth %wt data all the materials and the AC alone were tested by a TGA analysis in air. In Figure 31 the TGA result are shown as weight loss % against temperature of the sample.

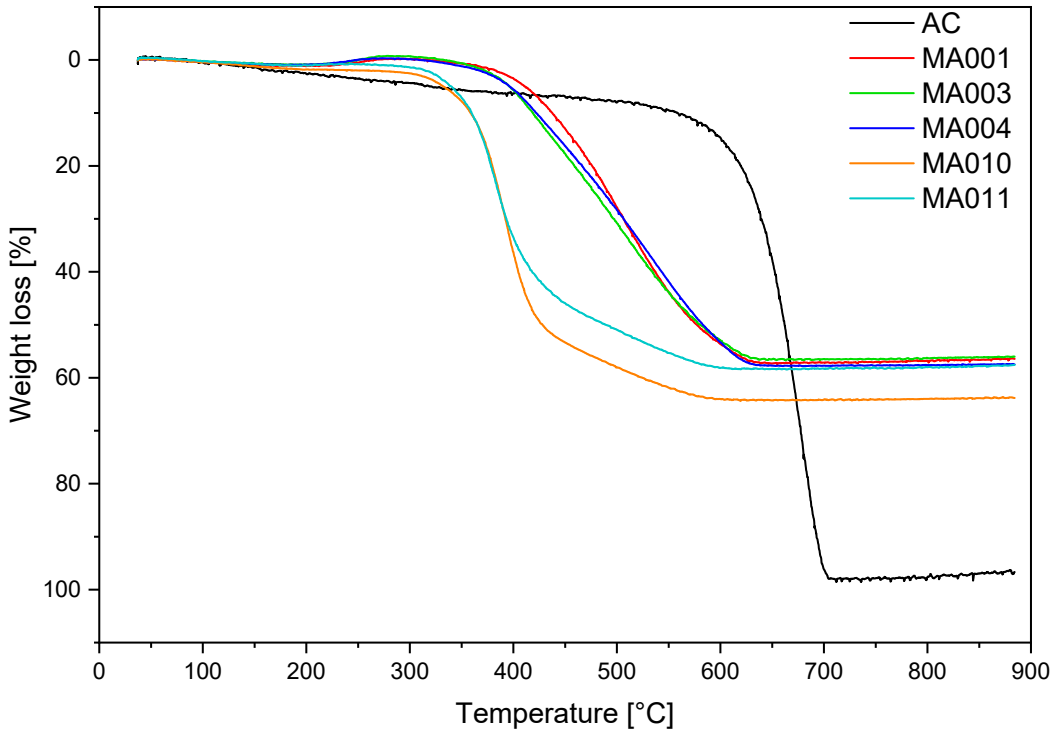

Figure 31: TGA analysis of BiSub@AC-400, BiNPs@AC-SA and BiNPs@AC-AcOH materials.

The main feature of the TGA curves (Figure 31), that is common to all the materials, is that the presence of Bi can catalyze the degradation of the AC reducing its T_{onset}. [2].

Using the Equation 5 the bismuth % wt was measured, Table 5 the results for all the materials are reported:

Table 5: Bismuth content in the materials MA001-011 measured by TGA analysis in air.

Material	Total weight loss %	Bi_2O_3% wt	Bi%wt
MA001	56	40	36
MA003	56	41	36
MA004	57	39	35
MA010	64	33	30
MA011	57	39	35

For the BiSub@AC-400 materials, it is interesting to observe that they exhibit similar thermal behavior (Figure 31). The onset temperatures (T_{onset}) for MA001, MA003 and

MA004 are 390 °C, 386 °C and 389 °C, respectively, while the final decomposition temperatures are 628 °C, 625 °C, and 625 °C.
The TGA curves for these materials show a single degradation step, but the DTG curves (Appendix F) reveal three overlapping peaks, suggesting a multi-step thermal degradation process. Using the DTG curves, the maximum degradation temperatures (T_{max}) were identified: 507 °C for MA001, 508 °C for MA003, and 535 °C for MA004. Interestingly, MA004 exhibits a higher T_{max} compared to the other BiSub@AC-400 materials, suggesting that bismuth in MA004 may be slightly less efficient in catalyzing the degradation process. However, due to the overlapping peaks it is challenging to understand the specific events during each degradation step and the cause of the T_{max} differences. To study in more details the degradation process, additional TGA analysis with a reduced heating rate would be beneficial.
At lower temperatures, the DTG curves (Appendix F) display a negative peak, indicating a weight gain likely due to bismuth oxidation. The peak temperature for MA001, MA003 and MA004 is 250 °C, 251 °C and 238 °C, respectively, aligning with literature values.[65] The lower oxidation peak temperature for MA004 may be attributed to smaller crystallites (Figure 15), as smaller crystallites have increased grain boundaries, surface defects that facilitate faster oxygen diffusion due to their imperfect atomic arrangement.[66]
Elemental composition analysis (Table 5) shows that the bismuth content in MA001, MA003, and MA004 is approximately 35–36%, which is lower than the theoretical value obtained using Equation 6 (40%wt Bi and 60%wt C). This discrepancy suggests incomplete BiSub degradation, consistent with the rod-like structures observed in SEM images as previously discussed (Figure 29b). However, this difference might be caused by an underestimation of the Bi content due to incomplete bismuth oxidation during TGA analysis. A more precise bismuth quantification could be achieved using elemental analysis methods such as ICP-OES.[2]

For MA010 and MA011, the thermal behavior differs slightly. The TGA curves (Figure 31) display two distinct degradation steps, with the DTG curves (Appendix F) showing a pronounced peak in the first step and ambiguity in the second, possibly indicating overlapping peaks.
The first degradation step occurs between 316 °C and 426 °C (weight loss % of 49) for MA010 and between 321 °C and 421 °C (weight loss % of 42) for MA011, with T_{max} values of 394 °C and 384 °C, respectively. These lower onset temperatures and higher degradation rates suggest enhanced catalytic activity and efficiency of bismuth in these materials compared to BiSub@AC-400. This enhanced activity may result from: (i) improved bismuth distribution on the AC surface (Figure 18b, 18d, 30d); or (ii) the presence of amorphous bismuth, which is known to exhibit higher reactivity than its crystalline counterpart. In this second scenario, the initial degradation step likely corresponds to the amorphous bismuth phase, followed by degradation of the crystalline phase. The presence of amorphous bismuth is supported by both XRD (Figure 24) and TEM analysis (Figure 25), as previously discussed. TGA gives further evidence, which includes:

- Two degradation steps: the second step, attributed to crystalline bismuth, exhibits a lower degradation rate and occurs between 426 °C and 583 °C for MA010 and 421 °C and 581 °C for MA011. Notably, the T_{onset} of the second step is comparable with the crystallization temperature of bismuth NPs considering an average radius of about 20 nm.[67] The reported crystallization temperature is approximately 390 °C so the measured T_{onset} are slightly higher, but this difference might be due to

the fast temperature ramp (10 °C/min).

- Weight loss percentages: for MA010, the first step accounts for 79% of the total weight loss, while it accounts for 74% in MA011. This proportional difference suggests a higher amorphous-to-crystalline ratio in MA010, consistent with the more pronounced hump in its XRD pattern (Figure 24).
- Reduction or disappearance of the negative DTG peak (Appendix F): the amorphous bismuth phase is more reactive compare to the crystalline one, so it get oxidazed at lower temperature. In MA011, the oxidation peak is less intense, while in MA010, it is absent, aligning with the amorphous-to-crystalline ratio discussed in the previous point.
- Measured Bi content: the bismuth weight concentration in MA011 matches that of BiSub@AC-400 materials (Table 5), suggesting that the XRD hump (Figure 24) is likely related to the presence of amorphous Bi/Bi_2O_3 instead of carbon. However, in MA010 the carbon content is higher and the hump is more pronounced compared to MA011, so this might suggest contributions from both Bi/Bi_2O_3 and carbon residues.

3.1.4 BiNPs@AC-AcOH: effect of BiSub:AC ratio

The effect of reducing the BiSub:AC ratio was investigated using the BiNPs@AC-AcOH synthesis method. In MA011, BiSub was not completely solubilized (Appendix E); thus, MA012 was synthetized using only 10%wt of the original amount of Bi precursor.

In Figure 32 the XRD pattern of MA012 is shown.
Comparison of the XRD patterns of MA012 and MA011 reveals the presence of the graphite peak around 26°–27° 2θ, more intense Bi_2O_3 peaks, along with hump regions before the main peak and between 40°–47° 2θ. These signals are attributed to the AC support, which becomes detectable in MA012 due to its lower bismuth loading. In fact, the relative intensity of the peak or the hump compared to the highest peak of the diffrattogram can give information about the concentration of the different phases.
The characteristic hump in the 25-32° 2θ range remains visible and is slightly more intense compared to MA011. Additionally, the peaks in MA012 are broader than those in MA011, indicating smaller estimated crystallite size of 30–40 nm for MA012 compared to 50–100 nm for MA011.

Figure 33 shows the SEM images of MA012.
In MA012, the NPs size distribution is narrower than in MA011, ranging from 20–250 nm compared to 20–1000 nm, respectively. Notably, MA012 exhibits a bimodal size distribution: larger NPs in the 100–250 nm range (Figure 33a) and smaller white spots approximately 20 nm in size (Figure 33b).

In Figure 34 both the TGA curve of MA011 and MA012 are reported.
Reducing the BiSub amount by 90% resulted in an increase in both T_{onset} and T_{max} (obtained by the DTG curve shown in Appendix F), from 321°C to 448°C and from 384°C to 506°C, respectively. This increase is likely due to the reduced bismuth concentration in MA012, as bismuth is supposed to catalyze the thermal degradation of AC.[2]
The TGA curve of MA012 reveals three distinct degradation steps with varying rates:

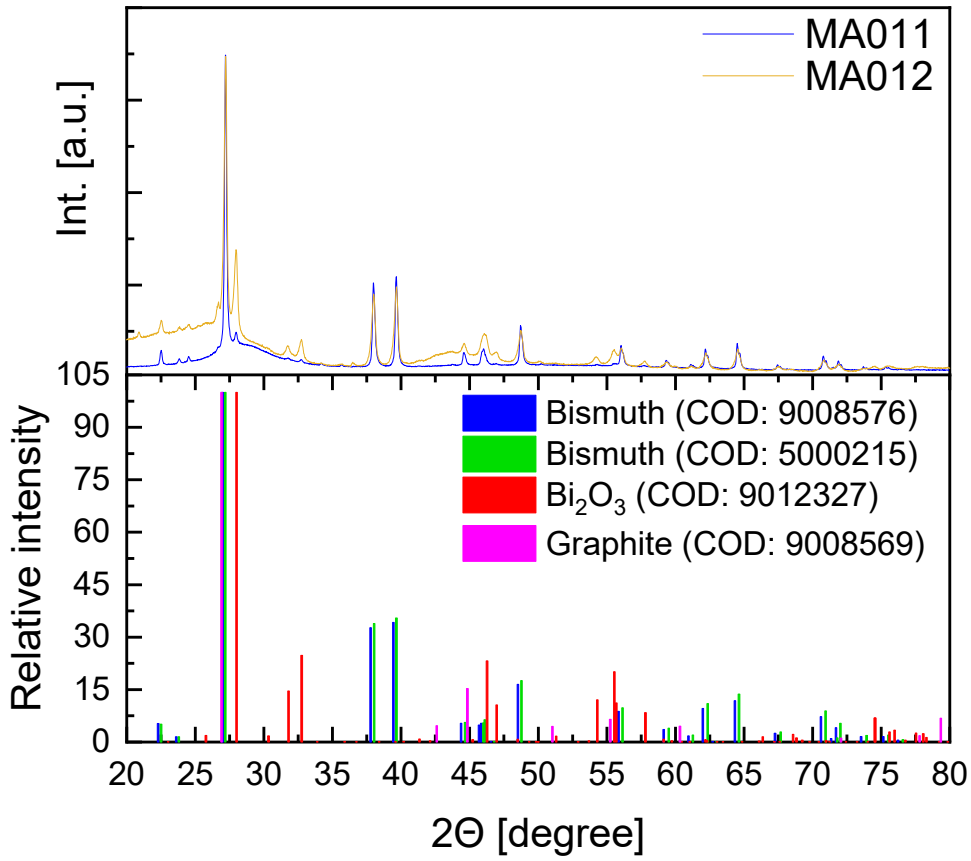

Figure 32: XRD patterns of MA011 and MA012.

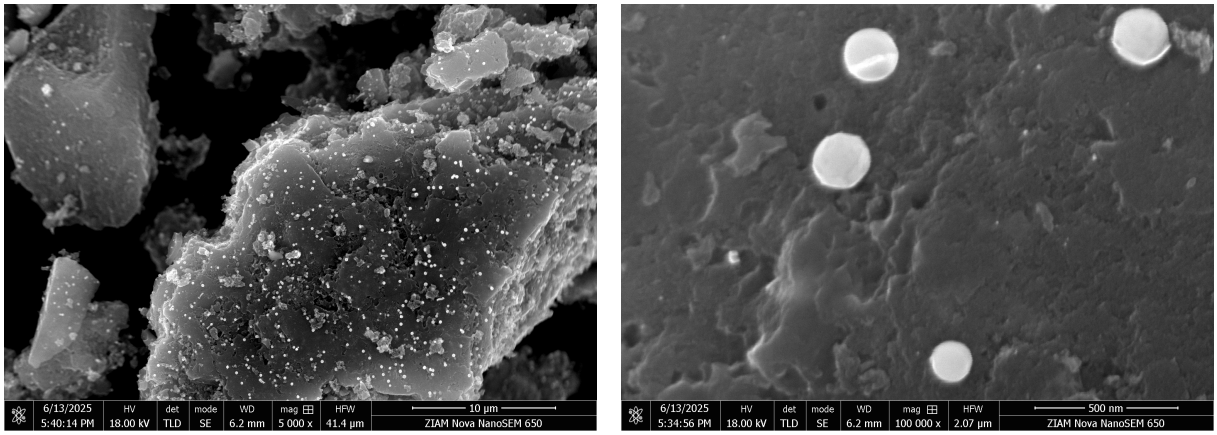

(a) SEM image of MA012 at 5000 x magnification.

(b) SEM image of MA012 at 100000 x magnification.

Figure 33: SEM images of the MA012 material.

- 448-497 °C, 21% weight loss.
- 497-523 °C, 53% weight loss.
- 523-590 °C, 11% weight loss.

In the TGA curve of MA011 (Figure 31) only two of these steps are visible. However, the DTG curve of MA011 suggests the presence of an initial degradation step preceding

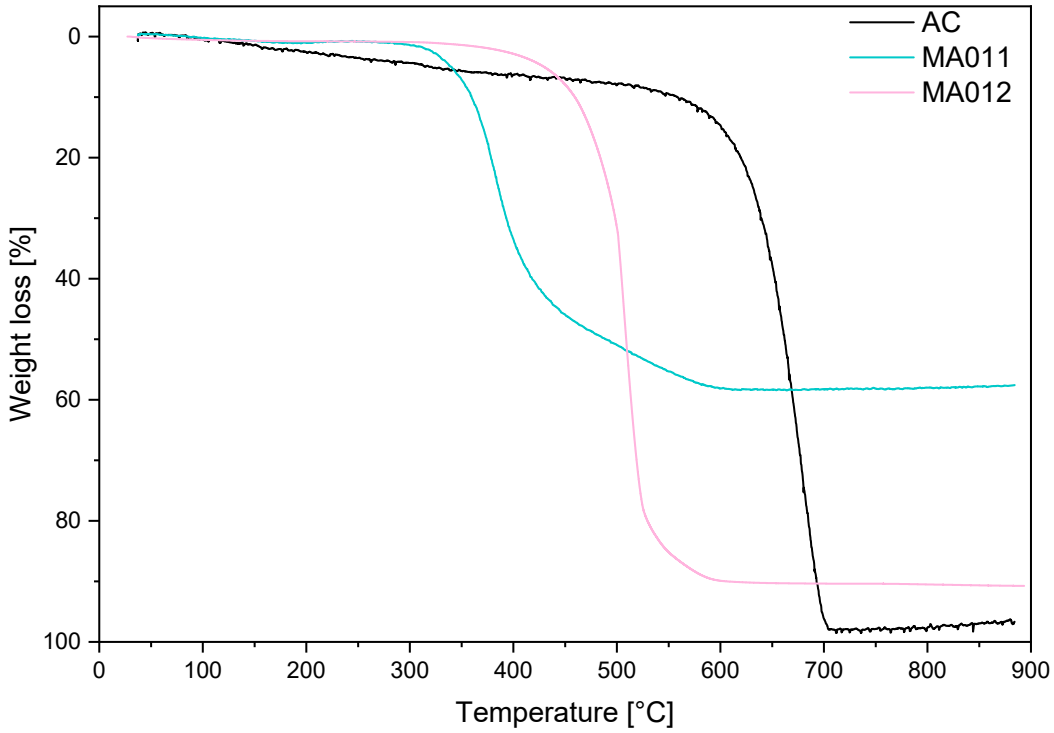

Figure 34: TGA analysis of BiNPs@AC-AcOH materials.

the main one. In MA012, the slower overall degradation process, likely due to the lower bismuth concentration, allows the first step to be more distinguishable in the TGA curve. Using the Equation 5, the bismuth content in MA012 was measured to be 5%wt, which is slightly lower than the theoretical value of 6%wt measured by Equation 6, assuming complete degradation of BiSub to metallic bismuth. The discrepancy may be attributed to the same factors discussed for the other materials, such as incomplete degradation of BiSub or incomplete bismuth oxidation during TGA analysis.

3.2 Electrochemical characterization

All the materials were tested three times to evaluate the reproducibility of the electrochemical test, in this chapter only the mean curves with the error are reported. In Appendix G are shown all the curves of each material and the calculation of the Faradaic efficiency toward formate ($FE_{formate}$).
The GC electrode and the bare AC were tested by chronoamperometry, Appendix C shows all the results. They both demonstrate increasing current density over time, with average value of -6.5 and -13.8 mA cm^{-2} respectively. However, no liquid product where detectable by HPLC analysis of the catholyte.

To make comparable all the tests the same condition were used and the uncompensated resistance (R_u) was maintained in the 3-4 Ohm range. Appendix G also reports the (R_u measured before each CA test.

3.2.1 BiSub@AC-400 materials

The materials MA001, MA003 and MA004 were tested electrochemically, Figure 35 report the CA mean curves and the error bands of each material. 50 μL of ink was dropcasted onto the GC electrode (1.69 cm^2) resulting in a catalyst loading of 0.296 mg cm^{-2}. All the samples were tested with the same catalyst loading to ensure a fair comparison of their intrinsic activity.

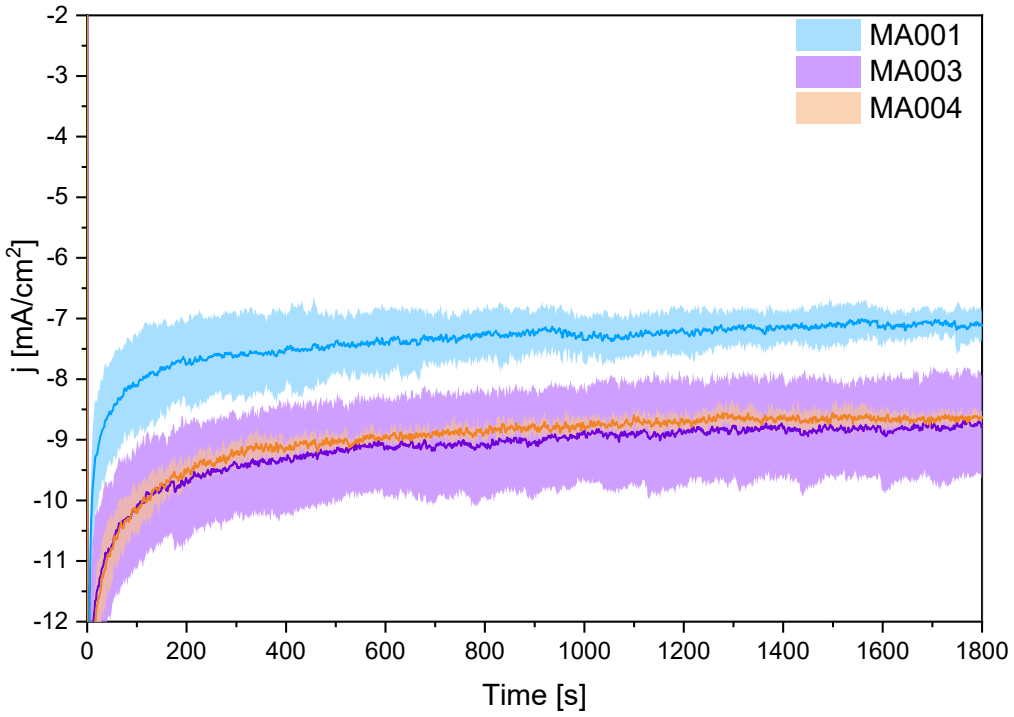

Figure 35: Chronoamperometry test, with mean curve and error, of MA001, MA003 and MA004.

The $FE_{formate}$ was also measured using the Equation 12, in Table 6 is reported the average value and the standard deviation for each material.

Table 6: Average current densities and Faradaic efficiencies toward formate of MA001, MA003 and MA004.

Material	Average j [mA cm^{-2}]	$FE_{formate}$ %
MA001	-7.6	86 ± 1%
MA003	-8.8	84 ± 4%
MA004	-8.7	83 ± 5%

All BiSub@AC-400 materials exhibited similar $FE_{formate}$, but the average current density of MA001 was lower compared to the materials synthesized with the new batch of BiSub. Additionally, MA001 also shows reduced electrocatalytic activity normalized by bismuth mass (Equation 8) compared to MA003 and MA004, with corresponding values of -0.36, -0.41 and -0.41 mA cm^{-2} mg^{-1}, respectively.
Several factors might contribute to this difference, two possible interpretation include: (i) partial degradation of the older BiSub, although this was not confirmed by experimental characterization (Appendix A), or (ii) variations in the fraction of rhombohedral and

hexagonal bismuth phases in the catalysts.
With regard to the second hypothesis, both rhombohedral and hexagonal bismuth belong to the same space group ($\overline{R}3m$), but their unit cells differ in size and shape. These structural differences influence which crystal facets are predominantly exposed, a critical factor for catalytic behavior. Specifically, the atoms arrangement of each facet impacts surface energy and the density of active sites. Atoms on crystal surfaces are non completely coordinated, leaving unsaturated orbitals known as dangling bonds, which contribute to the surface energy.[68] A greater density of dangling bonds correlates with higher surface energy, that refers the total excess energy possessed by the atoms on the surface compared to the ones in the bulk material.[69] In catalyst, dangling bonds serve as adsorption sites for reactant molecules, reducing the binding energy and enhancing the catalytic performance.[68]
Crystal facets are conventionally denoted by Miller indices (hkl).[66] These planes are often classified into: (i) low-index-facets, where h, k and l are 0 or 1, and (ii) high-index-facets, where at least one of the indices is equal to or greater than 2.[70] High-index facets tipically exhibit more surface defects, such as kinks, edges and steps, than lower-index planes. These defects serve as highly active catalytic sites thanks to increased density of dangling bonds and higher surface energy.[71]
The beneficial role of high-index facets in catalysis has been extensively studied for noble metals (primarily Pt, Pd and Au)[72] but only a limited number of Bi-based catalysts have been investigated (Bi dendrites[73], $BiVO_4$[71]).
As anticipated, rhombohedrical and hexagonal metallic bismuth primarily expose different facets. Using the DIFFRAC.EVA software and its crystallographic databases, the major XRD peaks and their corresponding facets were identified. These are summarized in Table 7.

Table 7: Relative intensities (normalized to 999), 2θ angles and crystal facets corresponding to the five most intense XRD peaks of rhombohedral (COD: 9008576) and hexagonal (COD: 5000215) bismuth phases.

Material	**Relative intensity**	2θ **angle [degrees]**	**Facet (hkl)**
Rhombohedral Bi	999	27.163	(110)
	390	37.954	(211)
	387	39.616	$(01\overline{1})$
	212	48.696	(200)
	187	64.508	$(21\overline{1})$
Hexagonal Bi	999	27.246	(012)
	393	39.719	(110)
	372	38.092	(104)
	211	48.834	(202)
	186	64.695	(122)

Notably, the hexagonal phase tends to expose a higher proportion of high-index facets (e.g., (012), (104)) compared to the rhombohedral phase. Therefore, it is plausible that a greater fraction of hexagonal bismuth in the electrocatalyst would enhance its catalytic activity due to the increased availability of highly active surface sites.

To assess the relative abundance of rhombohedral and hexagonal bismuth phases the peak area ratios were calculated, this is not a quantitative analysis but it provide insight into the relative concentrations of these phases. The peaks at approximately 27° 2θ and

the peaks between 64°–65° 2θ were analyzed (Table 7). While the first set of peaks is more intense, their overlap makes accurate convolution more challenging. The measured rhombohedral-to-hexagonal peak area ratios are as follows:

- MA001: 4.1 (27° 2θ) and 2.6 (64°-65° 2θ).
- MA002: 4.4 and 2.5.
- MA003: 3.3 and 2.0.
- MA004: 2.9 and 2.1.

The higher rhombohedral-to-hexagonal peak area ratios observed for MA001 and MA002 suggest a greater presence of rhombohedral Bi in these samples compared to the other materials. This variation in phase composition may be attributed to differing impurity profiles in the BiSub batches, which could influence the preferential growth of specific crystal facets.[74] In conclusion, the lower catalytic activity of MA001 can be attributed to the lower fraction of hexagonal bismuth, the crystalline phase that tends to expose a higher proportion of high-index facets.

Comparison with BiSub@AC-400

It is important to note that the results in Figure 35 are not directly comparable to the findings reported by Miola et al.[2] due to differences in catalyst loading. Material MA009 was retested with the loading of 0.385 mg cm^{-2} to enable a meaningful comparison. Increasing the catalyst loading, the average current density changed from -8.7 mA/cm^{-2} to -8.8 mA/cm^{-2}, and the average $FE_{formate}$ improved from 83 ± 5% to 88 ± 3% (Appendix G). The increase in Faradaic efficiency might be attributed to better coverage of the GC electrode. In fact, testing the GC electrode no production of formate was observed (Appendix D).
In the paper by Miola et al., testing at the same potential (-1.07 V vs. RHE) yielded nearly complete selectivity ($FE_{formate} > 99\%$) and a current density of -6.2 mA/cm^2. However, the reported Faradaic efficiency showed an error bar exceeding 100%, indicating possible analytical or systematic errors in the quantification method.
However, differences in the electrocatalyst performances were expected because of the physico-chemical properties dissimilarity of the materials.

The variations in the error bar width in the CA measurements of the different materials (Figure 35) could arise from human error during the drop-casting step in electrode preparation and to inherent variability of the cell configuration (Appendix D).

3.2.2 BiNPs@AC-SA and BiNPs@AC-AcOH materials

The materials MA010 and MA011 were tested electrochemically, Figure 36 presents the mean CA curves for both materials along with the error bands. The catalyst loading was maintained at 0.296 mg cm^{-2} for both samples to ensure a fair comparison with MA001, MA003 and MA004.
The $FE_{formate}$ of materials MA010 and MA011 is 75 ± 6% and 82 ± 3%, respectively. MA010 exhibits a lower current density and Faradaic efficiency compared to MA011, which is likely attributable to its lower bismuth content, as shown in Figure 31. However, despite a comparable bismuth content, MA011 exhibits lower current density than MA003 and MA004 (Table 5).

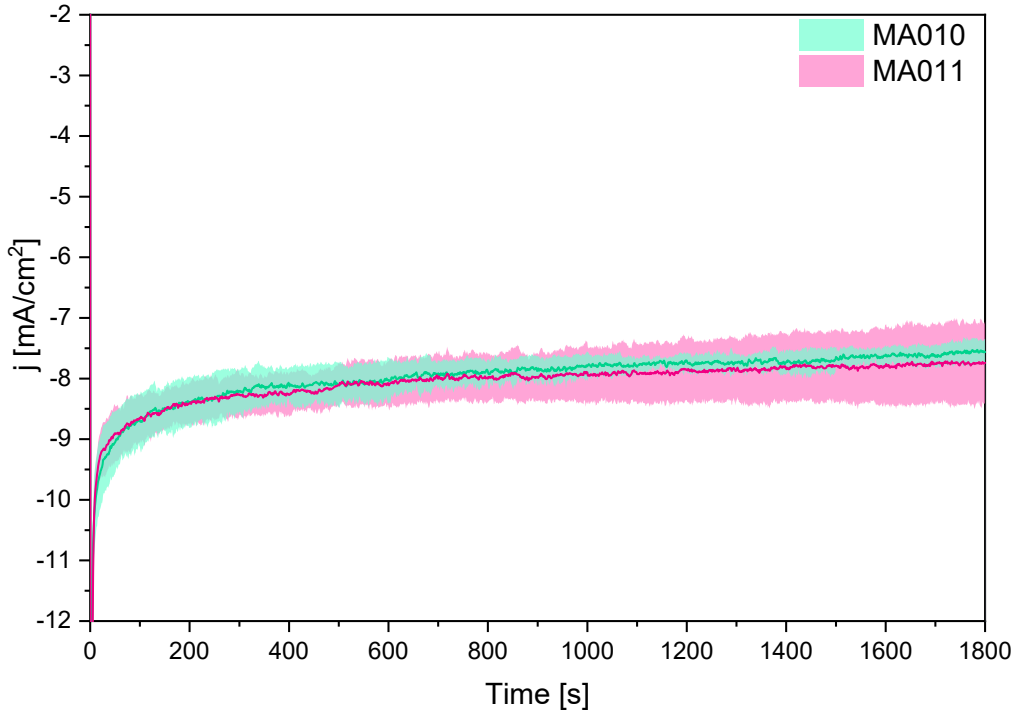

Figure 36: Chronoamperometry test, with mean curve and error (mean curve±standard deviation), of MA010 and MA011.

This discrepancy may be explained by two main hypotheses:

- Presence of amorphous Bi: previous studies have demonstrated, through both experimental analysis and DFT calculations, that a heterophase mixture of amorphous and crystalline bismuth can enhance the electrocatalytic performance in ECO_2RR.[75], [76] However, pure amorphous bismuth exhibits inferior activity compared to both crystalline and heterophase configurations.
  XRD analysis of MA010 and MA011 suggests the presence of both crystalline and amorphous bismuth phases (Figure 24), as previously discussed in this chapter. However, by TEM imaging it is difficult to affirm or deny the presence of a heterophase structure (Figure 25).

- Wettability changes: wettability plays a crucial role in electrocatalysis by influencing the surface area of the catalyst in contact with the electrolyte. According to the literature, nanostructured bismuth exhibits a lower water contact angle (about 80°) compared to AC, which has a contact angle of approximately 140°.[77], [78] These values, however, are highly dependent on surface roughness at both the micro and macro scale, and thus should be interpreted qualitatively. This hypothesis assume that the AC is hydrophobic and the bismuth NPs are hydrophilic.
  In the BiSub@AC-400 material, the majority of bismuth NPs are not supported directly on the AC substrate, implying that they are more likely to be fully exposed to the electrolyte. In contrast, in BiNPs@AC-SA and BiNPs@AC-AcOH, bismuth is more uniformly distributed across the AC surface. This creates regions with variable wettability based on the local surface area fractions of bismuth and AC. The Cassie-Baxter equation is commonly used to estimate the contact angle of such

heterogeneous surfaces, for a biphasic system:

$$cos\theta = \phi_1 \cdot cos\theta_1 + \phi_2 \cdot cos\theta_2$$

Where: θ is the effective contact angle, ϕ_1 and ϕ_2 are the surface area fractions of the two phases and θ_1 and θ_2 are their respective contact angles.
It is therefore plausible that regions with insufficient bismuth coverage remain poorly wetted by the electrolyte. This limited wettability may hinder the access of CO_2 molecules to the catalytic sites, thereby reducing, or even entirely suppressing, local electrochemical activity and ultimately compromising the overall catalytic performance of the material.

Since the bismuth content in MA010 and MA011 is different (Table 5), the electrocatalytic activity normalized by bismuth mass was calculated to be -0.39 mA/cm^2·mg for MA010 and -0.36 mA/cm^2·mg for MA011. This difference might be due to the rhombohedral-to-hexagonal peak area ratio of the two materials, as already discussed for BiSub@AC-400 materials. The measured values are:

- MA010: 0.8 (27° 2θ) and 1.0 (64°-65° 2θ).
- MA011: 2.6 and 1.3.

Compared to the BiSub@AC-400 materials, MA010 and MA011 exhibit a larger disparity in the rhombohedral-to-hexagonal peak area ratio, but a smaller variation in bismuth mass–normalized electrocatalytic activity. This behavior may be attributed to the higher fraction of amorphous phase present in MA010 relative to MA011 (Figure 24), which could negatively affect the material's catalytic performance. As a result, the potential benefits associated with the higher proportion of the hexagonal phase may be mitigated. Furthermore, the presence of amorphous bismuth phase implies a lower amount of crystalline material, thereby reducing the influence of variations in the rhombohedral-to-hexagonal ratio.

3.2.3 BiNPs@AC-AcOH: effect of BiSub:AC ratio

In Figure 37 are reported the CA mean curves and the error of MA011 and MA012.
Material MA012 exhibited an average current density of -4.1 mA/cm^2 with a $FE_{formate}$ of 70 ± 3%. In contrast, MA011 achieved both higher current density -7.8 mA/cm^2 and Faradaic efficiency 82 ± 3%.
Using the TGA in air the bismuth weight concentration in MA012 and MA011 was measured to be 5% and 35% respectively (Figure 34). Based on these values, the electrocatalytic activity normalized by bismuth mass was calculated to be -1.07 mA/cm^2·mg for MA012 and –0.36 mA/cm^2·mg for MA011. These results suggest that the bismuth in MA012 is more catalytically active on a per-mass basis, potentially due to the smaller size of its NPs (Figure 27, 33) and the greater fraction of the hexagonal bismuth phase. In fact, both materials contain comparable amounts of amorphous phase, as shown in Figure 32, but the rhombohedral-to-hexagonal peak area ratios for MA012 are significantly lower than those for MA011. Specifically, the ratios for MA012 are 0.2 (27° 2θ) and 0.1 (64°-65° 2θ), compared to 2.6 and 1.3, respectively, for MA011.
Regarding Faradaic efficiency, its reduction in MA012 may be attributed to a incomplete coverage of the AC surface. This hypothesis is supported by multiple CA measurements, shown in Figure 38.

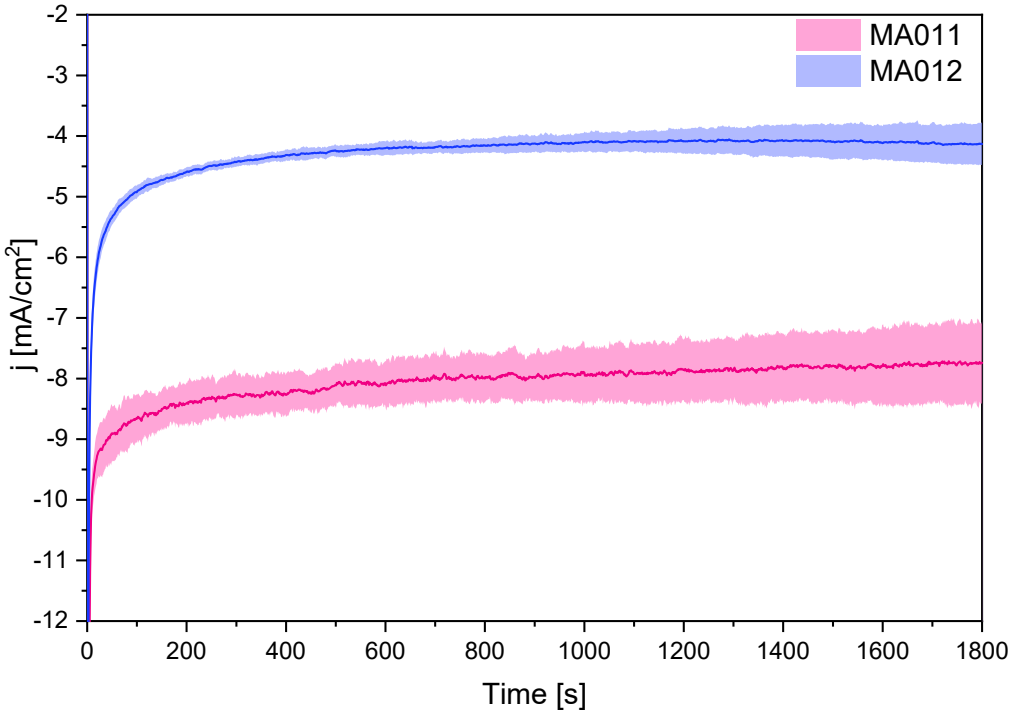

Figure 37: Chronoamperometry test, with mean curve and error, of BiNPs@AC-AcOH materials.

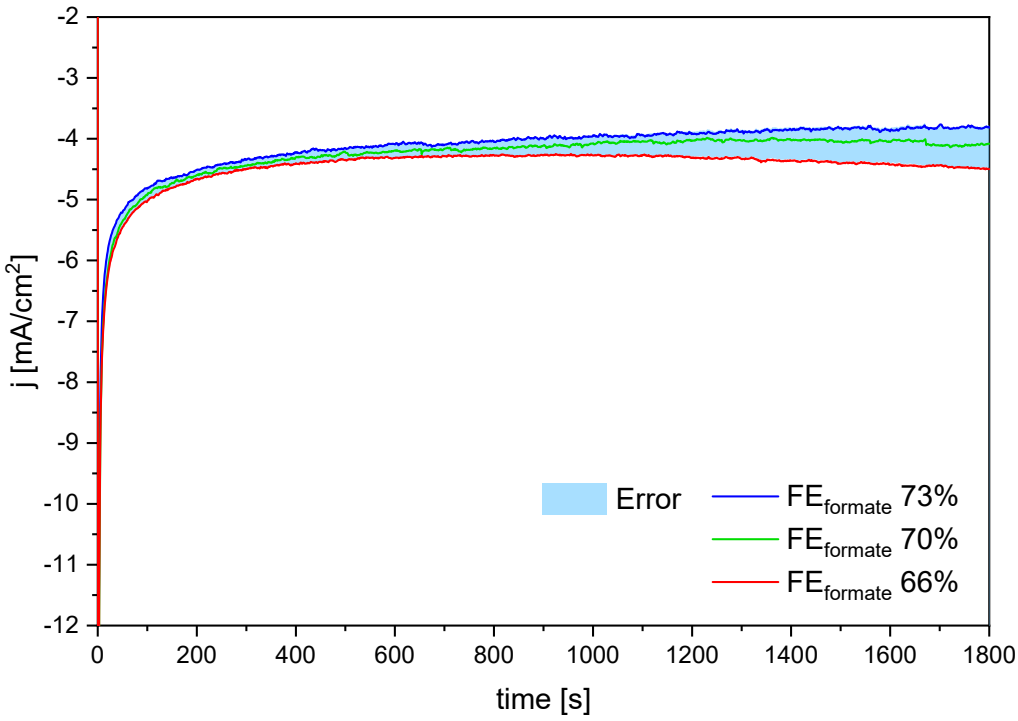

Figure 38: Chronoamperometry tests of MA012. The R_u of blue, green and red line was 3.6, 3.5 and 3.2 respectively.

In the red and green curves, an increase in current density is observed beginning around 800 s. A similar feature was noted in the CA test of bare activated carbon (Appendix C), indicating a possible contribution from the support material. Notably, a larger increase in

current density is associated with a lower $FE_{formate}$, which is consistent with 0% Faradaic efficiency toward formate measured for the activated carbon (Appendix C). Additionally, the variability among the three CA curves implies non-uniformity in the catalyst coating or distribution across different regions of the electrode.

4 Conclusion and future developments

This project on Bi-based electrocatalyst for the electrochemical reduction of CO_2 toward formate led to interesting insights into the effect of physico-chemical properties on electrocatalytic activity of these materials. Furthermore, it has outlined promising directions for future development of these systems.

Initially, attempts to reproduce the BiSub@AC-400 material reported by Miola et al.[2] were unsuccessful, despite varying several synthesis parameters. The main difference was the absence of bismutite ($(BiO)_2CO_3$), a crystalline phase not detected in any XRD analyses of the synthesized samples. This highlights the need to elucidate the mechanism of bismutite formation under pyrolytic conditions, with particular attention to understanding the role of synthesis parameters such as temperature, atmosphere, and flow rate in controlling its nucleation and growth.

The effect of changing synthesis conditions on the properties and performance of BiSub@AC-400 materials was systematically investigated. Among these parameters, stirring rate was found to have minimal impact. Specifically, materials MA003 and MA004, synthesized using different stirring rates, demonstrated nearly identical current densities (-8.8 and -8.7 mA/cm^2, respectively) and $FE_{formate}$ (84 ± 4% and 83 ± 5%, respectively).
In contrast, a notable change in catalytic activity was observed when switching the batch of the bismuth precursor (BiSub). Specifically, MA003 and MA004, prepared using a second batch of BiSub, exhibited higher current density than MA001 (-7.6 mA/cm^2) synthesized from the first batch. XRD analysis revealed that the second batch favored the formation of hexagonal Bi, as suggested by the lower rhombohedral-to-hexagonal peak area ratios of MA003 and MA004 compared to MA001 and MA002. This phase difference is likely due to presence of diverse impurities in the batches, which may have promoted preferential growth of the hexagonal phase. The improved performance of MA003 and MA004 may be attributed to this increased fraction of the hexagonal Bi phase, which exposes a higher proportion of high-index facets (e.g., (012), (104)) known for their superior catalytic activity.
This structure–activity relationship could be studied further using DFT simulations to compare the reactivity of different bismuth crystal facets. Additionally, the development of a synthesis method capable of selectively promoting the formation of high-energy surface would be of great interest for optimizing bismuth-based electrocatalysts for CO_2-to-formate conversion.

Materials MA010 and MA011 exhibited lower catalytic performance compared to MA003 and MA004. Precisely, MA010 and MA011 reached current densities of -7.7 mA/cm^2 and -7.8 mA/cm^2, with corresponding Faradaic efficiencies of 75 ± 6% and 82 ± 3%, respectively. These catalytic performance reductions were unexpected, given the improved dispersion of Bi over the AC surface (Figure 18, 30) and the reduced rhombohedral-to-hexagonal peak area ratios. Two possible explanations are: (i) the presence of amorphous bismuth, supported by XRD (Figure 24), TEM (Figure 25) and TGA (Figure 31) analysis, and consistent with literature reports; and (ii) a decrease in surface wettability, which may have reduced the electrochemically active area.

The effect of the BiSub:AC ratio was investigated on BiNPs@AC-AcOH materials. Reducing the bismuth content significantly enhanced the electrocatalytic activity normalized by bismuth mass, increasing from -0.36 to -1.07 mA/cm^2·mg with a 90 wt% decrease in

BiSub. This improvement likely results from both reduced NPs size and a higher proportion of the hexagonal bismuth phase. However, MA012 showed a lower Faradaic efficiency compared to all other materials, potentially due to insufficient coverage of the AC surface. Two promising directions for future development of BiNPs@AC-AcOH include: (i) conducting electrochemical testing at lower overpotential, only 0.88 V was evaluated in this study; and (ii) slightly increasing the BiSub:AC ratio to enhance surface coverage, while maintaining the observed benefits on NPs size and bismuth phase composition.
Moreover, integrating surfactants during synthesis, as discussed in section 1, could further improve nanoparticles size control. Since the presence of AC can lower the Faradaic efficiency, an alternative approach could focus on synthesizing Bi-based catalysts using surfactants alone.

Lastly, stability testing of BiSub@AC-400, BiNPs@AC-SA, and BiNPs@AC-AcOH electrocatalysts represents a useful future development. It would be particularly interesting to investigate whether the amorphous Bi-based phases, formed in BiNPs@AC-SA and BiNPs@AC-AcOH, transform into crystalline phases under electrochemical conditions. The electrocrystallization of Bi/Bi_2O_3 has been already observed.[79] If, as previously discussed in section 3, the amorphous Bi/Bi_2O_3 phases exhibit lower catalytic activity, their crystallization could potentially enhance electrocatalyst performance over time.

In conclusion, this work has demonstrated how tuning synthesis conditions, including precursor batch, Bi content, and synthesis methodology, can significantly affect the phase structure, particle morphology, and ultimately the electrocatalytic activity of Bi-based materials for CO_2 electroreduction to formate. These findings contribute to a deeper understanding of the structure–activity relationships in Bi-based electrocatalysts and provide a foundation for future efforts aimed at developing high-performance, stable, and scalable systems for ECO_2RR.

References

[1] https://ourworldindata.org/co2-emissions.

[2] Matteo Miola, Bart CA de Jong, and Paolo P Pescarmona. An efficient method to prepare supported bismuth nanoparticles as highly selective electrocatalyst for the conversion of co 2 into formate. *Chemical Communications*, 56(95):14992–14995, 2020.

[3] Darkwah Williams Kweku, Odum Bismark, Addae Maxwell, Koomson Ato Desmond, Kwakye Benjamin Danso, Ewurabena Asante Oti-Mensah, Asenso Theophilus Quachie, and Buanya Beryl Adormaa. Greenhouse effect: greenhouse gases and their impact on global warming. *Journal of Scientific research and reports*, 17(6):1–9, 2018.

[4] Alexey Mikhaylov, Nikita Moiseev, Kirill Aleshin, and Thomas Burkhardt. Global climate change and greenhouse effect. *Entrepreneurship and Sustainability Issues*, 7(4):2897, 2020.

[5] David Schimel, LG Enting, Martin Heimann, TML ML Wigley, D Raynaud, D Alves, U Siegenthaler, S Brown, WR R Emanuel, M Fasham, et al. C02 and the carbon cycle. *Climate Change 1994: Radiative Forcing of Climate Change and an Evaluation of the IPCC IS92 Emission Scenarios*, 1995.

[6] Sahil Garg, Mengran Li, Adam Z Weber, Lei Ge, Liye Li, Victor Rudolph, Guoxiong Wang, and Thomas E Rufford. Advances and challenges in electrochemical co 2 reduction processes: an engineering and design perspective looking beyond new catalyst materials. *Journal of Materials Chemistry A*, 8(4):1511–1544, 2020.

[7] Alina Gawel, Theresa Jaster, Daniel Siegmund, Johannes Holzmann, Heiko Lohmann, Elias Klemm, and Ulf-Peter Apfel. Electrochemical co2 reduction-the macroscopic world of electrode design, reactor concepts & economic aspects. *IScience*, 25(4), 2022.

[8] Philip H Rieger. *Electrochemistry*. Springer Science & Business Media, 2012.

[9] Allen J Bard, Larry R Faulkner, and Henry S White. *Electrochemical methods: fundamentals and applications*. John Wiley & Sons, 2022.

[10] Robert C Weast. *CRC handbook of chemistry and physics*. CRC Press Inc., 1986.

[11] Weiwei Quan, Yingbin Lin, Yongjin Luo, and Yiyin Huang. Electrochemical co2 reduction on cu: synthesis-controlled structure preference and selectivity. *Advanced Science*, 8(23):2101597, 2021.

[12] Parminder S Surdhar, Stephen P Mezyk, and David A Armstrong. Reduction potential of the carboxyl radical anion in aqueous solutions. *The Journal of Physical Chemistry*, 93(8):3360–3363, 1989.

[13] B Patrick Sullivan, K Krist, and HE Guard. *Electrochemical and electrocatalytic reactions of carbon dioxide*. Elsevier, 2012.

[14] Gaston A East and MA Del Valle. Easy-to-make ag/agcl reference electrode. *Journal of Chemical Education*, 77(1):97, 2000.

[15] Yoshio Hori, Katsuhei Kikuchi, and Shin Suzuki. Production of co and ch4 in electrochemical reduction of co2 at metal electrodes in aqueous hydrogencarbonate solution. *Chemistry letters*, 14(11):1695–1698, 1985.

[16] Yoshio Hori, Katsuhei Kikuchi, Akira Murata, and Shin Suzuki. Production of methane and ethylene in electrochemical reduction of carbon dioxide at copper electrode in aqueous hydrogencarbonate solution. *Chemistry Letters*, 15(6):897–898, 1986.

[17] Qi Lu and Feng Jiao. Electrochemical co2 reduction: Electrocatalyst, reaction mechanism, and process engineering. *Nano Energy*, 29:439–456, 2016.

[18] Otmane Zoubir, Lahoucine Atourki, Hassan Ait Ahsaine, and Amal BaQais. Current state of copper-based bimetallic materials for electrochemical co 2 reduction: a review. *RSC advances*, 12(46):30056–30075, 2022.

[19] Douglas R Kauffman, Jay Thakkar, Rajan Siva, Christopher Matranga, Paul R Ohodnicki, Chenjie Zeng, and Rongchao Jin. Efficient electrochemical co2 conversion powered by renewable energy. *ACS applied materials & interfaces*, 7(28):15626–15632, 2015.

[20] Theresa Jaster, Alina Gawel, Daniel Siegmund, Johannes Holzmann, Heiko Lohmann, Elias Klemm, and Ulf-Peter Apfel. Electrochemical co2 reduction toward multicarbon alcohols-the microscopic world of catalysts & process conditions. *Iscience*, 25(4), 2022.

[21] Andrew A Peterson, Frank Abild-Pedersen, Felix Studt, Jan Rossmeisl, and Jens K Nørskov. How copper catalyzes the electroreduction of carbon dioxide into hydrocarbon fuels. *Energy & Environmental Science*, 3(9):1311–1315, 2010.

[22] Andrew A Peterson and Jens K Nørskov. Activity descriptors for co2 electroreduction to methane on transition-metal catalysts. *The Journal of Physical Chemistry Letters*, 3(2):251–258, 2012.

[23] Heine A Hansen, Joel B Varley, Andrew A Peterson, and Jens K Nørskov. Understanding trends in the electrocatalytic activity of metals and enzymes for co2 reduction to co. *The journal of physical chemistry letters*, 4(3):388–392, 2013.

[24] Ruud Kortlever, Jing Shen, Klaas Jan P Schouten, Federico Calle-Vallejo, and Marc TM Koper. Catalysts and reaction pathways for the electrochemical reduction of carbon dioxide. *The journal of physical chemistry letters*, 6(20):4073–4082, 2015.

[25] Na Han, Pan Ding, Le He, Youyong Li, and Yanguang Li. Promises of main group metal–based nanostructured materials for electrochemical co2 reduction to formate. *Advanced Energy Materials*, 10(11):1902338, 2020.

[26] Sudipta Chatterjee, Indranil Dutta, Yanwei Lum, Zhiping Lai, and Kuo-Wei Huang. Enabling storage and utilization of low-carbon electricity: power to formic acid. *Energy & Environmental Science*, 14(3):1194–1246, 2021.

[27] Fanxu Meng, Zihan Shen, Xinlong Lin, Pengfei Song, Tianze Wu, Shibo Xi, Chao Wu, Zhenhui Ma, Daniel Mandler, and Zhichuan J Xu. Industrially viable formate production with 50% lower co2 emissions. *Energy & Environmental Science*, 18(8):3680–3688, 2025.

[28] Chi Chen, Juliet F Khosrowabadi Kotyk, and Stafford W Sheehan. Progress toward commercial application of electrochemical carbon dioxide reduction. *Chem*, 4(11):2571–2586, 2018.

[29] Zihao Wang, Junying Yan, Huangying Wang, Weicheng Fu, Duyi He, Baoying Wang, Yaoming Wang, and Tongwen Xu. Separation and conversion of co2 reduction products into high-concentration formic acid using bipolar membrane electrodialysis. *Journal of Membrane Science*, 708:123016, 2024.

[30] Wooseok Oh, Choong Kyun Rhee, Jeong Woo Han, and Bonggeun Shong. Atomic and molecular adsorption on the bi (111) surface: insights into catalytic co2 reduction. *The Journal of Physical Chemistry C*, 122(40):23084–23090, 2018.

[31] Yayu Guan, Minmin Liu, Xufeng Rao, Yuyu Liu, and Jiujun Zhang. Electrochemical reduction of carbon dioxide (co 2): bismuth-based electrocatalysts. *Journal of Materials Chemistry A*, 9(24):13770–13803, 2021.

[32] Tung-Han Yang, Jaewan Ahn, Shi Shi, and Dong Qin. Understanding the role of poly (vinylpyrrolidone) in stabilizing and capping colloidal silver nanocrystals. *ACS nano*, 15(9):14242–14252, 2021.

[33] Hui Yang, Na Han, Jun Deng, Jinghua Wu, Yu Wang, Yongpan Hu, Pan Ding, Yafei Li, Yanguang Li, and Jun Lu. Selective co2 reduction on 2d mesoporous bi nanosheets. *Advanced Energy Materials*, 8(35):1801536, 2018.

[34] Na Han, Yu Wang, Hui Yang, Jun Deng, Jinghua Wu, Yafei Li, and Yanguang Li. Ultrathin bismuth nanosheets from in situ topotactic transformation for selective electrocatalytic co2 reduction to formate. *Nature communications*, 9(1):1320, 2018.

[35] Xia Zhang, Xiaofan Hou, Qi Zhang, Yixiao Cai, Yuyu Liu, and Jinli Qiao. Polyethylene glycol induced reconstructing bi nanoparticle size for stabilized co2 electroreduction to formate. *Journal of Catalysis*, 365:63–70, 2018.

[36] Qiufang Gong, Pan Ding, Mingquan Xu, Xiaorong Zhu, Maoyu Wang, Jun Deng, Qing Ma, Na Han, Yong Zhu, Jun Lu, et al. Structural defects on converted bismuth oxide nanotubes enable highly active electrocatalysis of carbon dioxide reduction. *Nature communications*, 10(1):2807, 2019.

[37] Peilin Deng, Hongming Wang, Ruijuan Qi, Jiexin Zhu, Shenghua Chen, Fan Yang, Liang Zhou, Kai Qi, Hongfang Liu, and Bao Yu Xia. Bismuth oxides with enhanced bismuth–oxygen structure for efficient electrochemical reduction of carbon dioxide to formate. *ACS Catalysis*, 10(1):743–750, 2019.

[38] Peilong Lu, Denglei Gao, Hongyan He, Qiaoxin Wang, Zhanjun Liu, Sobia Dipazir, Menglei Yuan, Wenyue Zu, and Guangjin Zhang. Facile synthesis of a bismuth nanostructure with enhanced selectivity for electrochemical conversion of co 2 to formate. *Nanoscale*, 11(16):7805–7812, 2019.

[39] Paolo Lamagni, Matteo Miola, Jacopo Catalano, Mathias S Hvid, Mohammad Aref H Mamakhel, Mogens Christensen, Monica R Madsen, Henrik S Jeppesen, Xin-Ming Hu, Kim Daasbjerg, et al. Restructuring metal–organic frameworks to nanoscale bismuth electrocatalysts for highly active and selective co2 reduction to formate. *Advanced Functional Materials*, 30(16):1910408, 2020.

[40] Ke Fan, Yufei Jia, Yongfei Ji, Panyong Kuang, Bicheng Zhu, Xiangyu Liu, and Jiaguo Yu. Curved surface boosts electrochemical co2 reduction to formate via bismuth nanotubes in a wide potential window. *Acs Catalysis*, 10(1):358–364, 2019.

[41] Alexandros Ch Lazanas and Mamas I Prodromidis. Electrochemical impedance spectroscopy a tutorial. *ACS measurement science au*, 3(3):162–193, 2023.

[42] Lloyd R Snyder, Joseph J Kirkland, and John W Dolan. *Introduction to modern liquid chromatography*. John Wiley & Sons, 2011.

[43] `https://qiserver.ugr.es/cod/`.

[44] Ivan Zelocualtecatl Montiel, Abhijit Dutta, Kiran Kiran, Alain Rieder, Anna Iarchuk, Soma Vesztergom, Marta Mirolo, Isaac Martens, Jakub Drnec, and Peter Broekmann. Co2 conversion at high current densities: Stabilization of bi (iii)-containing electrocatalysts under co2 gas flow conditions. *ACS Catalysis*, 12(17):10872–10886, 2022.

[45] Jose Luis Ortiz-Quiñonez, Carolina Vega-Verduga, David Díaz, and Inti Zumeta-Dubé. Transformation of bismuth and β-bi2o3 nanoparticles into (bio) 2co3 and (bio) 4 (oh) 2co3 by capturing co2: the role of halloysite nanotubes and "sunlight" on the crystal shape and size. *Crystal Growth & Design*, 18(8):4334–4346, 2018.

[46] Joël Brugger, Blake Tooth, Barbara Etschmann, Weihua Liu, Denis Testemale, Jean-Louis Hazemann, and Pascal V Grundler. Structure and thermal stability of bi (iii) oxy-clusters in aqueous solutions. *Journal of Solution Chemistry*, 43:314–325, 2014.

[47] A Ken Inge. In the pink with bismuth subsalicylate. *Nature Chemistry*, 16(7):1210–1210, 2024.

[48] Xun Lv, Ling Zhang, Feifei Xing, and Hengwei Lin. Controlled synthesis of monodispersed mesoporous silica nanoparticles: Particle size tuning and formation mechanism investigation. *Microporous and Mesoporous Materials*, 225:238–244, 2016.

[49] Eduardo Hernández-Silva, Fabiola Vázquez-Hernández, Salvador Mendoza-Acevedo, Mario Pérez-González, Sergio Tomás-Velázquez, Patricia Rodríguez-Fragoso, Julio Mendoza-Álvarez, and Pedro Juan Luna-Arias. Effect of stirring rate on the size of hydroxyapatite nanoparticles synthesized by a modified heat-treated precipitation method. *Processing and Application of Ceramics*, 17(2):133–139, 2023.

[50] Yongde Xia and Robert Mokaya. To stir or not to stir: formation of hierarchical superstructures of molecularly ordered ethylene-bridged periodic mesoporous organosilicas. *Journal of Materials Chemistry*, 16(4):395–400, 2006.

[51] MA García, V Bouzas, and N Carmona. Influence of stirring in the synthesis of gold nanorods. *Materials Chemistry and Physics*, 127(3):446–450, 2011.

[52] Zongjian Liu, Yuanyuan Chen, and Yifan Zheng. Stirring-induced growth of hierarchical cu structures in the presence of diamine. *CrystEngComm*, 16(38):9054–9062, 2014.

[53] Yujiang Song, Robert M Garcia, Rachel M Dorin, Haorong Wang, Yan Qiu, Eric N Coker, William A Steen, James E Miller, and John A Shelnutt. Synthesis of platinum nanowire networks using a soft template. *Nano letters*, 7(12):3650–3655, 2007.

[54] Mohd Farhan Khan, Akhter H Ansari, M Hameedullah, Ejaz Ahmad, Fohad Mabood Husain, Qamar Zia, Umair Baig, Mohd Rehan Zaheer, Mohammad Mezbaul Alam, Abu Mustafa Khan, et al. Sol-gel synthesis of thorn-like zno nanoparticles endorsing mechanical stirring effect and their antimicrobial activities: Potential role as nano-antibiotics. *Scientific reports*, 6(1):27689, 2016.

[55] Roberto Valenzuela, María Cecilia Fuentes, Carolina Parra, Jaime Baeza, Nelson Duran, SK Sharma, Marcelo Knobel, and Juanita Freer. Influence of stirring velocity on the synthesis of magnetite nanoparticles (fe3o4) by the co-precipitation method. *Journal of Alloys and Compounds*, 488(1):227–231, 2009.

[56] Wen Xiao, Yanbing Guo, Zheng Ren, Gregory Wrobel, Zhuyin Ren, Tianfeng Lu, and Pu-Xian Gao. Mechanical-agitation-assisted growth of large-scale and uniform zno nanorod arrays within 3d multichannel monolithic substrates. *Crystal growth & design*, 13(8):3657–3664, 2013.

[57] Fan Qin, Guangfang Li, Runming Wang, Jiliang Wu, Hongzhe Sun, and Rong Chen. Template-free fabrication of bi2o3 and (bio) 2co3 nanotubes and their application in water treatment. *Chemistry–A European Journal*, 18(51):16491–16497, 2012.

[58] Shiyuan Liu, Botao Hu, Junkai Zhao, Wenjun Jiang, Deqiang Feng, Ce Zhang, and Wei Yao. Enhanced electrocatalytic co2 reduction of bismuth nanosheets with introducing surface bismuth subcarbonate. *Coatings*, 12(2):233, 2022.

[59] Erik Svensson Grape, Victoria Rooth, Mathias Nero, Tom Willhammar, and A Ken Inge. Structure of the active pharmaceutical ingredient bismuth subsalicylate. *Nature Communications*, 13(1):1–7, 2022.

[60] Sema Akay, Berkant Kayan, María Ángeles Peña, Abolghasem Jouyban, and Fleming Martínez. Solubility of salicylic acid in some (ethanol+ water) mixtures at different temperatures: determination, correlation, thermodynamics and preferential solvation. *International Journal of Thermophysics*, 44(8):121, 2023.

[61] AK Mandal and SC Lahiri. Determination of the dissociation constants of salicylic acid in water-ethanol mixtures by modified conductometric methods. *Bulletin of the Chemical Society of Japan*, 49(7):1829–1831, 1976.

[62] EV Timakova, TA Udalova, and Yu M Yukhin. Precipitation of bismuth (iii) salicylates from mineral acid solutions. *Russian Journal of Inorganic Chemistry*, 54:873–880, 2009.

[63] P Lunca Popa, Steffen Sønderby, Sit Kerdsongpanya, Jun Lu, Hans Arwin, and Per Eklund. Structural, morphological, and optical properties of bi2o3 thin films grown by reactive sputtering. *Thin Solid Films*, 624:41–48, 2017.

[64] Ye Chen, Zhuangchai Lai, Xiao Zhang, Zhanxi Fan, Qiyuan He, Chaoliang Tan, and Hua Zhang. Phase engineering of nanomaterials. *Nature Reviews Chemistry*, 4(5):243–256, 2020.

[65] MG Hapase, VB Tare, and AB Biswas. Oxidation of bismuth. *Acta Metallurgica*, 15(1):131–133, 1967.

[66] William F.. Smith and Javad Hashemi. *Foundations of materials science and engineering*. Mcgraw-Hill Publishing, 2006.

[67] VM Egorov, ON Uryupin, and Yu V Ivanov. Crystallization temperature of bismuth microparticles. *Physics of the Solid State*, 57:1846–1849, 2015.

[68] Suhaib Alam, Hiromi Yamashita, and Priyanka Verma. Unveiling the critical role of high-/low-index facets in nanostructured energy materials for enhancing the photoelectrochemical water splitting. *ChemCatChem*, 17(5):e202401672, 2025.

[69] Shaodong Sun and Zhimao Yang. Recent advances in tuning crystal facets of polyhedral cuprous oxide architectures. *RSC advances*, 4(8):3804–3822, 2014.

[70] Shaodong Sun, Xiaochuan Zhang, Jie Cui, and Shuhua Liang. Identification of the miller indices of a crystallographic plane: a tutorial and a comprehensive review on fundamental theory, universal methods based on different case studies and matters needing attention. *Nanoscale*, 12(32):16657–16677, 2020.

[71] Ping Li, Xingyu Chen, Huichao He, Xin Zhou, Yong Zhou, and Zhigang Zou. Polyhedral 30-faceted bivo4 microcrystals predominantly enclosed by high-index planes promoting photocatalytic water-splitting activity. *Advanced Materials*, 30(1):1703119, 2018.

[72] Shaodong Sun, Xin Zhang, Jie Cui, Qing Yang, and Shuhua Liang. High-index faceted metal oxide micro-/nanostructures: a review on their characterization, synthesis and applications. *Nanoscale*, 11(34):15739–15762, 2019.

[73] Jai Hyun Koh, Da Hye Won, Taedaehyeong Eom, Nak-Kyoon Kim, Kwang Deog Jung, Hyungjun Kim, Yun Jeong Hwang, and Byoung Koun Min. Facile CO2 electroreduction to formate via oxygen bidentate intermediate stabilized by high-index planes of Bi dendrite catalyst. *ACS Catalysis*, 7(8):5071–5077, 2017.

[74] Gang Liu, C Yu Jimmy, Gao Qing Max Lu, and Hui-Ming Cheng. Crystal facet engineering of semiconductor photocatalysts: motivations, advances and unique properties. *Chemical Communications*, 47(24):6763–6783, 2011.

[75] Chenchen Qin, Li Xu, Jian Zhang, Jun Wang, Jiaxin He, Daomeng Liu, Jia Yang, Juan-Ding Xiao, Xifan Chen, Hong-Bao Li, et al. Phase interface regulating on amorphous/crystalline bismuth catalyst for boosted electrocatalytic co2 reduction to formate. *ACS Applied Materials & Interfaces*, 15(40):47016–47024, 2023.

[76] Chengbo Li, Xian Zhong, Yuan Ji, Yawei Hong, Jiawei Li, Youpeng Wang, Hongliang Zeng, Chunxiao Liu, Zhaoyang Chen, Xu Li, et al. Surface amorphization of bismuth for efficient acidic co2 electrolysis. *ACS nano*, 2025.

[77] Yujing Ji, Jichuang Wu, Ha Eun Lee, Yongsu An, Duk-Young Jung, Chan Woo Lee, Young Dok Kim, and Hyun Ook Seo. Relationships between the surface hydrophilicity of a bismuth electrode and the product selectivity of electrocatalytic co2 reduction. *ACS omega*, 9(49):48855–48866, 2024.

[78] Hongsik Yoon, Taijin Min, Sung-Hwan Kim, Gunhee Lee, Dasom Oh, Dong-Chan Choi, and Seongsoo Kim. Effect of activated carbon electrode material characteristics on hardness control performance of membrane capacitive deionization. *RSC advances*, 13(45):31480–31486, 2023.

[79] Zoran Grubač and Mirjana Metikoš-Huković. Kinetics and mechanism of electrocrystallization of bismuth in oxide matrix. *Electrochimica acta*, 44(25):4559–4571, 1999.

[80] Harald Günther. *NMR spectroscopy: basic principles, concepts and applications in chemistry*. John Wiley & Sons, 2013.

[81] Mariana CO Monteiro, Leon Jacobse, Thomas Touzalin, and Marc TM Koper. Mediator-free secm for probing the diffusion layer ph with functionalized gold ultramicroelectrodes. *Analytical chemistry*, 92(2):2237–2243, 2019.

[82] Mariana CO Monteiro, Leon Jacobse, and Marc TM Koper. Understanding the voltammetry of bulk co electrooxidation in neutral media through combined secm measurements. *The journal of physical chemistry letters*, 11(22):9708–9713, 2020.

[83] Mariana CO Monteiro, Alex Mirabal, Leon Jacobse, Katharina Doblhoff-Dier, Scott Calabrese Barton, and Marc TM Koper. Time-resolved local ph measurements during co2 reduction using scanning electrochemical microscopy: Buffering and tip effects. *Jacs Au*, 1(11):1915–1924, 2021.

[84] Fredrik L Nordström and Åke C Rasmuson. Solubility and melting properties of salicylic acid. *Journal of Chemical & Engineering Data*, 51(5):1668–1671, 2006.

A Degradation of bismuth subsalicylate

Materials

Bismuth(III) subsalicylate 99.9% (BiSub), purchased from Sigma-Aldrich.

Methods & Results

First of all, an XRD analysis of both the powder was done. In Figure 39 both the patterns are shown, the one of the old BiSub is shifted on the y-axes of +100000 to reduce the overlap of the curves.

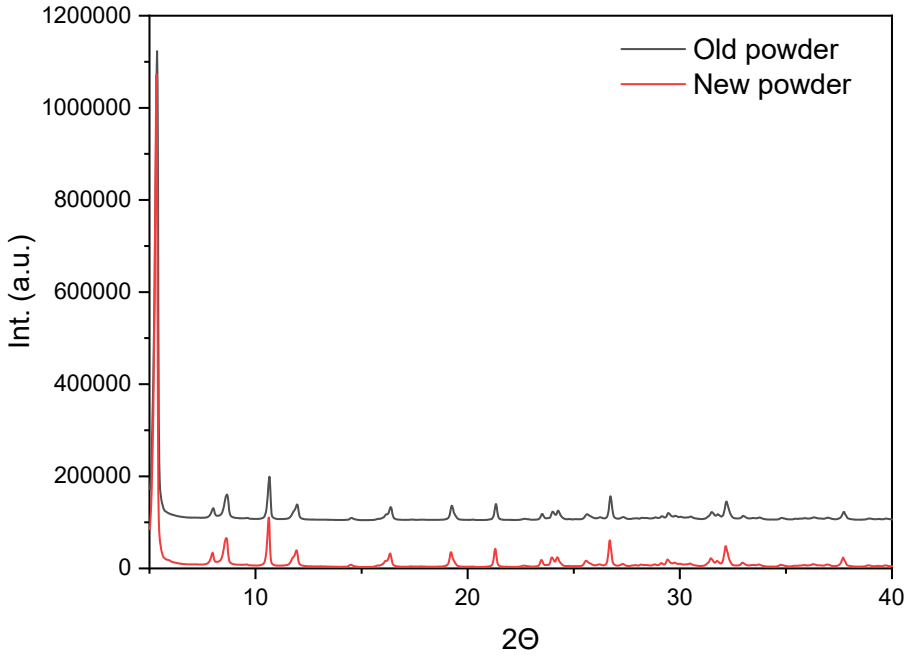

Figure 39: XRD patterns of the old and the new BiSub powders.

The patterns do not show relevant differences.

To investigate the degradation of the BiSub an H-NMR analysis was done in methanol-D_4, since the salicylic acid is soluble in alcohol, to look for differences in the intensity of the related to the hydrogen of the benzyl ring. In Figure 40 are shown the spectra of both the old and the new powder of bismuth subsalicylate.
The spectra in Figure 40 show three peaks around 7 ppm, they can all be attributed to hydrogen atoms present in the salicylic acid molecule.[80] In particular, starting from the peak at lower ppm, we can relate the peaks with those groups: the benzene ring, the phenol and the carboxylic group.

Using the results of the XRD and the H-NMR (Figure 39, Figure 40) it is difficult to understand if the old powder was really degradated or not.

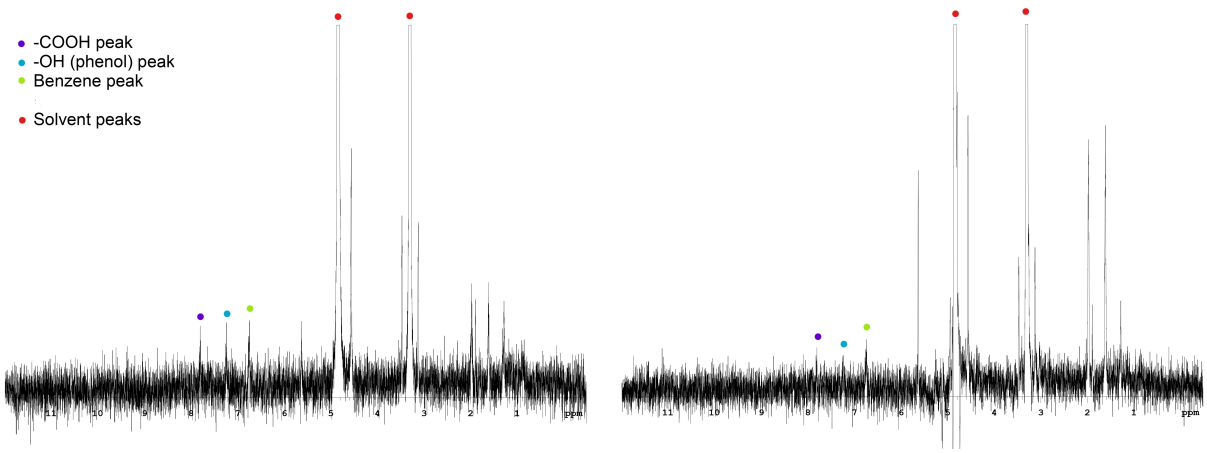

(a) NMR pattern of the old powder of BiSub. **(b)** NMR pattern of the new powder of BiSub.

Figure 40: NMR pattern of BiSub with the peaks label.

B Convolution of XRD peaks

The deconvolution of the XRD pattern peaks was done to apply the Scherrer equation and to measure the rhombohedral-to-hexagonal peak area ratios.
To estimate the crystallite size the main peaks of rhomboedrical and hexagonal bismuth and Bi_2O_3 phases were used. Figure 41 and 42 show the fitting of these peaks of all the materials. In all the fitting images, the experimental pattern is shown in black, the individual pseudo-Voigt curves in orange, and the overall fit in light blue.

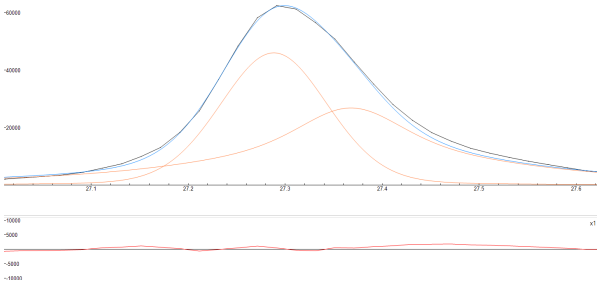

(a) Fitting of the main bismuth peaks of MA010.

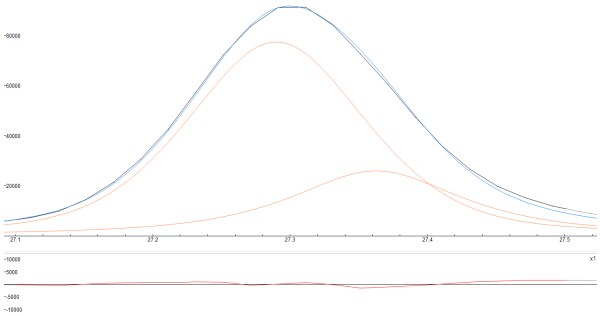

(b) Fitting of the main bismuth peaks of MA011.

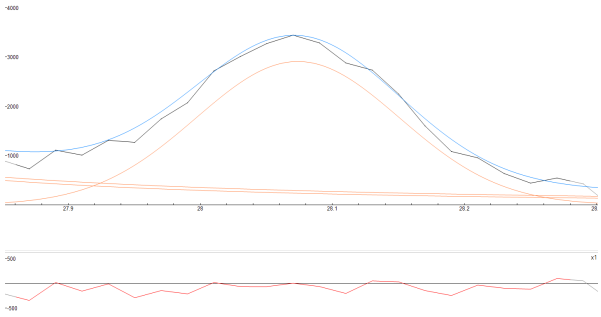

(c) Fitting of the main bismuth oxide peak of MA011.

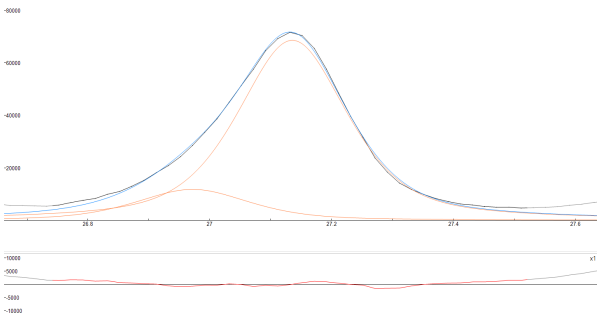

(d) Fitting of the main bismuth peaks of MA012.

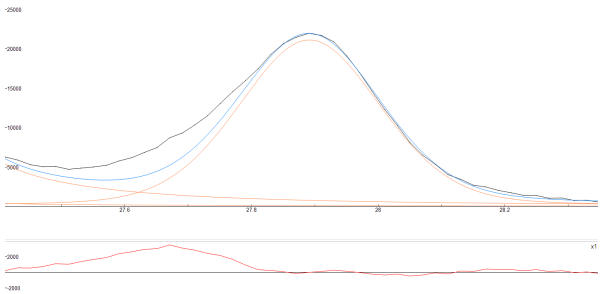

(e) Fitting of the main bismuth oxide peak of MA012.

Figure 42: Fitting of the main peaks of the bismuth and bismuth oxide phases of BiNPs@AC-SA and BiNPs@AC-AcOH materials.

The measurement of the rhombohedral-to-hexagonal peak area ratios was done using both the main peaks and the peaks around 64°-65° 2θ. In Figure 43 are reported the Fitting of all the materials.

In Table 8, 9, 10, 11, 12, 13 and 14 are reported all the data of the Pseudo-Voigt curves.

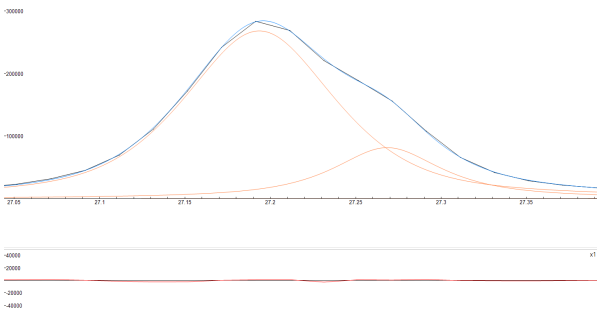

(a) Fitting of the main bismuth peaks of MA001.

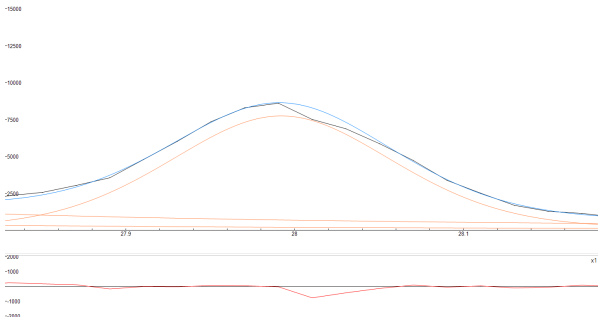

(b) Fitting of the main bismuth oxide peak of MA001.

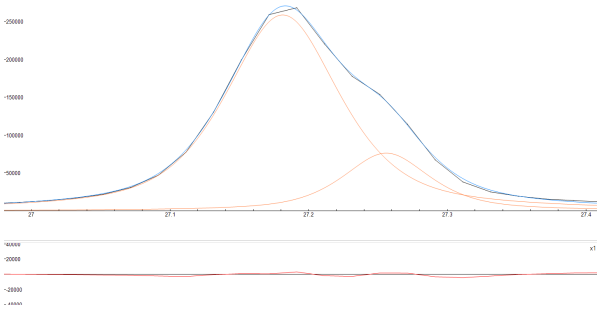

(c) Fitting of the main bismuth peaks of MA002.

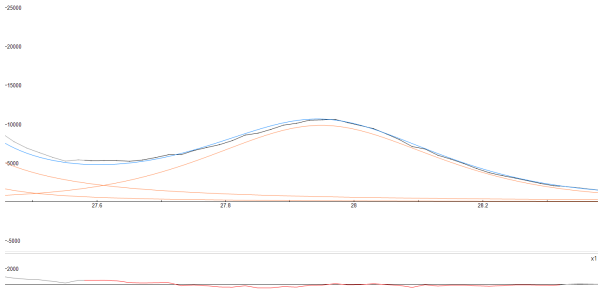

(d) Fitting of the main bismuth oxide peak of MA002.

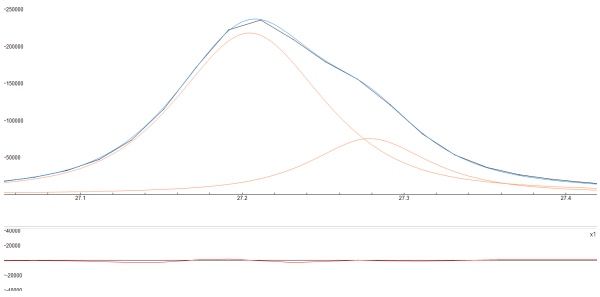

(e) Fitting of the main bismuth peaks of MA003.

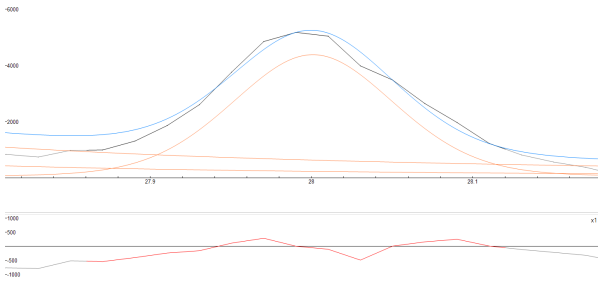

(f) Fitting of the main bismuth oxide peak of MA003.

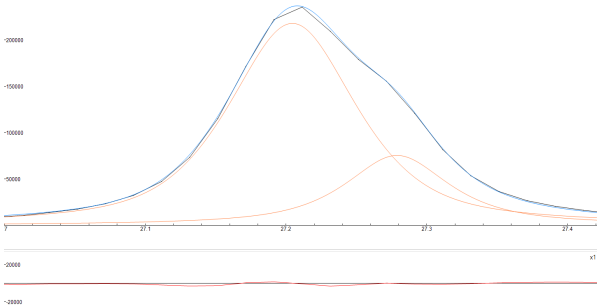

(g) Fitting of the main bismuth peaks of MA004.

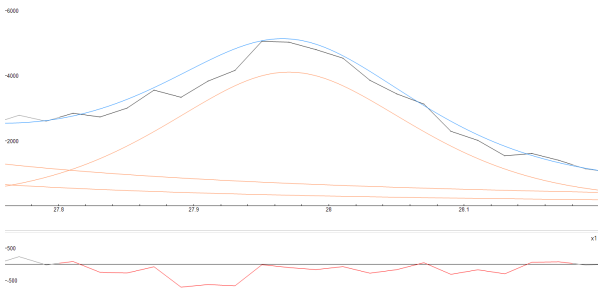

(h) Fitting of the main bismuth oxide peak of MA004.

Figure 41: Fitting of the main peaks of the bismuth and bismuth oxide phases of BiSub@AC-400 materials.

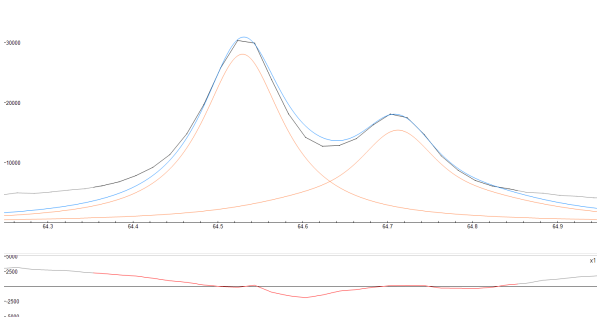

(a) Fitting of MA001.

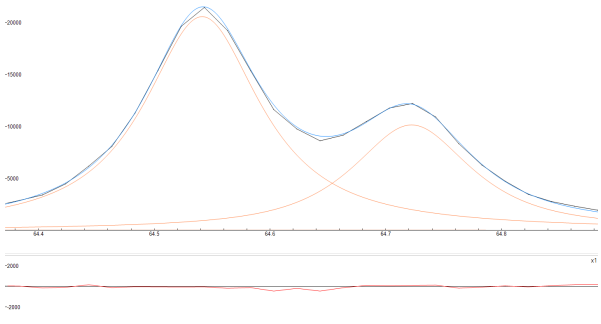

(b) Fitting of MA003.

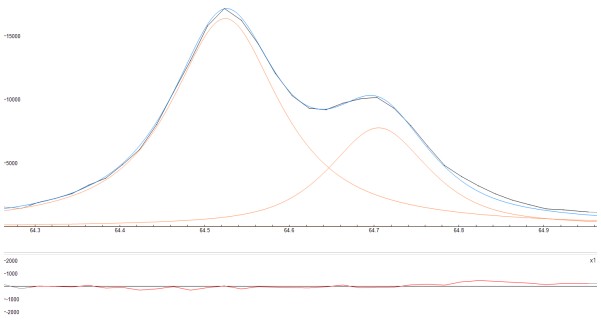

(c) Fitting of MA004.

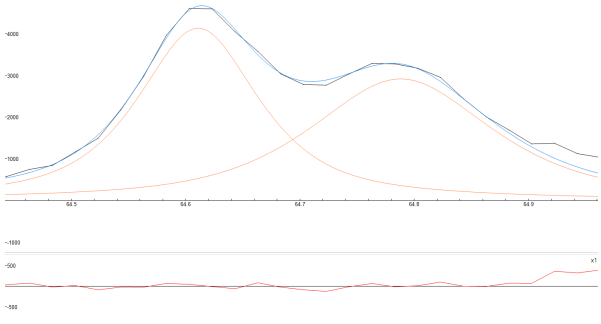

(d) Fitting of MA010.

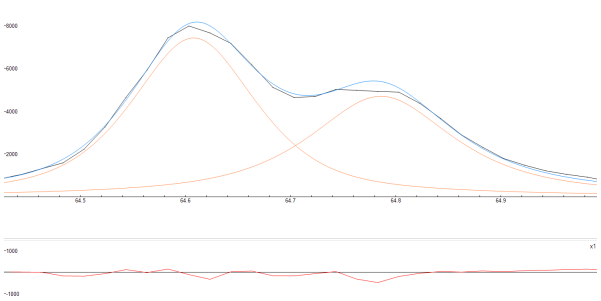

(e) Fitting of MA011.

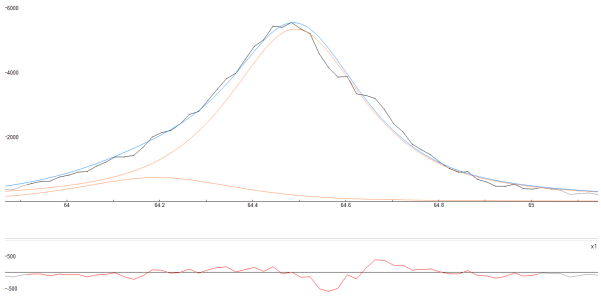

(f) Fitting of MA012.

Figure 43: Fitting of the bismuth peaks around 64°-65° 2θ of all the materials.

Table 8: Convolution curve data of material MA001.

Crystalline phase	FWHM [deg]	2θ position [deg]	Area [Counts]
Rhomboedrical Bi (27° 2θ)	0.105	27.194	38663.3
Hexagonal Bi (27° 2θ)	0.076	27.268	9325.2
Bi_2O_3	0.157	27.992	1443.7
Rhomboedrical Bi (64° 2θ)	0.118	64.529	5181.3
Hexagonal Bi (64° 2θ)	0.140	64.712	3918.2

Table 9: Convolution curve data of material MA002.

Crystalline phase	FWHM [deg]	2θ position [deg]	Area [Counts]
Rhomboedrical Bi (27° 2θ)	0.098	27.181	35141
Hexagonal Bi (27° 2θ)	0.075	27.256	7965.4
Bi_2O_3	0.415	27.949	5380.1

Table 10: Convolution curve data of material MA003.

Crystalline phase	FWHM [deg]	2θ position [deg]	Area [Counts]
Rhomboedrical Bi (27° 2θ)	0.108	27.204	32562.4
Hexagonal Bi (27° 2θ)	0.088	27.279	9889.5
Bi_2O_3	0.120	28.001	613.0
Rhomboedrical Bi (64° 2θ)	0.123	64.541	4052.7
Hexagonal Bi (64° 2θ)	0.124	64.723	1818.6

Table 11: Convolution curve data of material MA004.

Crystalline phase	FWHM [deg]	2θ position [deg]	Area [Counts]
Rhomboedrical Bi (27° 2θ)	0.138	27.186	30355.4
Hexagonal Bi (27° 2θ)	0.134	27.256	10362.8
Bi_2O_3	0.220	27.970	1189.8
Rhomboedrical Bi (64° 2θ)	0.156	64.525	3917.6
Hexagonal Bi (64° 2θ)	0.140	64.705	1557.3

Table 12: Convolution curve data of material MA010.

Crystalline phase	FWHM [deg]	2θ position [deg]	Area [Counts]
Rhomboedrical Bi (27° 2θ)	0.131	27.288	6841.6
Hexagonal Bi (27° 2θ)	0.191	27.365	9070.0
Rhomboedrical Bi (64° 2θ)	0.127	64.611	759.3
Hexagonal Bi (64° 2θ)	0.189	64.788	783.3

Table 13: Convolution curve data of material MA011.

Crystalline phase	FWHM [deg]	2θ position [deg]	Area [Counts]
Rhomboedrical Bi (27° 2θ)	0.153	27.290	15022.9
Hexagonal Bi (27° 2θ)	0.150	27.363	5790.9
Bi_2O_3	0.182	28.074	562.4
Rhomboedrical Bi (64° 2θ)	0.142	64.608	1465.1
Hexagonal Bi (64° 2θ)	0.166	64.786	1160.6

Table 14: Convolution curve data of material MA012.

Crystalline phase	FWHM [deg]	2θ position [deg]	Area [Counts]
Rhomboedrical Bi (27° 2θ)	0.220	26.971	3419
Hexagonal Bi (27° 2θ)	0.214	27.135	19823.7
Bi_2O_3	0.265	27.891	6543
Rhomboedrical Bi (64° 2θ)	0.339	64.194	390.8
Hexagonal Bi (64° 2θ)	0.351	64.492	2762.7

C SEM images of bare AC

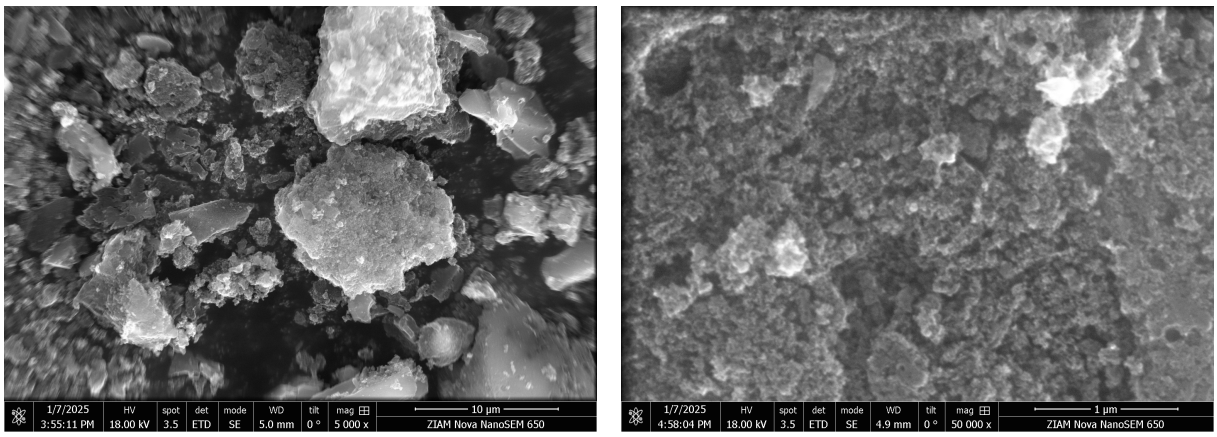

(a) SEM image at 5000 x magnification. **(b)** SEM image at 50000 x magnification.

Figure 44: SEM images of bare AC.

D Electrochemical test: GC electrode and bare AC

Chronoamperometry tests on both GC electrode and bare AC were conducted using the same procedure and experimental conditions reported in section 2.

First of all, the glassy carbon electrode was tested without any catalyst to evaluate its intrinsic electrochemical activity and the inherent variability of the cell configuration. Figure 45 presents the results of three CA measurements performed on GC electrode at -1.7 V vs. Ag/AgCl.
The HPLC analysis was done on the catholyte but no liquid product were detected. However, the formation of gaseous products was observed on the electrode surface.

For the test of bare AC, the electrode preparation procedure followed the same protocol described in section 2, with the only difference being to use 12 mg of AC in the ink formulation instead of the electrocatalyst. After the drying, the AC loading on the electrode was 0.296 mg cm^{-2}. The results of the three CA measurements performed on bare AC at -1.7 V vs. Ag/AgCl are shown in Figure 46.
The bare AC reaches higher current density compared to the synthesized electrocatalysts; however, the Faradaic efficiency toward formate was 0%. Interestingly, also for the bare AC a progressive increase in current density was observed over time. To investigate if this increase was due to activation of the material, the same electrode was tested consecutively in two experiments. After the first test, the electrolyte was replaced with fresh solution, saturated with CO_2 by bubbling for 10 minutes. In Figure 47 the results of the two consecutive test are shown.
As the initial current densities in both tests are comparable, the observed increase in activity over time is unlikely attributable to activation of the AC during the electrochemical test. Instead, this behavior may be attributed to a local increase in pH near the electrode surface, that can increase the overpotential favoring the HER. Such pH change have been previously reported during the electrochemical reduction of CO_2.[81], [82], [83] The interfacial pH can rise due to the formation of OH^- ions, which are generated at the catalyst surface both during the HER and during CO production via the CO_2 reduction pathway

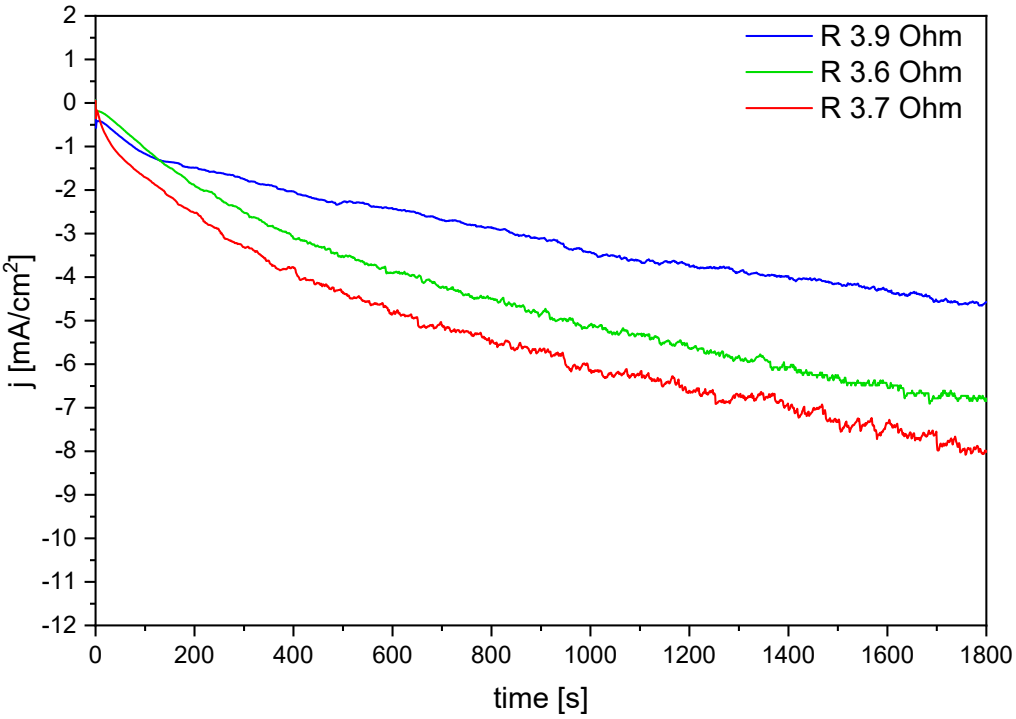

Figure 45: Three CA tests performed on the GC electrode.

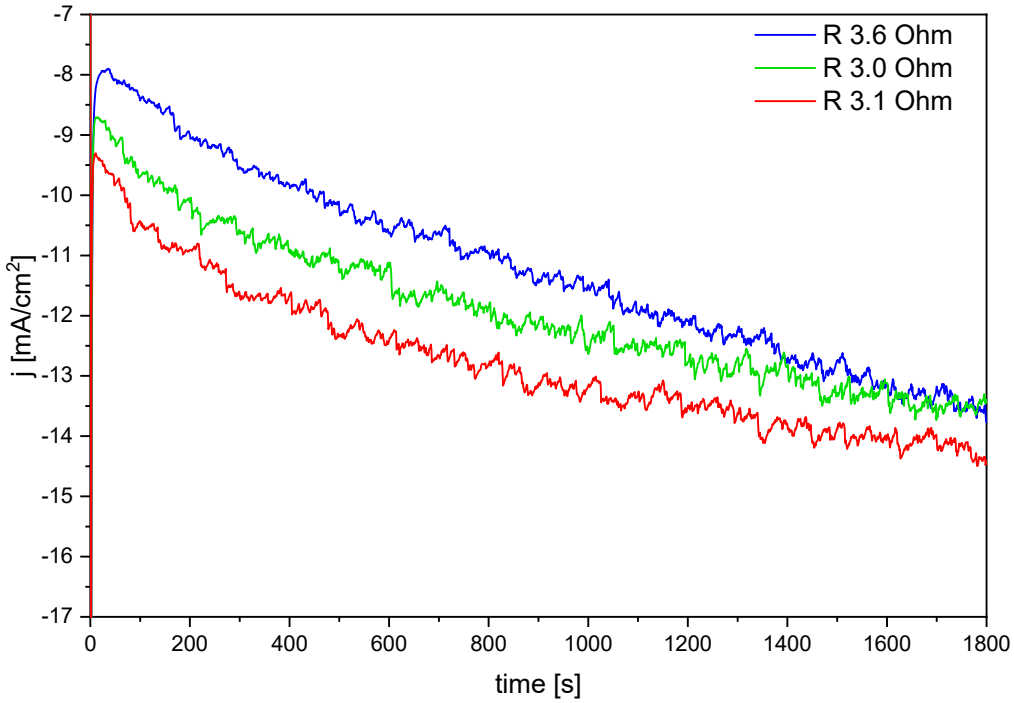

Figure 46: Three CA tests performed on the bare AC.

($CO_2 + H_2O + 2e^- \rightarrow CO + 2OH^-$). Further experiments, such as in situ pH measurements or rotating disk electrode studies, are recommended to verify this hypothesis and better understand the time-dependent increase in electrocatalytic activity.

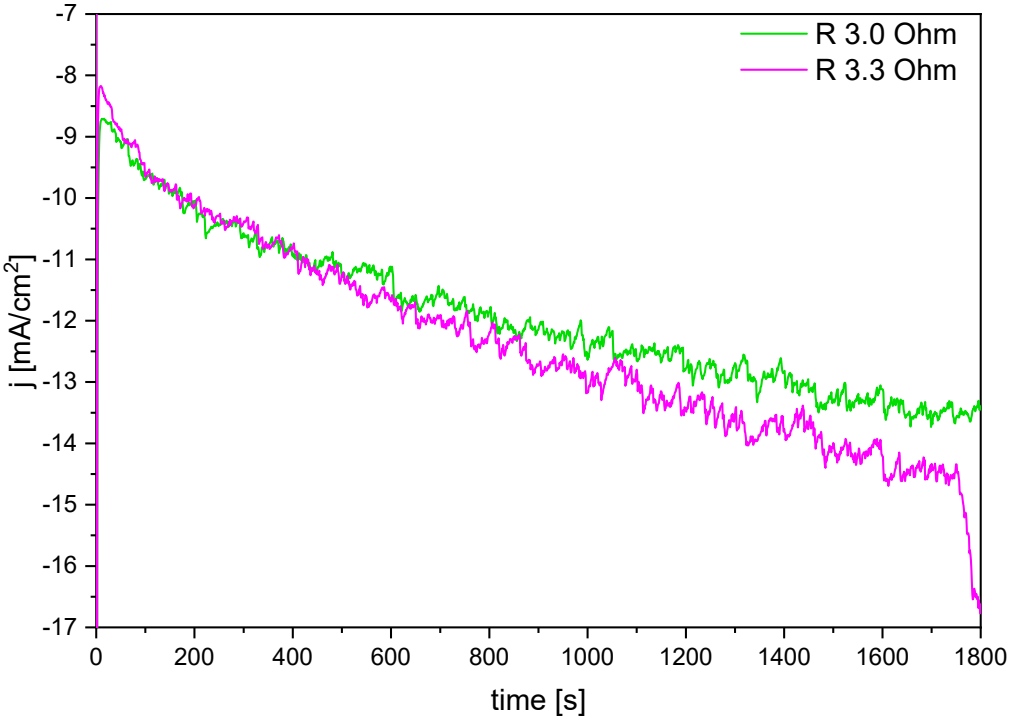

Figure 47: Two consecutive CA test on the same electrode, changing the electrolyte.

E Solubility test

The first solubility test of BiSub was conducted in ethanol at 96% and 99% purity, using the same concentration employed in the synthesis (0.0646 M). After stirring overnight (16 hours), the dispersions were left undisturbed for two days to allow complete sedimentation. Figure 48 shows the vials containing the settled dispersions.

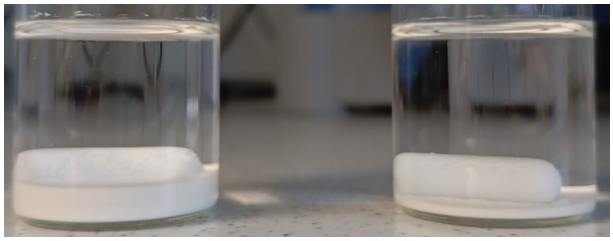

Figure 48: Settled dispersion of BiSub in 96% EtOH (left) and 99% EtOH (right) after two days.

A visibly smaller amount of BiSub settled in 99% EtOH compared to 96%, indicating better solubility. Consequently, all subsequent solubility tests were performed using 99% EtOH.

For the BiNPs@AC-SA material, salicylic acid was added incrementally to a dispersion of BiSub in 99% EtOH (0.0646 M) until reaching a final SA concentration of 1.8 M. Complete dissolution of BiSub was not achieved, but this SA concentration was used for the synthesis.

In the case of BiNPs@AC-AcOH materials, solubility tests were carried out in both pure acetic acid and a 1:1 (v/v) mixture of AcOH and EtOH. Interestingly, the mixed solvent, despite being less acidic, exhibited improved BiSub solubility compared to pure AcOH, as shown in Figure 49.

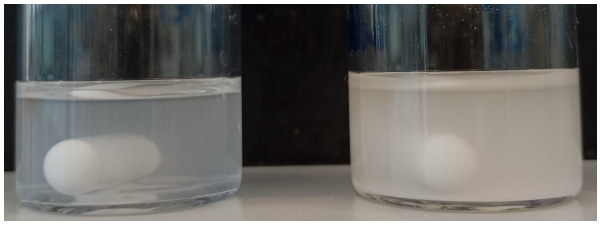

(a) Mixed dispersions in AcOH/EtOH (left) and pure AcOH (right).

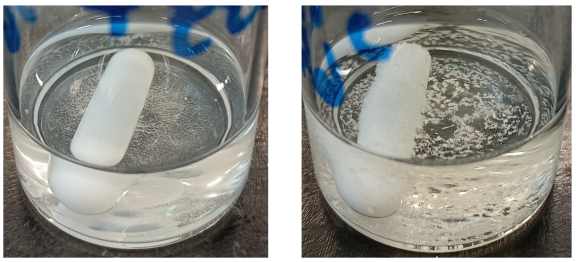

(b) Settled dispersions in AcOH/EtOH (left) and pure AcOH (right).

Figure 49: Dispersions of BiSub in a mixture AcOH/EtOH and pure AcOH: (a) immediately after mixing, (b) after sedimentation.

In the sample prepared with pure AcOH, needle-like crystals were observed after sedimentation (Figure 49b). These crystals are likely salicylic acid. This interpretation is supported by the fact that BiSub is soluble in acidic media due to protonation of salicylate anions ($HSal^-$), which leads to the release of Bi^{3+} cations into solution.[59] Furthermore, the solvent mixture, that is less acidic than pure AcOH, exhibits improved solubility, suggested by more transparent dispersion. This effect can be attributed to the lower solubility of salicylic acid in acetic acid compared to ethanol. At 25 °C, the mole fraction

solubility of SA is reported as 54.93E-03 in AcOH[84] and 0.143 in EtOH[60]. This substantial difference in solubility explains the increased turbidity observed in the pure AcOH dispersion, where SA tends to precipitate and form visible needle-like crystals.

F DTG curves

The DTG curves, of the TGA analysis perfomed in air, of all the materials are shown in this appendix.

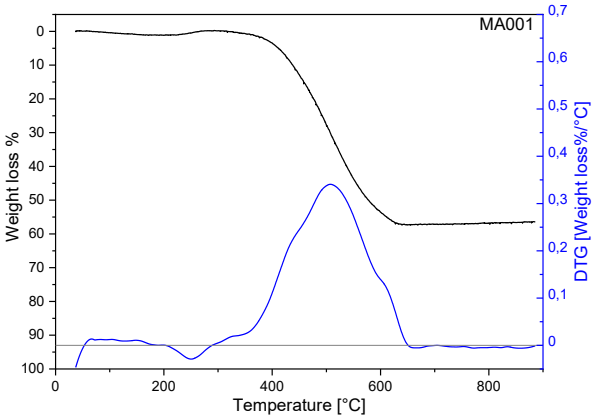

Figure 50: TGA and DTG curves of MA001.

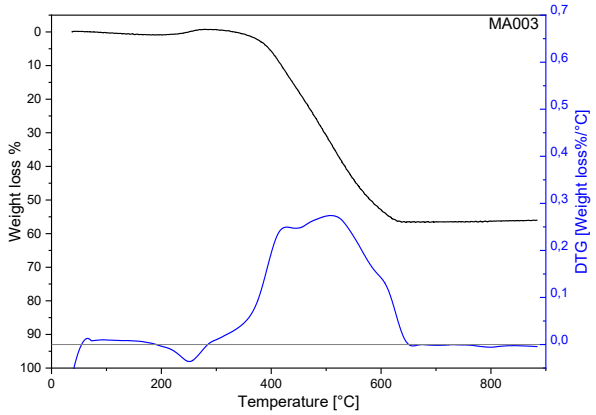

Figure 51: TGA and DTG curves of MA003.

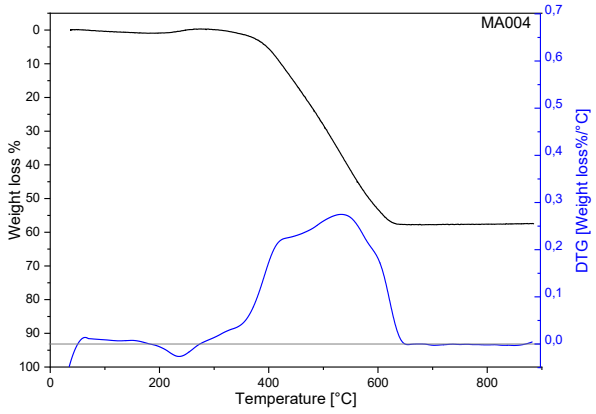

Figure 52: TGA and DTG curves of MA004.

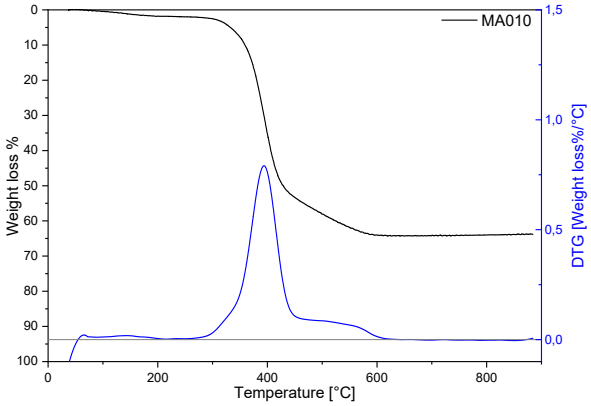

Figure 53: TGA and DTG curves of MA010.

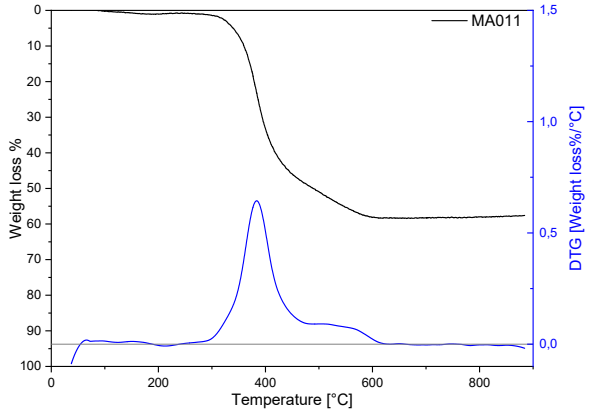

Figure 54: TGA and DTG curves of MA011.

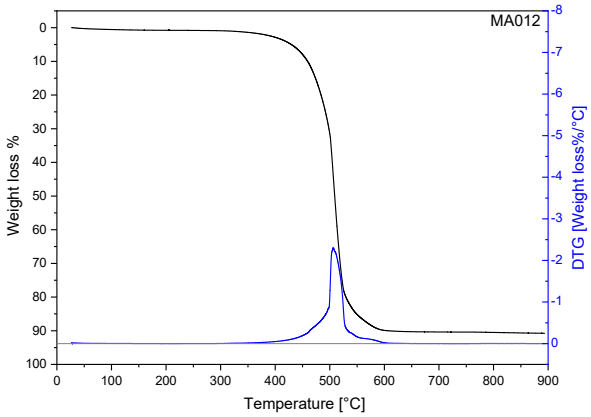

Figure 55: TGA and DTG curves of MA012.

G CA and HPLC results

For each material, the three CA curves and the HPLC analysis of the catholyte are shown in this appendix. In the HPLC graph, the curve of the second test (green) is shifted by +1500 nRIU on the vertical axis, and the third test curve (red) by +3000 nRIU to improve readability. All HPLC chromatograms exhibit similar profiles, showing two positive peaks at approximately 17 and 26 minutes of retention time, corresponding to formate and DMSO (used as the internal standard), respectively. Additionally, a negative peak appears around 21 minutes, attributed to the presence of bicarbonate ions (HCO_3^-) from the electrolyte ($NaHCO_3$). In some chromatograms, a slight horizontal shift of the peaks can be observed, which is likely due to minor variations in injection volume or flow rate during the analysis.
The anolyte was also analyzed; however, since no formate or other liquid product were detected, the corresponding graphs are not reported.

In Table 15 are shown the data used to graph the calibration curve used for the Faradaic efficiency calculation.

Table 15: Calculation for the calibration curve used to measure the Faradaic efficiency.

Total volume [L]	FA [M]	DMSO [M]	FA/DMSO [M/M]	$Area_{FA}/Area_{DMSO}$
1.60E-03	1.25E-03	9.38E-03	1.33E-01	2.78E-02
	2.50E-03		2.67E-01	4.86E-02
	3.75E-03		4.00E-01	7.72E-02
	5.00E-03		5.33E-01	1.05E-01
	6.25E-03		6.67E-01	1.36E-01

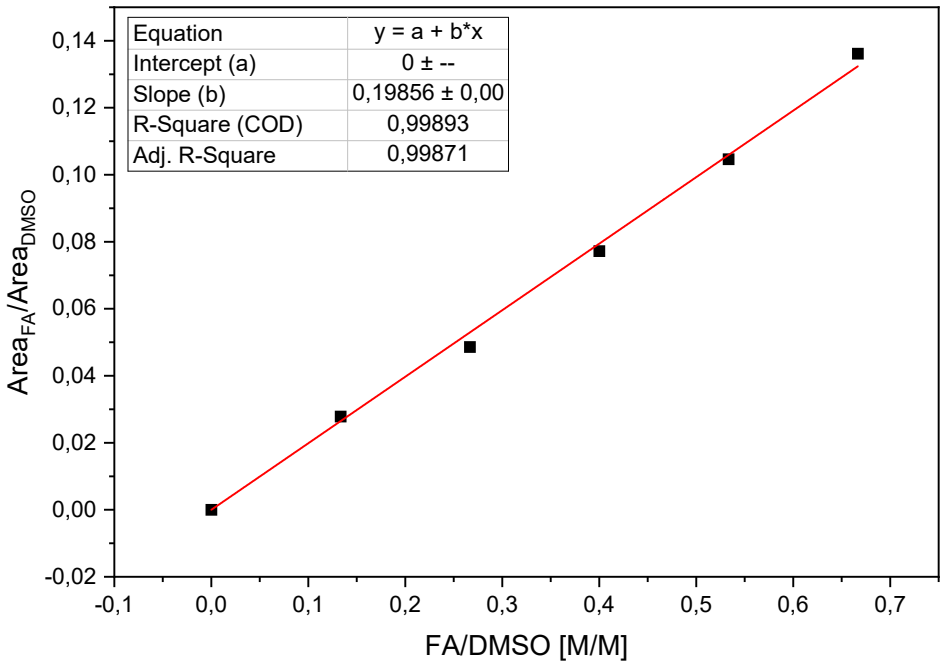

Figure 56: Calibration curve obtained with the data in Table 15.

In Table 16 are reported the calculation of the Faradaic efficiency.

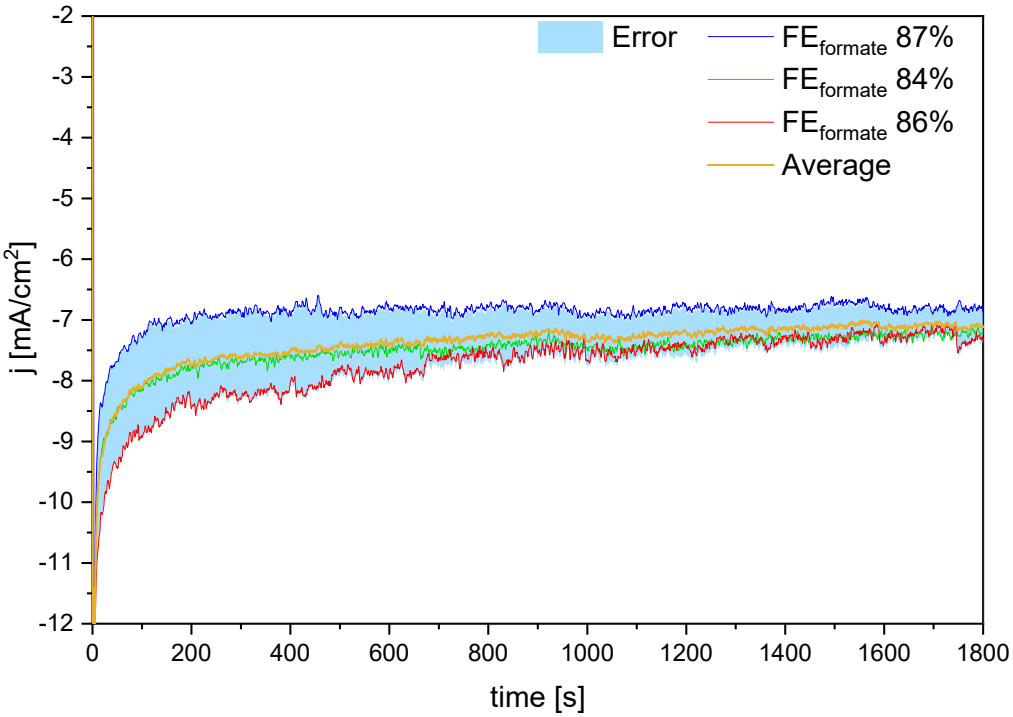

Figure 57: Chronoamperometry tests performed on MA001 at -1.07 V vs. RHE for 30 minutes. The R_u of blue, green and red line was 3.0, 3.5 and 3.4 respectively.

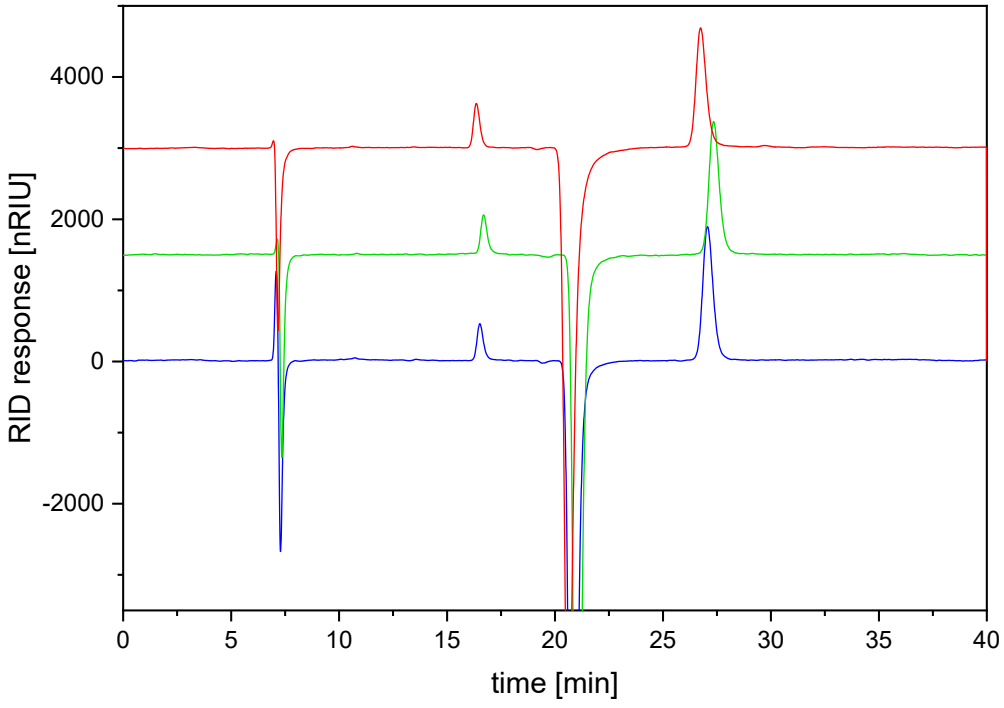

Figure 58: HPLC tests on the catholyte of the three CA test on MA001.

fill

This thesis project was carried out in collaboration with the University of Groningen. Thanks to the University of Groningen for the opportunity and for providing me with the necessary resources and support.

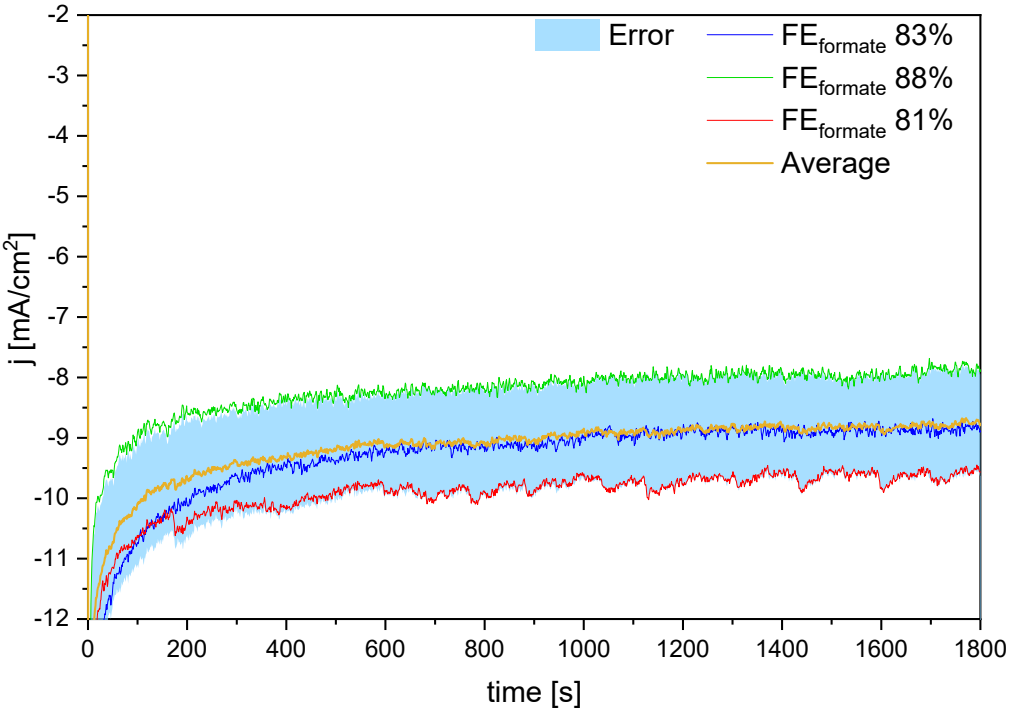

Figure 59: Chronoamperometry tests performed on MA003 at -1.07 V vs. RHE for 30 minutes. The R_u of blue, green and red line was 3.1, 3.0 and 3.1 respectively.

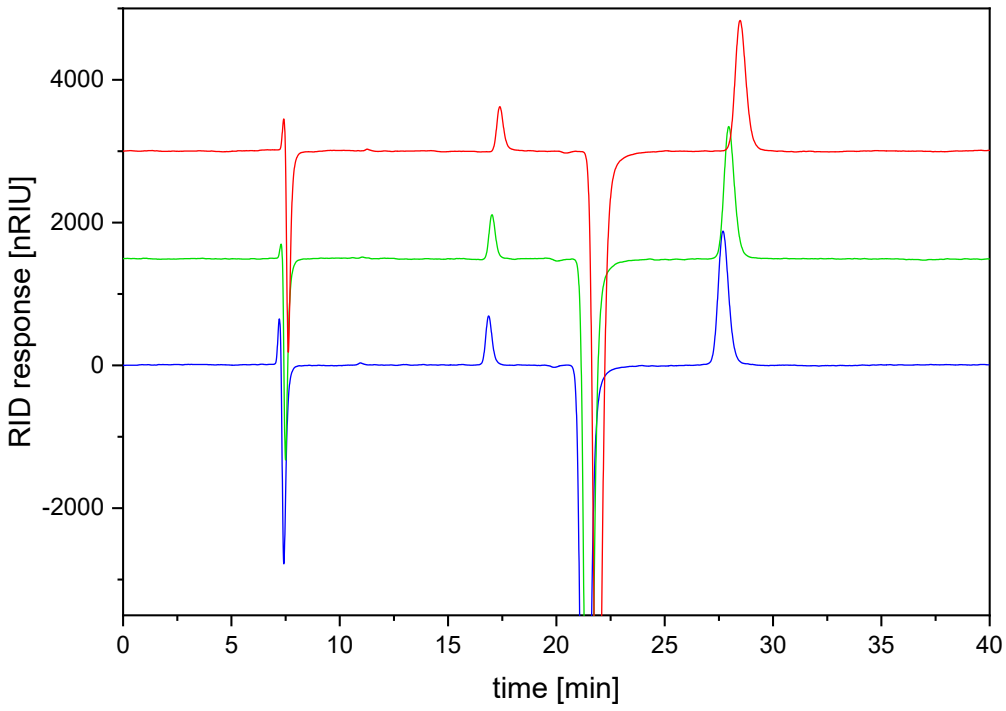

Figure 60: HPLC tests on the catholyte of the three CA test on MA003.

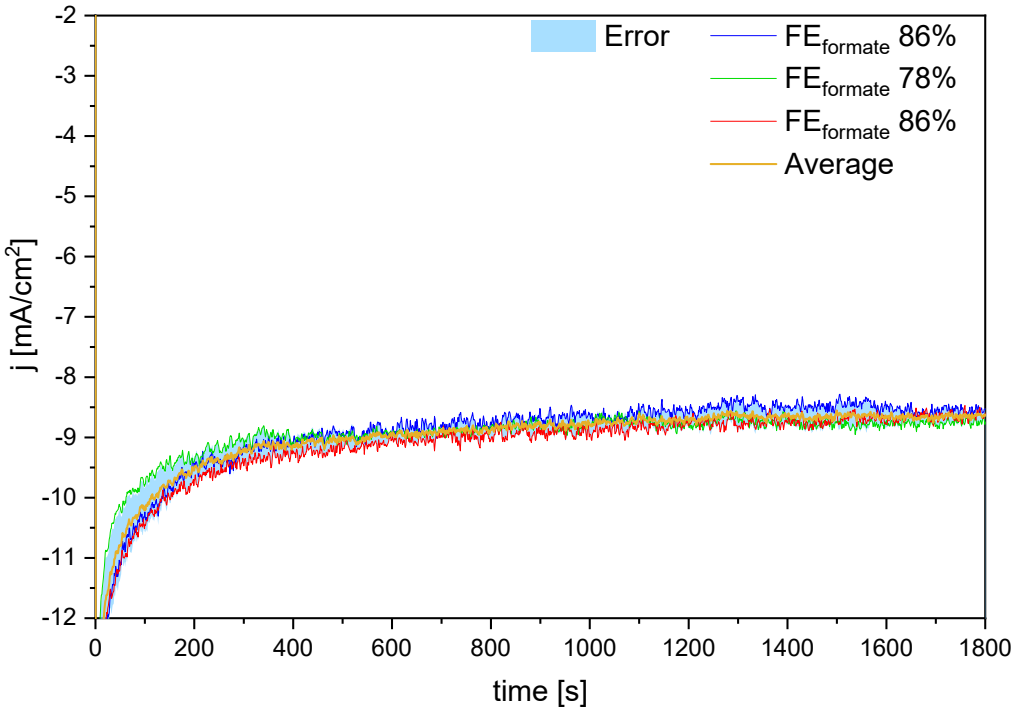

Figure 61: Chronoamperometry tests performed on MA004, with catalyst loading 0.296 mg cm^{-2}, at -1.07 V vs. RHE for 30 minutes. The R_u of blue, green and red line was 3.4, 3.3 and 3.0 respectively.

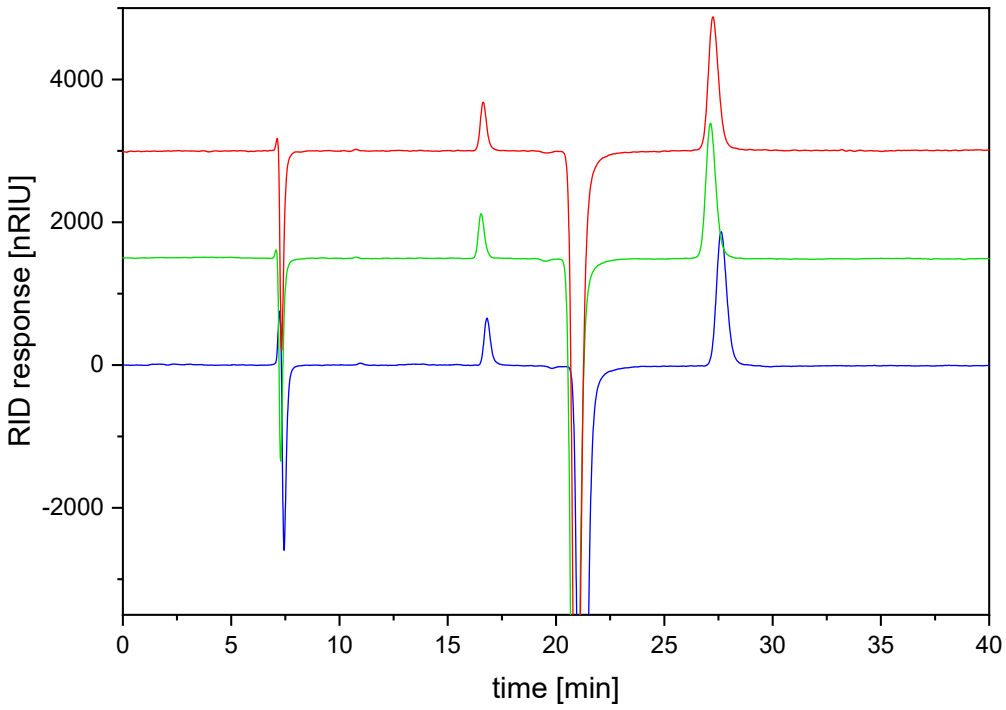

Figure 62: HPLC tests on the catholyte of the three CA test on MA004.

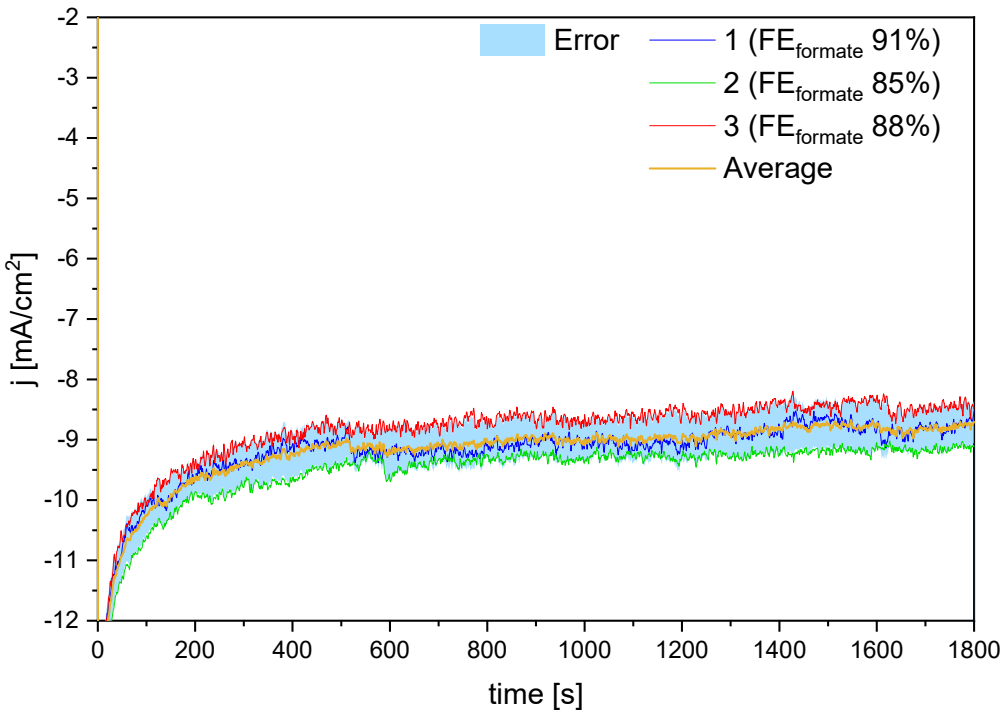

Figure 63: Chronoamperometry tests performed on MA004, with catalyst loading 0.385 mg cm^{-2}, at -1.07 V vs. RHE for 30 minutes. The R_u of blue, green and red line was 3.1, 3.0 and 3.1 respectively.

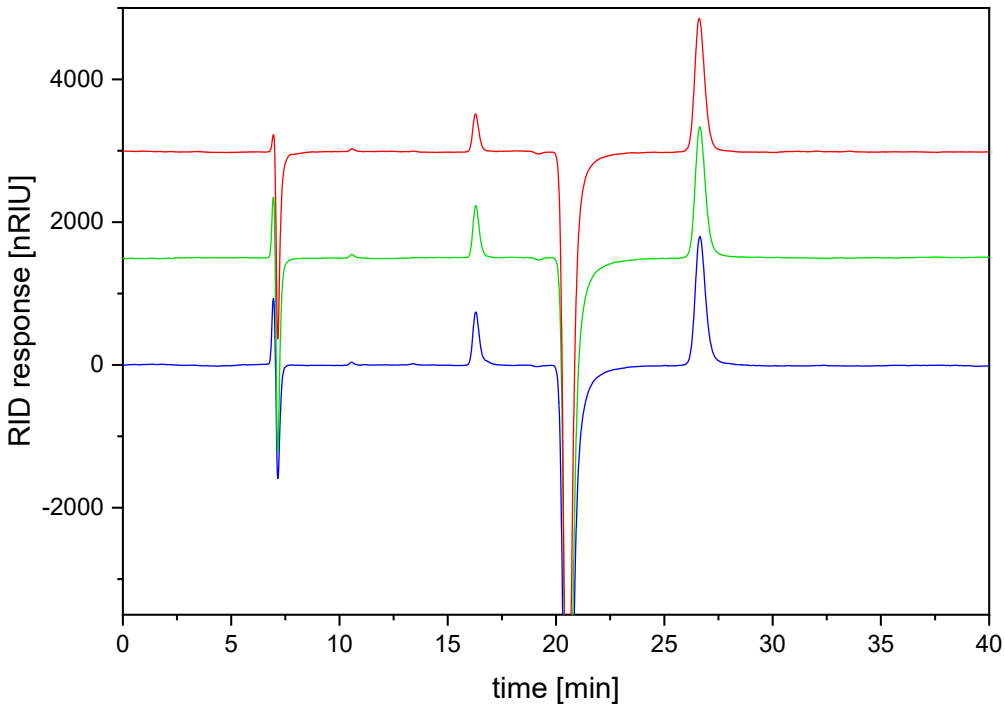

Figure 64: HPLC tests on the catholyte of the three CA test on MA004 with catalyst loading 0.385 mg cm^{-2}.

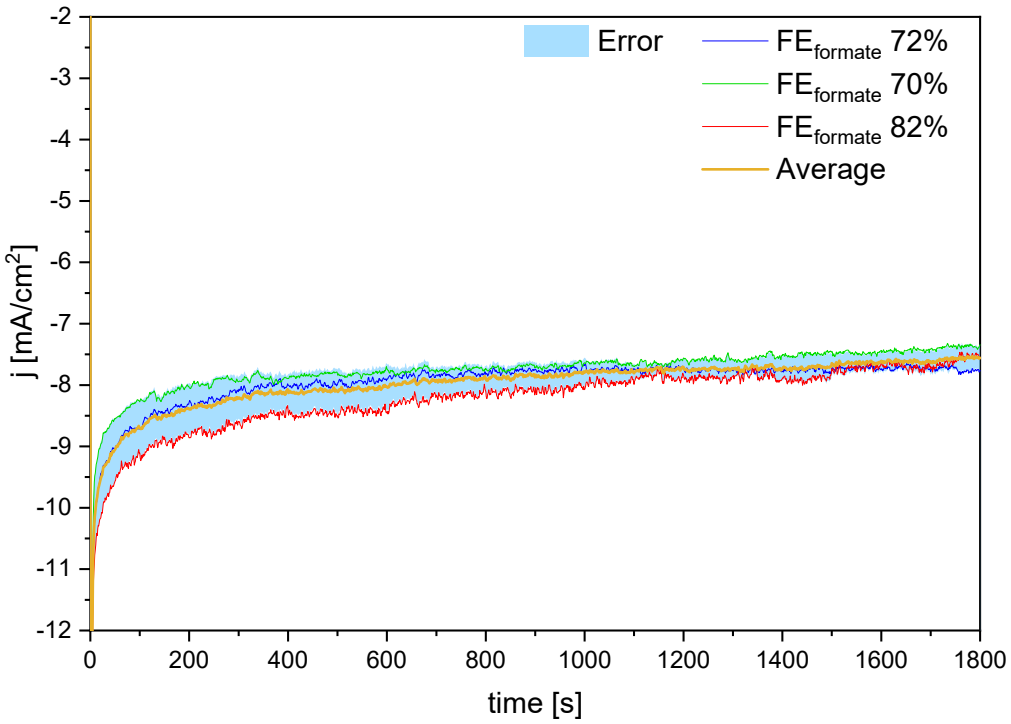

Figure 65: Chronoamperometry tests performed on MA010 at -1.07 V vs. RHE for 30 minutes. The R_u of blue, green and red line was 3.2, 3.3 and 3.0 respectively.

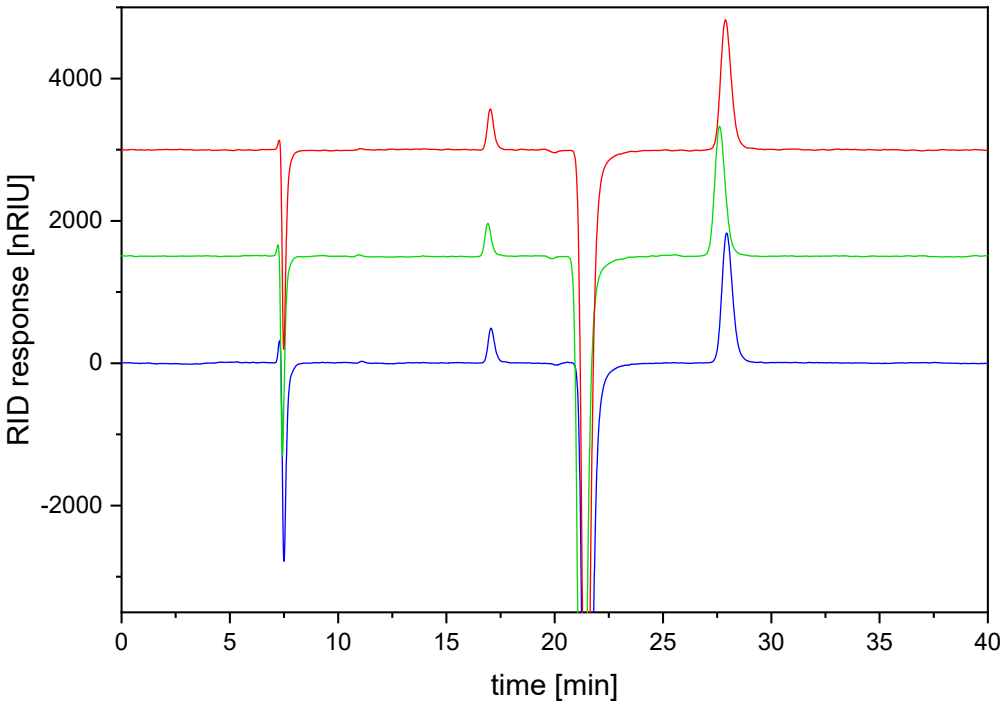

Figure 66: HPLC tests on the catholyte of the three CA test on MA010.

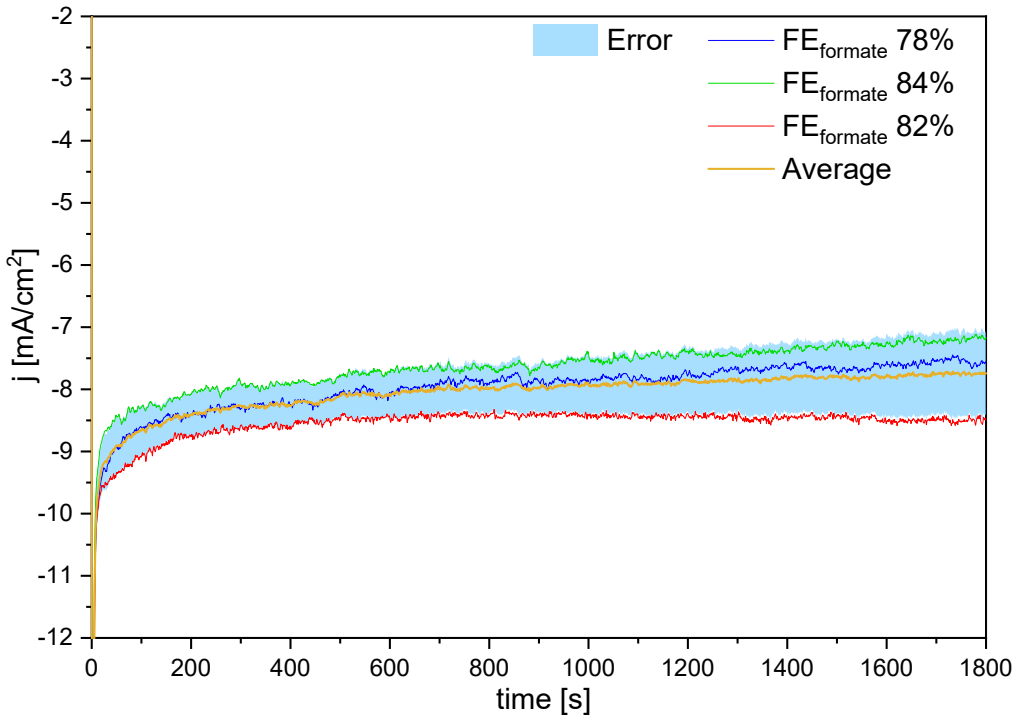

Figure 67: Chronoamperometry tests performed on MA011 at -1.07 V vs. RHE for 30 minutes. The R_u of blue, green and red line was 3.4, 3.1 and 3.8 respectively.

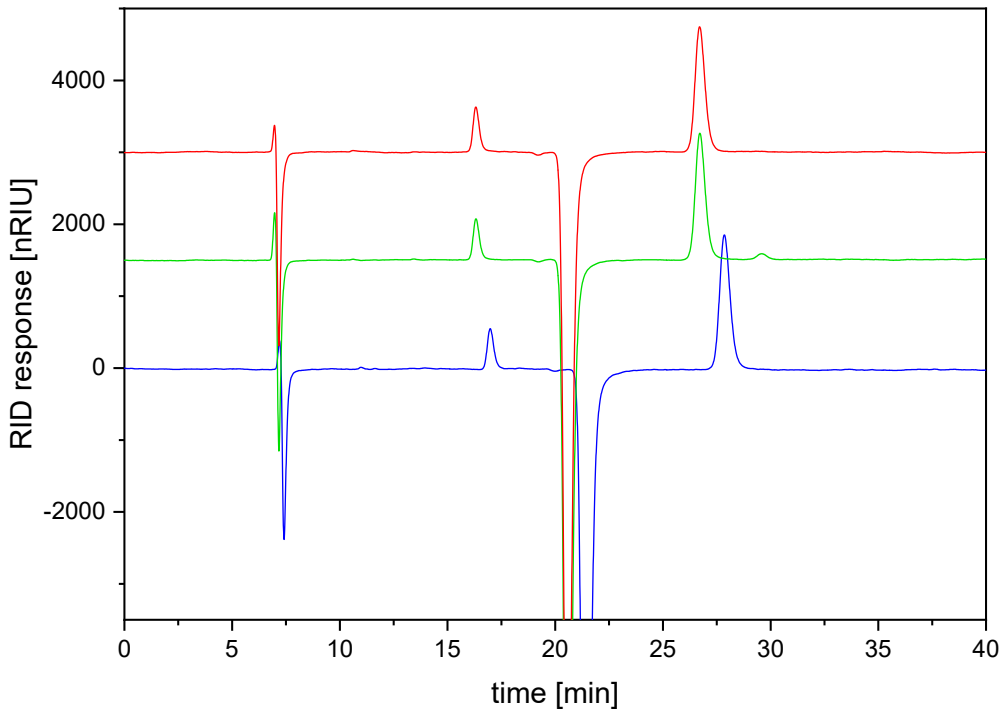

Figure 68: HPLC tests on the catholyte of the three CA test on MA011.

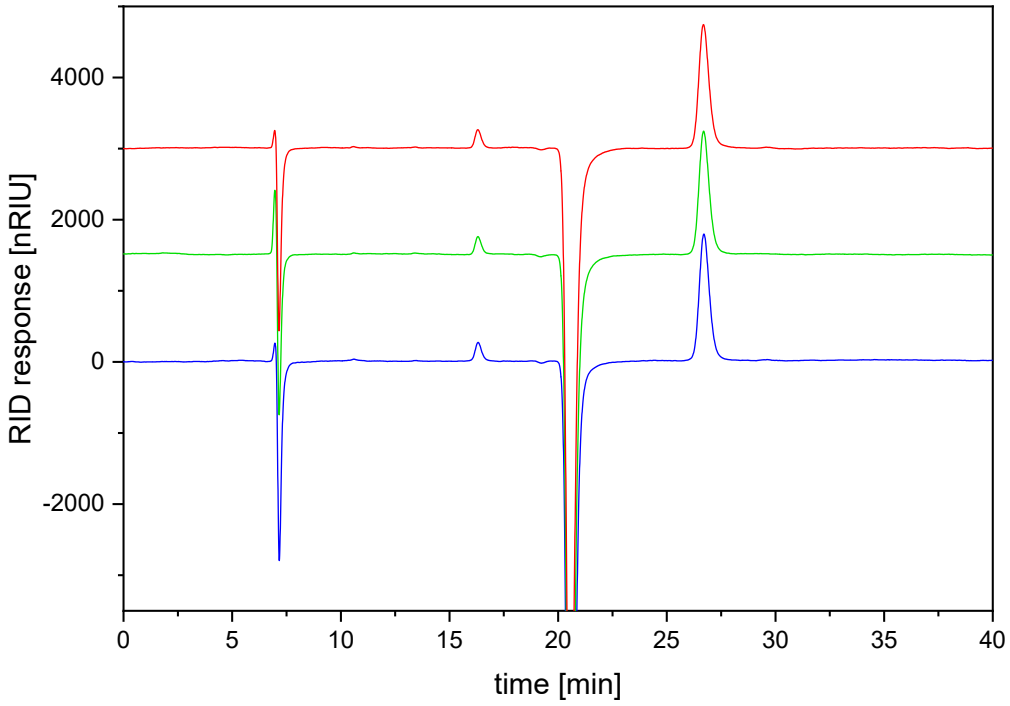

Figure 69: HPLC tests on the catholyte of the three CA test on MA012.

Table 16: Formate production and Faradaic efficiency results.

Material	$Area_{FA}/Area_{DMSO}$	$Total_{FA}$ [mol]	Total charge [C]	$FE_{formate}$ [%]
MA001	0.178	9.41E-05	2.08E+01	87.1
	0.188	9.96E-05	2.28E+01	84.2
	0.213	1.61E-05	2.53E+01	85.8
MA003	0.231	1.22E-04	2.83E+01	83.5
	0.216	1.14E-04	2.50E+01	88.3
	0.239	1.27E-04	3.01E+01	81.1
MA004 (0.296 mg cm^{-2})	0.228	1.20E-04	2.71E+01	85.7
	0.207	1.09E-04	2.72E+01	77.5
	0.234	1.24E-04	2.77E+01	86.1
MA004 (0.385 mg cm^{-2})	0.269	1.42E-04	3.03E+01	90.6
	0.260	1.37E-04	3.12E+01	85.0
	0.233	1.23E-04	2.72E+01	87.6
MA010	0.169	8.94E-05	2.41E+01	71.6
	0.162	8.58E-05	2.35E+01	70.5
	0.199	1.05E-04	2.49E+01	81.6
MA011	0.200	1.06E-04	2.60E+01	78.5
	0.195	1.03E-04	2.37E+01	84.2
	0.209	1.11E-04	2.59E+01	82.3
MA012	0.090	4.74E-05	1.25E+01	73.0
	0.089	4.69E-05	1.30E+01	69.8
	0.088	4.67E-05	1.36E+01	66.5

Acknowledgement

I would like to express my sincere gratitude to the univestity of Groningen and the ENTEG (Engineering and Technology institute Groningen) for providing me the opportunity to conduct research at their facilities. I am particularly grateful to technician for their support throughout my stay, and to Prof. Paolo P. Pescarmona and Dr Jiahui Zhu and Jennifer Hong for their supervision.